Corso di Laurea Magistrale
in Chimica e Tecnologie Sostenibili

Tesi di Laurea

Small-Angle Neutron Scattering: a Study of the Porosity of Historical Ceramic Materials.

Relatore
Ch. Prof. Elti Cattaruzza

Correlatrice
Dr.ssa Claudia Mondelli

Laureando
Sandro Zorzi
Matricola: 849103

Anno Accademico
2019/2020

Dipartimento di Scienze Molecolari e Nanosistemi
Università Ca' Foscari Venezia

Contents

Abstract

Ceramics are complex objects and a rich source of information: they constitute a large part of the staple memory of past and present human activities. A deep understanding of traditional ceramics is an essential key to designing new ceramic materials. The demanding synthesis of ceramics with fine-tuned properties, such as enhanced mechanical, electrical, optical or magnetic characteristics, must be associated with cutting-edge analysis procedures in order to improve the engineering process. The neutron-based non-destructive approach reported in this thesis has proved to be an effective investigation technique for exploring both traditional and advanced ceramic materials. The historical ceramics samples analysed in this thesis are divided in two groups distinguished for the excavation sites and the manufacturing period. The Mediterranean group is constituted of samples from excavation sites in Torcello (Venice), originating from the Mediterranean basin and dated from the 5^{th} to the 12^{th} centuries. These samples belong to shreds of globular amphorae mainly involved in the trade of goods. They are made by terracotta, which is the simplest and coarsest type of pottery. The German group is constituted of ceramic shreds dated from 13^{th} to 19^{th} centuries, from several excavation sites located in Central and Eastern Germany. This group includes different type of ceramic, made from a more carefully selected and finer raw materials and a higher technology than the Mediterranean ones. The German ceramics shreds are: stoneware, near-stoneware, unglazed earthenware and glazed earthenware. The Mediterranean samples are defined as late antique amphorae The samples were previously been analysed with other techniques during the PhD work of Dr. Giulia Ricci, in order to well understand their chemical and mineralogical structure which is connected to their firing temperature [1]. This characterisation was achieved using several techniques, such as Fourier-Transform Infrared Spectroscopy (FT-IR), Micro-Raman Spectroscopy (μ-Raman), X-ray Diffraction (XRD), and Scanning Electron Microscope coupled with Energy Dispersive X-ray Probe (SEM-EDX). The present work of thesis is focussed on the study of the nanoporosity of a large number of the samples belonging to these two historical groups by means of Small Angle Neutron Scattering (SANS) technique, in order to obtain a deep knowledge of their morphology analysing the

open and closed nanopores ratio, their shape and tortuosity. Neutron scattering is a continuous evolving technique, which has a relevant importance for different field of research as physics, material science, chemistry, biology, etc.. It is a powerful method for the detailed investigation of condensed matter. Neutrons have wavelengths of the order of atomic dimension, they present a magnetic moment and energies allowing the investigation of the space-time behaviour of condensed matter on a microscopic scale over many decades and dynamic from neV to eV [2]. In particular SANS technique allows the investigation of the structure, i.e. shape and size of microscopic objects, from some Ångström (Å) to some thousand of Å. The small-angle term means that information regarding the structure of probed objects are contained in the intensity of elastically scattered neutrons typically at 2ϑ less than 2° [3]. Neutrons are product by uranium fission or by spallation process, both require a high technological and expensive infrastructures. This is why around the world there are "only" almost 22 neutron sources available for scientific purpose. The most intense neutron facility is the Institut Laue – Langevin (ILL) located in Grenoble, France. This international research centre provides a very high flux of neutrons feeding 40 state-of-the-art instruments [4]. For this work of thesis SANS measurements of historical ceramic samples were obtained by means of the D11 instrument at ILL. The beam time was obtained passing through a submission of a scientific proposal and a high competitive selection process by a panel of international experts. The experimental set up has been arranged to cover the widest Q range available on D11 in order to cover spatial dimensions from few Å to almost 600 nm.

The global analysis of the data using the Porod's Invariant technique allows to obtain the total volume of the pores inside the clay matrix. The same analysis has been used on data obtained enhancing experimentally the signal from the closed pores in order to obtain the ratio closed/open pores. The main result was that the nanoporosity in samples from the same historical group (even if they have different origin) is closed to the same value and it is clearly different for the two groups: the Mediterranean samples exhibit higher porosity than the German ones. This result can be explained with the differences in the granularity of the starting raw materials coming from the different technology in the two historical periods of the ensemble of the studied samples. Furthermore, a detailed analysis of the shape of the SANS curves allow the determination of the form factor of the pores. Using Small Angle Scattering Analysis Software package (named SasView) we find that the pores can be described as flexible cylinders with elliptical cross section for both groups, but ones again the results are distributed in two well distinguished families for the two groups: the pores of Mediterranean samples are more extended toward into the matrix exhibiting a high tortuosity and a

more flattened elliptical cross section than German ones. The ensemble of this results represent a new and original work on the nanopores in ceramics and it is the object of a publication in an international journal [5].

Chapter 1

Introduction

What are neutrons ?
The neutron was discovered in 1932 by James Chadwick by means of the collision between alpha particle and the nuclei of beryllium [4]. It is a particle with no charge and whit a mass very close to that of proton, which constitute with the latter the nuclei of atoms. Due to its neutrality it can penetrate deeply into the matter. Its prominent properties that are wavelengths of the order of atomic dimension and, at the same time, frequencies of the order of characteristic vibrational frequency allow the investigation of the space-time behaviour of condensed matter on a microscopic scale over many decades [2]. It is a powerful method for the detailed investigation of condensed matter.Neutron scattering is a relevant techniques for different field of research as physics, material science, chemistry, biology, etc..

What are historical ceramics ?
Ceramics are complex non-metallic inorganic solids. This term refers to an object made by firing clay material extracted from the earth, that are mainly composed of alluminosilicates. In the context of this thesis ceramics are referred to artifacs coming from two different excavation sites. One part of fragments have been recovered from excavation sites in Torcello (Venice, Italy), originating from the Mediterranean basin and attributed to three main epoch: Late Antiquity (5^{th}-7^{th} centuries), Early Middle Ages (8^{th}-10^{th} centuries) and Middle Age (10^{th}-12^{th} centuries). The other part of the ceramic shreds, dating from the late 13^{th} to 19^{th} centuries, have been recovered from several sites located in Central and Eastern Germany, provided by the Landesamt für Archäologie Sachsen in Dresden (Germany).

What could be result if these two objects are "combined"?
This last question represent in a romantic way what in this work has been done. Neu-

trons have been employed as a probe which pass through the body of the historical samples and comes out with a lot of information, regarding in this case, the morphology of the ancient pottery.
In this thesis, historical ceramic samples previously characterised in the PhD work of Dr. Giulia Ricci have been studied by means of Small Angle Neutron Scattering (SANS) technique.

The aim of this thesis is to report a neutron-based, non-destructive approach for the study of porosity of a pottery matrix. Ceramic is one of the most ancient industries widespread over the word. For this reason potteries are a rich source of information: they constitute a large part of staple memory of past and present human activities. In archaeological site, the ceramic findings are considered as the most important set of data due to their large distribution [6]. The continuous manufacturing process, for example the recycling of vessels and waste pieces found at archaeological excavation sites, has made it possible to create an archive of testimonies. A deep understanding of traditional ceramics is even an essential key to designing new ceramic materials.
The data collection and the first data reduction and treatment have been carried out during a 5 month stage that I have attended at the Institut Laue – Langevin.
The SANS data were obtained through the use of the instrument D11 at ILL during official experiments on historical ceramic samples, using the beam-time assigned through a high competitive selection by means of research proposals submitted to an international scientific committee which has to judge and eventually assign the beam-time to the winning projects. In these SANS experiments, samples were analysed with the instrumental configurations reported in section 5.1.
This work is the result of the collaboration between the University Ca'Foscari of Venice and the Institut Max von Laue - Paul Langevin (ILL) sited in Grenoble (France). ILL is an international research centre at the leading edge of neutron science and technology. It provides scientists with a very high flux of neutrons feeding 40 state-of-the-art instruments [7].

Bibliography

[1] Giulia Ricci, PhD thesis, Ca'Foscari Venezia, **2016**, 203 pp.

[2] *Studying Kinetics with Neutrons: Prospects for Time-Resolved Neutron Scattering*, *Vol. 161*, (Eds.: G. Eckold, H. Schober, S. E. Nagler), Springer Berlin Heidelberg, Berlin, Heidelberg, **2010**.

[3] R. Roe, *Methods of X-ray and Neutron Scattering in Polymer Science*, Oxford University Press, **2000**.

[4] Bernard Jacort, *Neutron for Science*, **2006**.

[5] C. Mondelli, S. Zorzi, G. Ricci, V. Galvan, E. Balliana, R. Schweins, E. Cattaruzza, *ChemPhysChem* **2020**, *21*, 966–970.

[6] M. Vidale, *Ceramica e archeologia*, (Ed.: Carocci), **2007**.

[7] ILL web site, Library Catalog: www.ill.eu, `https://www.ill.eu/`.

Chapter 2

Neutron Scattering

Neutron scattering is one of the most powerful methods for the detailed investigation of condensed matter. A plethora of different techniques have been developed using the neutron as a probe that interacting with nuclei can "tell what it has seen" in its travel inside the matters. The neutron is a particle with no charge and whit a mass very close to that of proton, which constitute with the latter the nuclei of atoms. Due to its neutrality it can penetrate deeply into the matter. Its prominent properties that are wavelengths of the order of atomic dimension and frequencies of the order of characteristic vibrational frequency allowing the investigation of the space-time behaviour of condensed matter on a microscopic scale over many decades.
Neutron was discovered in 1932 by James Chadwick by means of a nuclear reaction in which an alpha particle collided with the nuclei of beryllium. In the 1939 Hahn and Strassman discover that the nucleus of uranium (^{235}U) would undergo fission induced by capturing a neutron, producing energy and the emission of other neutrons. The first practical application of this type of reactivity of the Uranium was done in 1942 by Enrico Fermi in the "Manhattan Project" for the development of the atomic bomb. In 1943 was built the first experimental reactor at Oak Ridge in Tennessee, USA, producing a 3.5 MW of heat and a flux of neutrons of about 10^{12}, involved in the production of plutonium required to build atomic weapons. After the end of the second world war even in Europe the experimental neutron reactors have started to appear, and one of the most important is nowadays the Institut Max Von Laue - Paul Langevin (ILL) [1].

2.1 Neutron source

The production of neutrons which are suitable for the purpose of investigating condensed matter on the nanometric length scale requires a two-stage process. Firstly

neutrons have to be liberated via nuclear excitation and subsequent nuclear decay process, producing high-energy neutrons of several MeV (with a very short wavelength). In the second stage they have to be slowed down until few meV to be used as an efficient and adequate probe.
Nowadays neutrons are produced by two different methods:

1. fission;

2. spallation.

In the first case a continuous flux of neutrons is produced while the second source produces a pulsed flux.
Based on their energy, neutrons can be distinguished in: thermal with E≈0.25 eV, epithermal with energies form 1 eV to 100 keV and the fast (or even called "hot") with E>100 keV.

2.1.1 Fission Source

In the case of **fission**, slow neutrons are absorbed by metastable ^{235}U (which exist as 0.7% of natural occurring uranium), producing averagely 2.5 neutrons for each nucleus and a cascade of fission products, as showed in figure 2.1. The resulting fast neutrons with an energy of about 1 MeV are slowed down to meV energies by means of a moderator. The moderator is build up of light atoms such as for example H_2O

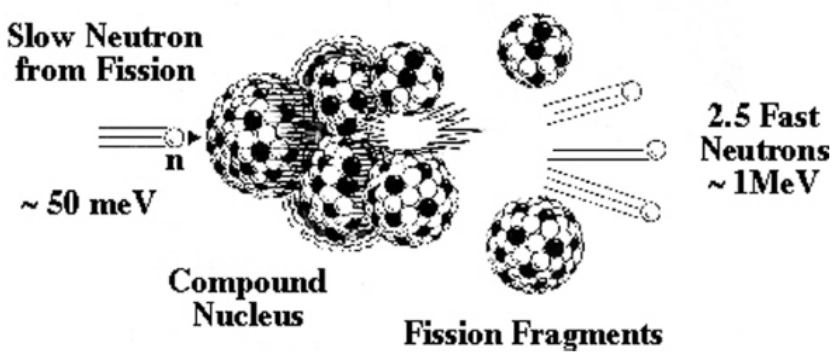

Figure 2.1: Schematic representation of a generic fission reaction [2]

or D_2O, which take up an appreciable amount of the neutron energy from collisions. The best choice to have a high neutron flux is to employ D_2O instead of H_2O for the moderator, since the latter has a higher absorption cross section. In fact H_2O requires 18 collision to thermalise neutrons while for D_2O this number grows up to 25. After these average number of collisions, neutrons have energies comparable to that of

the atoms of the moderator. The Maxwellian distribution of the energy spectrum of neutrons can be shifted by changing the temperature of the moderator [3]. In fact employing heavy-water at averagely 293 K, the distribution of neutron energy is centred at 25 meV which correspond to a wavelength of $\lambda = 1.8$ Å. Some useful relations due to the Maxwell-Boltzmann distribution of the energy are:

$$\lambda_{max} = \frac{h}{(5mk_BT)^{1/2}} \tag{2.1}$$

$$E = \frac{h^2}{2m\lambda^2} = \frac{81,799}{\lambda^2} \qquad with \quad \lambda(\text{Å}) \quad and \quad E(meV) \tag{2.2}$$

At the Institut Laue - Langevin in the case of SANS instruments, "cold neutrons" with longer wavelength than 1.8 Å, with an energy distributions centred at 5.5 Å, are usually employed. These slow neutrons are obtained by means of a liquid hydrogen (D_2) moderator (T=20 K). "Hot neutrons" are instead obtained from a heated graphite moderator (T=2000 K) with a maximum at 0.6Å.

2.1.2 Spallation Source

In this case, the nuclear reactions occur by means of high-energy protons produced by an accelerator that hit a metallic target like uranium, tungsten, lead or mercury [4]. The reaction occurs above certain energy threshold for the incident particle, typically from 5 to 15 MeV. In the reaction (see figure 2.2), excited nuclei "boil off" particles like high-energy neutrons, various nucleons, photons and neutrinos. By spallation reaction 20 to

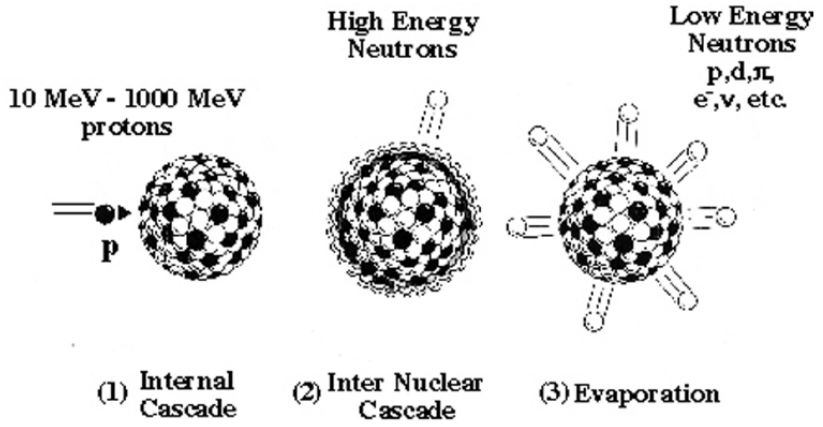

Figure 2.2: Representation of the spallation nuclear reaction [2]

30 neutrons per incident proton are typically generated. For the experimental use, the

produced neutrons have to be moderated for scattering applications. The spallation process is more efficient for neutron production than the fission one, in fact a 5 MW spallation source can product the same number of neutrons as a fission reactor of 50 MW but its overall energy balance is at least an order of magnitude higher than the fission ones in term of electrical power needed. Neutron flux produced from this kind of sources is not continuous. One example of a spallation source research centre is the ISIS Neutron and Muon source, based at the STFC Rutherford Appleton Laboratory in Oxfordshire (UK), which is characterised by: 800 MeV protons, U target, 200 A (50 Hz), pulse width= 0:27 μs, flux = 4 x 10^{16} n/s.

2.2 The Institut Laue - Langevin

The ILL is an example of fully successful scientific collaboration between European countries. It was born after the second world war from a reconciliation between the French and the German countries. Years later Great Britain joined the initiative. Nowadays this collaboration has become European-wide including 10 other European countries in the partnership, which are showed in the figure 2.3.

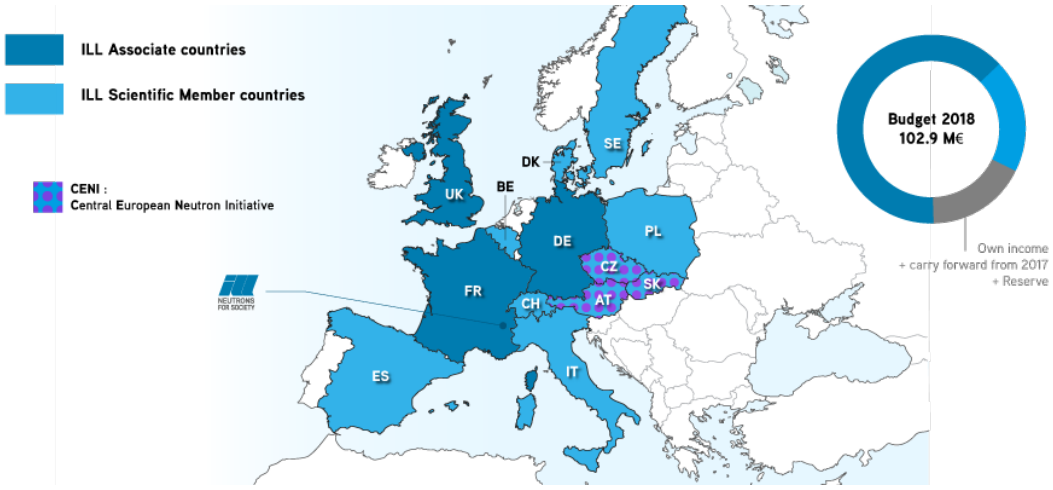

Figure 2.3: European partners and members of the ILL.[5]

This extended collaboration allowed Europe to surpass the USA in this field of research thanks to this extraordinary facility. ILL has a nuclear reactor with a uniquely high continuous neutron flux, which is unequalled nowadays in the world. The ILL facility is located in the city of Grenoble (France), surrounded by the French alps. It provides a very high flux of neutrons feeding 40 state-of-the-art instruments. The ILL reactor produce the highest world-wide flux of neutrons of 1.5 x 10^{15} neutrons per second per cm^2, with a thermal energy of 58.4 MW. The fuel element highly enriched in

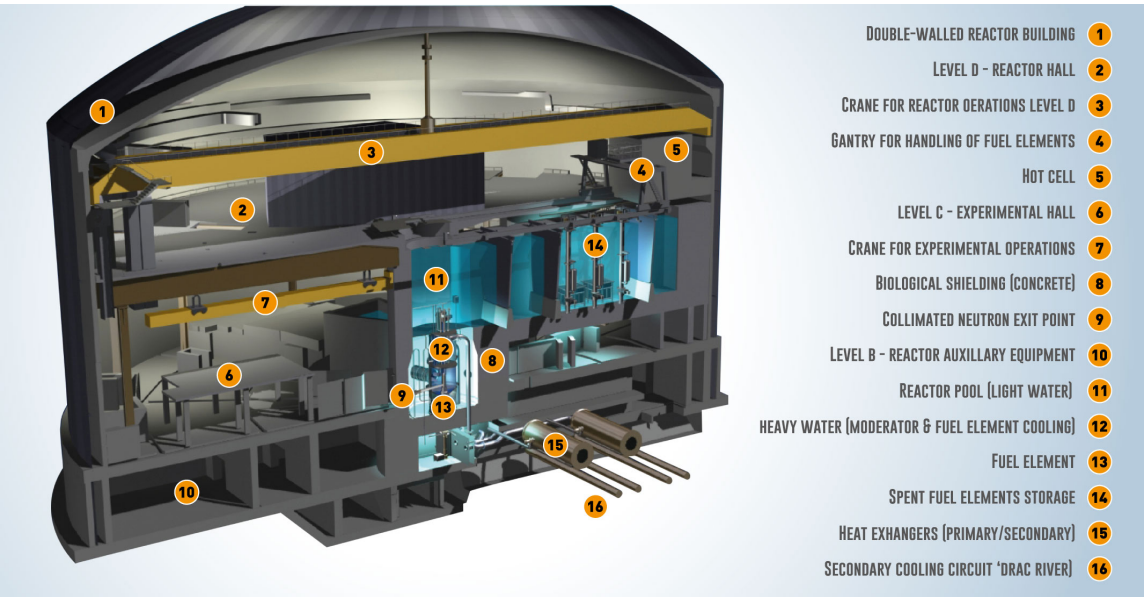

Figure 2.4: Graphical representation of the reactor building, the ILL 5 [5]

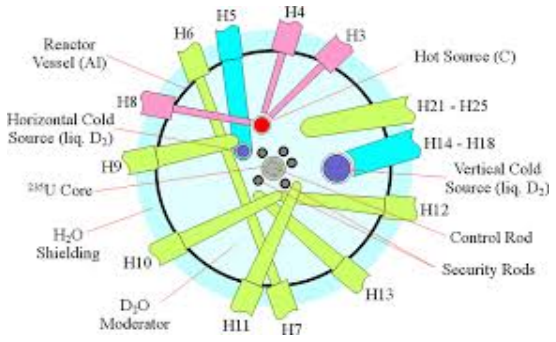

Figure 2.5: Disposition of the guides inside the reactor which collect neutrons at different speed. In red the hot line, in green the cold line and in blue the ultra cold line [6]

^{235}U, together with the control rod is arranged in the hole of a cylindrical holder which allows the circulation of the heavy-water. This cylinder is positioned in the centre of the moderator pool of 2.5 m of diameters filled with D_2O. This is surrounded by another pool of H_2O which shield the radiations. In figure 2.4 is shown an image of the reactor building (the ILL 5). Each reactor cycle is 50 day long and every year there are averagely 4.5 cycles providing for 225 days available for the research. The neutron guides which collect and transmit the neutron from the moderator to the instruments are shown in figure 2.5. The map of the ILL laboratories (ILL5, ILL7 and ILL 22) and the 40 instruments are shown in figure 2.6.

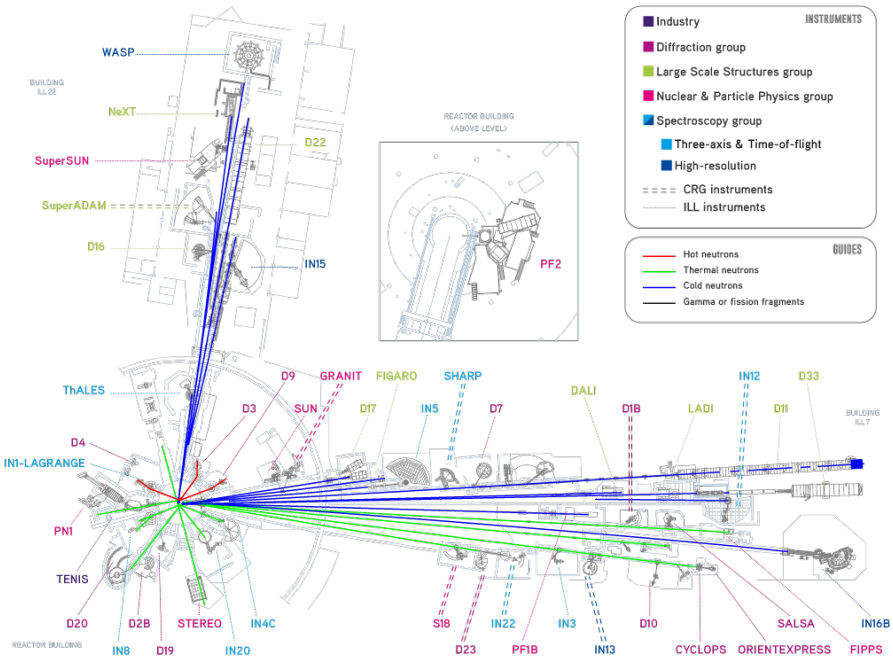

Figure 2.6: The map of the laboratory with the guideline and the instruments provided by the ILL [5]

2.3 Neutron Scattering

In a neutron scattering experiment, a collimated beam of neutrons of well-defined wavelength and energy interact with a sample. In a neutron scattering experiment, when the beam hit the samples, neutrons can be transmitted, absorbed or scattered in different directions. The probabilities that these events occur are defined by the cross section σ that have the dimension of [area]. The cross sections are the quantities actually measured in a scattering experiment. The geometry of the experiment can be represented as in figure 2.7 (a). We assume that the wave functions of the incident beam can be represented by a simple plane wave:

$$\psi_{inc} = \psi_{inc} exp(i(\boldsymbol{k_0 r} - \omega_0 t)) = \psi_0 exp(i\boldsymbol{k_0 r}) \tag{2.3}$$

where ψ_{inc} is the amplitude, $\boldsymbol{k_0}$ is the incident wave vector of magnitude $k_0 = 2\pi/\lambda_0$ and $\boldsymbol{r}$ is the position of the incident neutron. For simplicity during the scattering event, the energy loss is assumed to be negligible because the energy of the incident neutron is much larger than any energy exchange, i.e. the so-called **static approximation** [7]. Due to the fact that nuclear forces causing the scattering have a range of about 10^{-14} to 10^{-15} m, and the wavelength of a thermal neutron is of order of 10^{-10} m, it results much larger than the range of the forces and then the scattering will be isotropic. Then the

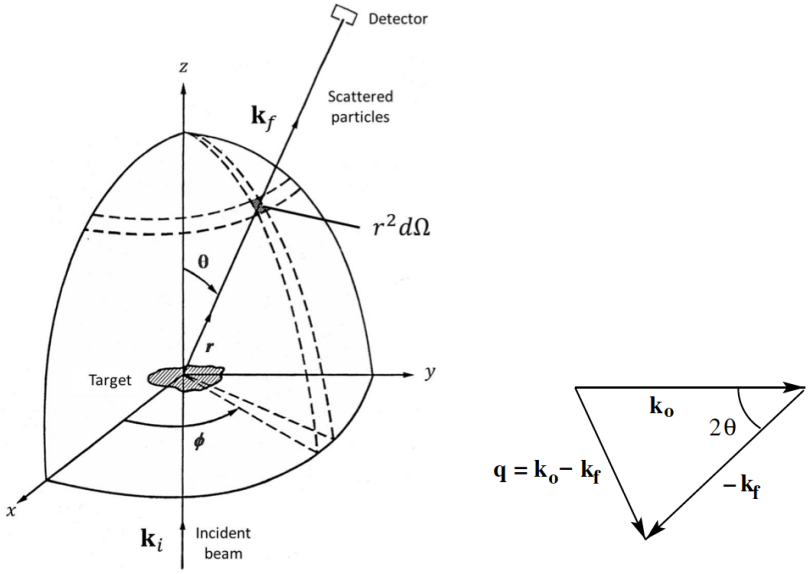

(a) Scheme of a typical scattering experiment

(b) Scattering triangle of wave vectors

Figure 2.7: Geometries of a typical scattering experiment.

wave function of a single neutron, which is scattered by a single scattering centre i at the origin of the coordinates is represented by a spherical wave

$$\psi_{scatt,i} = \frac{-\psi_0 b_i}{\boldsymbol{R}} exp(ik_f R) \tag{2.4}$$

where $\boldsymbol{R}$ is its the distance from the scattering centre and k_f is the magnitude of the final wave vector $\boldsymbol{k_f}$ [8]. Due to the static approximation, $k_f \approx k_0$. The constant b_i is the scattering length for the scattering centre i, which is a function of its interaction with the neutron and it has a dimension of length. This value depends randomly upon the atomic number of the scattering nucleus. It is strongly dependent from the different type of isotope. If the scattering centre is not at the origin but at a position r_i, an additional phase shift $\boldsymbol{q \cdot r_i}$ has to be added, providing $R >> r_i$. The quantity $\boldsymbol{q = k_o - k_f}$ is called the scattering vector, represented in figure 2.7 (b). Considering now the whole sample composed by N scattering centres i with a scattering length b_i each ones, the total wave function, at a distant point defined by $\boldsymbol{R}$, taken to be parallel to k_f where is placed a detector of area $dS << R^2$, can be written as

$$\psi_{scatt,N} = \frac{-\psi_0}{R} exp(ik_f R) \sum_{i=1}^{N} b_i exp(i\boldsymbol{q r_i}) \tag{2.5}$$

Taking into account the figure 2.7, the number of neutrons scattered per second in a given direction, i.e. into the small solid angle $d\Omega$ in the direction θ, ϕ is given by the **differential cross-section**

$$\frac{d\sigma}{d\Omega} = \frac{number\ of\ neutrons}{\Phi d\Omega} \tag{2.6}$$

where Φ is the flux of incident neutrons. By a suitable normalisation of the wave function, the incident flux can be written by $\Phi = v_0|\psi_{inc}|^2 = v_0\psi_0^2$ where v_0 is the average velocity of the incident neutrons which is equal to the velocity of neutrons after the scattering (due to the static approximation). The differential cross section for a single scattering centre can be obtained as

$$\frac{d\sigma}{d\Omega} = \frac{|\psi_{scatt,i}|^2}{|\psi_{inc}|^2 d\Omega} = \frac{(\psi_0^2|b_i|^2/R^2)(R^2 d\Omega)}{\psi_0^2 d\Omega} = b_i^2 \tag{2.7}$$

which gives an isotropic elastic scattering. Extending this relation for the whole sample composed by N scattering centres **the total differential scattering cross section** becomes

$$\frac{d\sigma}{d\Omega}(Q) = \langle \sum_{i,j}^{N} b_i \bar{b}_j exp(i\boldsymbol{q} \cdot \boldsymbol{r_{ij}}) \rangle \tag{2.8}$$

The total cross section σ_{tot} in the case of elastic scattering is obtained by integration of the differential cross section over the solid angles $d\Omega$

$$\sigma_{tot} = \int_{all\ directions} (\frac{d\sigma}{d\Omega}) d\Omega \tag{2.9}$$

where the vector $\boldsymbol{r_{ij}} = \boldsymbol{r_i} - \boldsymbol{r_j}$ gives the relative positions of scattering centres i and j. The brackets in equation 2.9 indicates that these positions are counted by means of an average due to the thermal displacement occurring during the scattering experiment.

2.4 Small-Angle Neutron Scattering

The elastic scattering allows to study the structure of crystalline or amorphous objects. This process takes place when there is no loss of energy during the interaction between the neutrons and the nuclei of the sample. Therefore the wave vectors of the scattered neutrons change their directions but maintaining their modulus. This kind of measure is performed by measuring the neutron scattering as a function of θ for all the angles ϕ, (in the case of isotropic scattering), see figure 2.7 (a). In this case the scattering vector

Q is defined as

$$Q = \frac{4\pi}{\lambda} sin(\theta) \tag{2.10}$$

where λ is the wavelength of the monochromatic neutron beam, θ is the diffusion angle. Practically all the instrument used for reflectometry, diffraction and SANS are built to measure this quantity within different ranges [9]. In figure 2.8 is illustrated the scheme of a typical SANS experiment.

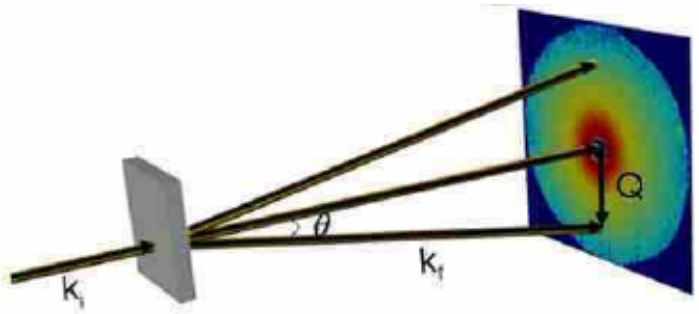

Figure 2.8: Scheme of a typical SANS experiment.

The scattering vector has two advantage respect to the θ notation: its does not depends from the wavelength of the probe (λ) and it has the dimension of the inverse of a length (usually Å^{-1}). In fact from the Bragg equation ($\lambda = 2dsin\theta$) is possible to obtain Q as

$$Q = \frac{2\pi}{d} \qquad (or\ eventually \quad d = \frac{2\pi}{Q}) \tag{2.11}$$

where d is the correlation distance of sampling observable through the scattering vector Q [10]. The scattering instrument is like a microscope working in the reciprocal space by means of a Fourier transformation lens. From equations 2.10 and 2.11, for a chosen wavelength, it is possible to find the accessible Q range and consequently the accessible d range, that defines the maximum and the minimum distances measurable in the SANS experiment.
The SANS technique has revealed to be an efficient investigation method for different field of research such as: biology, material science, polymers, complex fluids, micelles solution, etc. Taking into account a dispersion of spherical particles in a solvent, the scattering length of the whole sample changes within the volume V of the sample. In this case the macroscopic coherent differential cross section is commonly indicated as

$$\frac{d\Sigma}{d\Omega} = (\frac{N}{V})\langle V_p \Delta\rho \rangle^2 P(Q) S(Q) \tag{2.12}$$

where N/V is the particles density, V_p is the particle volume, $\Delta\rho^2 = (\rho_p - \rho_s)$ is the contrast factor where ρ_p and ρ_s are the scattering length density of the particles and

the solvent respectively [9]. $P(Q)$ and $S(Q)$ are the form factor and the structure factor respectively, which are better described later in section 6.5.

2.4.1 SANS Instrument

The geometry and architecture of a SANS instrument depends on the neutron source employed. For a fission neutron source, as is the case of the ILL, the SANS instrument is a steady-state instrument. At the ILL there are three SANS instruments which are called D11, D22 and D33.
For the present work, the instrument D11 has been employed to study historical potteries (see chapter 4). This instrument is located in the ILL 7 building, connected to the guide-hall 1 which receives neutron from the vertical source H15 (see figure 2.4 and 2.5). D11 is the archetype of a long, pinhole geometry instrument designed for the study of large scale structures in different scientific field as reported above [5]. The instrument is composed mainly by five parts as illustrated in figure 2.9. The first part of

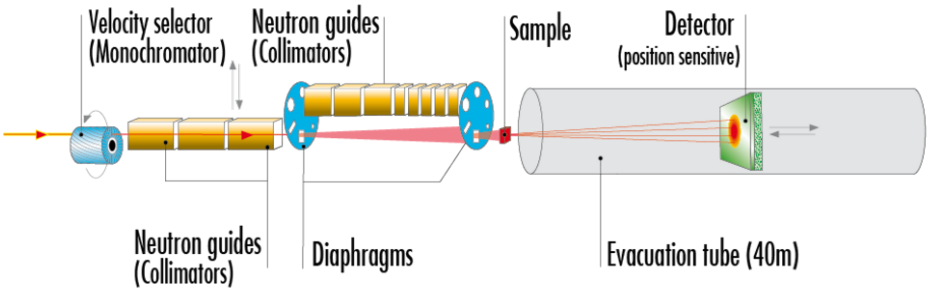

Figure 2.9: Illustration of the D11 instrument situated at the ILL 7 building [5].

the instrument from the left is the monochromator which select the wavelength (with a $\Delta\lambda/\lambda = 9\%$), through the selection of the neutrons velocity. It is a helicoidal turbine positioned far away from the reactor (∼100m) to reduce the noisy background, coming from the nuclear reaction inside the reactor. The neutrons are then collimated in the second part of the instrument by means of borosilicate glass guides. The third part of the instrument is composed by diaphragms (six different shaped holes). The sample holder is positioned 40 meters far from the monochromator, and may be equipped with different sample environments such as for example a temperature controlled sample changer, cryostat, magnet, etc. The last part of the instrument is the evacuation tube, a 40 m vacuum pipe. Inside this pipe there is the detector that can be moved to obtain different sample-to-detector distances (SDD) variable from 1.2m to 39m, that allows to extend the measurable Q range. The detector is a 96 x 96 cm^2 multi-detector screen (CERCA) filled with ^3He. The pixel size is 7.5 x 7.5 mm^2 [5].

Bibliography

[1] Bernard Jacort, *Neutron for Science*, **2006**.

[2] *Neutron data booklet*, 2nd ed, (Eds.: A. J. Dianoux, G. H. Lander, I. Laue-Langevin), Old City, Philadelphia, PA, **2003**, 1 p.

[3] *Studying Kinetics with Neutrons: Prospects for Time-Resolved Neutron Scattering, Vol. 161*, (Eds.: G. Eckold, H. Schober, S. E. Nagler), Springer Berlin Heidelberg, Berlin, Heidelberg, **2010**.

[4] J. M. Carpenter, W. B. Yelon in *Neutron Scattering*, (Eds.: K. Sköld, D. L. Price), Methods in Experimental Physics, ISSN: 0076-695X, Academic Press, **1986**, pp. 99–196.

[5] ILL web site, Library Catalog: www.ill.eu, `https://www.ill.eu/`.

[6] Instruments, `https://www.ill.eu/users/instruments/`.

[7] H. E. Fischer, A. C. Barnes, P. S. Salmon, *Reports on Progress in Physics* **2006**, *69*, 233–299.

[8] G. L. Squires, *Introduction to the Theory of Thermal Neutron Scattering*, 3rd ed., Cambridge University Press, Cambridge, **2012**.

[9] I. Grillo in *Soft Matter Characterization*, (Eds.: R. Borsali, R. Pecora), Springer Netherlands, Dordrecht, **2008**, pp. 723–782.

[10] R. Roe, *Methods of X-ray and Neutron Scattering in Polymer Science*, Oxford University Press, **2000**.

Chapter 3

Ceramic samples

Ceramics are complex objects rich source of information which constitute a large part of the sample memory of past and present human activities. Therefore the study of these materials is essential in order to thoroughly understand the materiality of historical events and their echo in the present.

3.1 Pottery in archaeology

Pottery is certainly a key element in cultural heritage field. In an archaeological site, the ceramic findings are considered as the most important set of data due to their large distribution. The constant manufacturing process, recycling of vessel and waste pieces found in the site lead to the creation of an archive of testimonies which faithfully record the changes in terms of mode of time, technical functions and symbols.
Ceramic's term refers to an object made by firing materials extracted from the Earth. Ceramics are actually an artificial form of stones. It is defined as a non-metallic inorganic solid and it is characterised by several properties, such as high hardness and strength, high melting point, low deformation under forces, corrosion and abrasion resistance and good electrical and thermal insulation [1]. Ceramic is one of the most ancient industry and its invention is the learning result of particular process: the handling clay and its change by means of the fire. The first clay-fired objects found in archaeological excavation were fragments of statuettes found in Czech Republic in the Moravian Basin. One of those statuettes was a female sculpture named "Venus of Dolni Věstonice", dated from 28000 and 24000 BCE [2].

3.2 Raw Materials

Ceramic paste is composed od naturally-occurring raw materials classified in two basic groups, represented by plastic (clay) and non-plastic (non-clay or fillers) materials.

3.2.1 Clay Minerals

Clay is the generic name for very fine grained, unconsolidated earthy minerals that are supple and pliable when wet, become hard and retain their shape when dried, and turn into a stony material, known as fired clay, when heated to red heat [3]. Clays represent the most important component of ceramic body and their amount generally range 40-60 in weight percentage. They include clay minerals and accidental minerals. Clay minerals are phillosilicates chemically constituted of the hydrous silicate of alumina based on $[(Si_2O_3)^{-2}]_n$ sheets and minor amount of impurities such as potassium, sodium, calcium, magnesium or iron. Clays main property is the plasticity when wet, that permit to shape the artifact, dry without excessive cracking and warping. These minerals have a sheet-like morphology made by the arrangement of two basic structures: tetrahedral corner-linked sheet (T) and octahedral edge-sharing sheet (O) [4]. Tetrahedrical and octahedrical monomers are equally oriented in the same direction, linked together through oxygen atoms. Almost all phyllosilicates, in addition to the oxygens linkages, have hydroxyl OH^- ions involved in a linkage to form the sheets that extend laterally, as shown in figure 3.1.

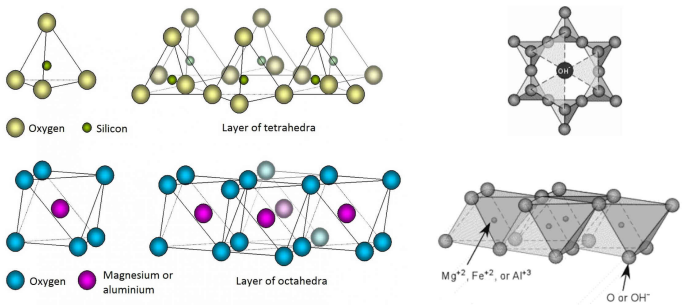

Figure 3.1: Tetrahedral and octahedral structure of phyllosilicates.

These two basic structures (T) and (O) could stack together forming seven different groups of phyllosilicates: kaolinite group, clay-micas group (or illite group), smectite group (or montmorillonite group), chlorite group, vermiculite group, allopane group, spiolite and palygorskite group In 3.2 are shown the principal five groups.

The main clay minerals involved in the ceramic production belong to the first three groups listed above. Due to this fact only these minerals are considered and described

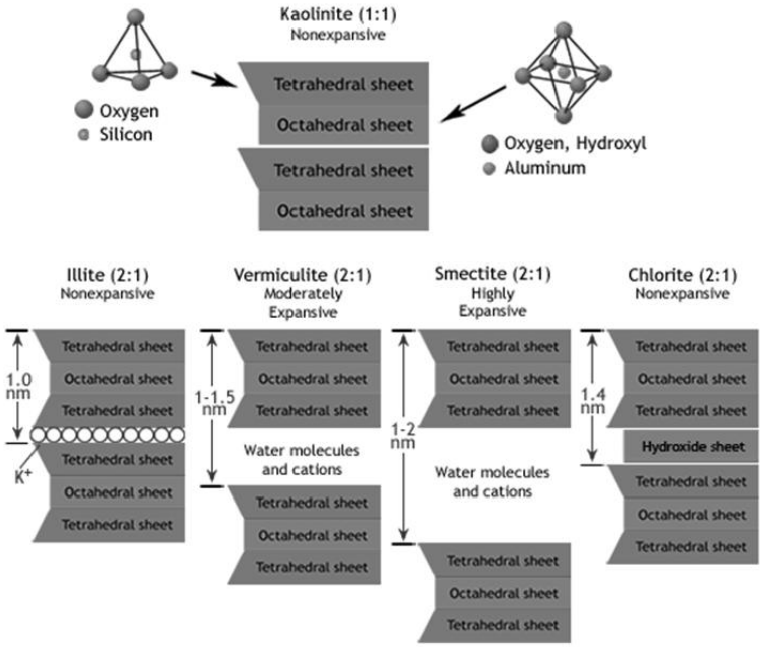

Figure 3.2: Five principal groups of clay's structure.

in more detail.

1. **Kaolinite group** present three different polymorphous forms: kaolinite, dickite and nacrite. The triclinic structure of kaolinite obtained from X-ray powder patterns was proposed by Brindley and Robinson (1945) [5]. Their proposed structure confirm that kaolinite is a dioctahedral 1:1 clay with a stoichiometric formula that is $Al_2Si_2O_5(OH)_4$. The structure of each unit cell is characterised by an alternation of T-O layers weakly bonded, without metal cations and water between the layers. Due to this structure the kaolinite results easy to be shutter and broken owning a low plasticity and low drying shrinkage.

2. **Illite group** often called clay-micas, is basically a hydrated muscovite. The illite mineral, which has a nominal formula $K_{0\cdot 88}Al_2(Si_{3\cdot 12}Al_{0\cdot 88})O_{10}(OH)_2$ is a non-expanding 2:1 clay with a crystal structure of T-O-T. Between the individual clay crystals poorly hydrated potassium cations are present which is responsible for the absence of swelling. Illite is the main component of shale and other argillaceous rock. It possess a good workability and plasticity.

3. **Smectite group** also called monmorillonite group, includes several minerals as montmorillonites which are a type of 2:1 dioctahedral phyllosilicates with the general formula: $(Al_{(2-y)}Mg_y)(Si_{(4-x)}Al_x)O_{10}(OH)_2M_{(x+y)}\cdot nH_2O$ where y>x and M represents inter layer exchangeable cations [6]. The structure is a complex T-O-T

sandwich in which water molecules surround cations as Na^{+}, Mg^{2+}, and Ca^{2+} forming swelled inter layers (with one to three layers of water molecule). Due to this the mineral obtain an excessive plasticity and strong shrinkage.

3.2.2 Non-Clay Materials

The term non-clay materials indicate raw materials which do not posses plastic properties when mixed with water. These materials are already naturally present in clay and the pottery during the manufacturing process intentionally adds more amount of them to modify the final characteristic of the artefact in the way to reduce high plasticity and/or shrinkage of the body when drying or firing. They include quartz, feldspar, limestone, iron hydroxides and oxides and minor compounds. Non-clay materials are both artificial or natural compounds and can be divided in three main groups, basing on their function in the ceramic production.

1. The first group includes inert tempers, able to reduce plasticity and shrinkage after drying and providing structure to the artefact because they do not absorb water. The main components are: quartz, micas, feldspars and the artificial temper called chamotte.

2. The second group consists of fluxes and binders that affect firing process and chemical-physical transformations. As a result, new mineral phases as complex silicates can be formed with lower melting point. These components are: calcite, iron oxides and hydroxides as hematite, magnetite and limonite.

3. The third group is represented by accidental materials: organic compounds, fossil, flint fragments, heterogeneous materials, etc.

3.3 Production Technology

Ceramic production involves the following basic steps:

- procuring and selecting the raw materials (clay and non-clay);
- preparing the clay paste mixing raw materials and water;
- shaping and modelling the paste into object;
- drying the object;
- surface treatments;

- firing the object into a klin.

The raw materials come from natural deposit in mine and/or deposited clay along river courses. For these reason raw materials have to be purified, to obtain pure powder with low content of impurities. This process involves the reduction of particle size by crushing and fine grinding to produce a homogeneous paste and to liberate the impurities, removed by washing with water and filtering. Potters that can add particular tempers to the paste to alter the original properties of the clay changing the chemical, mineralogical and morphological features of the artefacts.

3.4 Firing procedure

Firing process is a critical step in production technology of pottery because during the heating process at high temperature chemical and physical transformations take place, changing characteristic of pottery. The minimum temperature in order to obtain an irreversible transformation process, is between 550 - 600 °C; actually above 700 °C a ceramic artefact is considered fired, and may simple potteries are fired at that temperature [3]. All the several reactions occur during the firing process, that form new mineral phases from those which decompose, can be divided in three phases:

- oxidation (100 - 400 °C);
- dehydration (450 - 600 °C);
- incipit of vitrification, including baking and burning (above 600 °C).

3.4.1 Types of Fired Ceramics

Firing temperature reached in the kiln are able to distinguish, together with chemical and mineralogical composition, different types of fired ceramics. In fact, the chemical and physical transformations are dependent on temperatures and mineralogy of the raw materials. The physical properties most often used for the characterisation of ceramic materials are porosity, translucency, strength and colour. Porosity indicates the relative amount of voids within a material, measured as the amount of water that the material absorbs and is expressed as a percentage of total volume taken up by voids,

$$Porosity = \frac{V_{\mathrm{v}}}{V_{\mathrm{tot}}} = \frac{\rho_{\mathrm{particle}} - \rho_{\mathrm{bulk}}}{\rho_{\mathrm{particle}} - \rho_{\mathrm{fluid}}} \tag{3.1}$$

where V_{v} is the volume of voids, ρ_{particle} is the particle density or true density of a particulate solid or powder, ρ_{bulk} is the average density of a large volume of powder

in a specific medium and ρ_{fluid} the density of the fluid medium in which the porous object is measured. The porosity of ceramic materials is determined mainly by the nature of the raw materials used and the degree of vitrification the object underwent when fired [3]. In 3.1 are listed the four types of ceramics classified by means of their physical characteristic.

A more detailed distinction of these type of ceramics is reported below.

- Terracotta (T < 900 °C) is the simplest and coarsest type of pottery. It is very porous, lightweight, typically red-coloured and it is fired at temperatures below 900 °C. Much of ancient pottery, for example is of the terracotta type. Because of the relatively low temperature at which it is fired, terracotta is only slightly vitrified and consequently is highly porous and totally opaque. The colour of most terracotta fired under oxidising conditions is either red, brown, or yellow, the intensity of the colour is dependent on the relative amount of iron oxides (oxidising condition defines the presence of oxygen inside the firing chamber and so directly in contact with the ceramic object).

- Earthenware is obtained when the same ceramic paste used for the terracotta is fired at higher temperature (above 950 °C). In this way the ceramic object results more vitrified, less porous (5-10%) and stronger than terracotta. Two particular types of earthenware, among many others, are majolica and faience.

- The traditional stoneware has a dense ceramic body obtained by firing a fine-grained raw materials between 1100 - 1300 °C. It posses a high degree of vitrification and a low porosity. The higher firing temperature account for the much grater hardness and strength of stoneware over earthenware.

- Porcelain is fired at relatively high temperature (1300 - 1450 °C) forming a mixture of glass and crystalline phases ceramic body with a very low porosity (less than 2%). It can be distinguished from stoneware for its translucent optical characteristic rather than opaque.

3.4.2 Firing Process: Chemical and Physical Reactions

Firing is a process that irreversibly change the structure of clay in a new chemical and mineralogical composition, whit a different physical and microstructural features. The final of firing process is that the clay is converted to a new hard and rigid ceramic material. When clay is fired at a high temperature (above 600 °C), it undergoes profound

Table 3.1: The four main type of ceramics classified through their physical characteristics [3]

Material	Firing temperature [°C]	Porosity [%]	Optical characteristics
Terracotta	< 900	> 25	Opaque
Earthenware	> 950	< 10	Opaque
Stoneware	1100 - 1300	< 5	Opaque
Porcelain	1300 - 1450	< 2	Translucent

chemical changes on its matrix depend on the firing strategy adopted during the synthesis. The parameters controlled in the firing strategy are generally, firing temperature, atmosphere conditions, firing duration and fuels. The firing temperature plays a fundamental role in the dynamic aspect of the process, thus in developing new mineral phases, depending also on the raw material composition [7] Table 3.2 summarises the chemical changes that take place when clay is heated [3]

Table 3.2: Summary of the changes caused by heating the clay. RT = room temperature.

Temperature (°C)	Changes
RT - 100	Drying: loss of the water of formation
100 - 500	Loss of the water of plasticity
500 - 600	Dehydration: loss of chemically combined water and modification of clay structure
600 - 900	Breakdown of clay structure and incipient vitrification
900 - 1700	vitrification and formation of new structure
> 1700	Melting

Chemical and mineralogical changes are strongly connected to morphological and structural adjustments. The reactions occurring through the firing clay paste for the different range of temperature are reported below.

50°C - 200 °C

Above 100°C the water physically adsorbed in the clay paste evaporates. Above 105°C the chemisorbed water or bonded H_2O is removed [8]. This means that inter-layer water adsorbed in the lamellar structure and the ones trapped in the micro pores exit from the matrix as steam. The evaporation of water produces porous microstructure and a dilatation of the material.

200°C - 700 °C

In this step of temperature different reactions occur. The organic matter in the ceramic matrix is completely combusted producing CO_2, CO and carbon, depending on the at-

mosphere conditions, increasing the porosity. The chemisorbed water is still removed until 500°C. Above 500°C hydroxyl groups are removed as the dehydroxylation of bonded water take place. The temperature at which the dexydroxylation initiates depend upon the structure of the clay matrix i.e. on the type of minerals and the firing conditions [6]. This reaction provokes significant shrinkage of the matrix of ceramic object that is supported from the non-clay minerals acting as a skeleton [9]. The most used clay minerals in the manufacture of ceramics are kaolinite, montmorillonite and illite, and as such, their dehydroxilation reactions are widely studied because central in the process.

1. **Kaolinite** between 450 - 600 °C loses hydroxyl units which migrates from the inner to the exterior and dehydroxilates endotermically [10]. Starting from this temperature range, Kaolinite reorganise forming metakaolinite until 950 °C. At this point the interlaminar channels that allow water to be removed are blocked resulting in some residual OH in the ceramic [11]. The next phase transition occurs from 950 °C to 1100 °C when the spinnel is formed, followed by the complete conversion in mullite at 1100 °C.

2. **Montmorillonite** dehydroxylate when a proton moves from one hydroxyl to an adjacent hydroxyl to form a water molecule and aluminium cations coordinate to the remaining oxygen [6]. The dehydroxylation starts at 500 - 550 °C forming a stable dehydroxylated phase that preserve partially the crystal structure of the original clay minerals until its structure collapses, at around 900 °C.

3. **Illite** begins to dehydroxylate at 450 - 600 °C and its skeleton persist still it breaks down between 700 and 850 °C. It continues to dehydroxylate until a complete conversion to metakaolinite occurs at 950 - 1100 °C.

At 500 - 700 °C the temperature is high enough to avoid rehydration and the clay become a plastic structure which clay particles are permanent bonded. At 573 °C quartz undergoes a reversible phase transition (α to β), accompained by a 7 vol% change [12].

700°C - 900°C

From around 650 °C to 850 °C carbonates as calcite $CaCO_3$ (that is the most common carbonate) or dolomite $CaMg(CO_3)_2$ start to decompose in their metal oxides MO where M is Ca or Mg, releasing CO_2 with an increment of the porosity. The oxides thus produce are reactive and they can form new phases reacting with other compounds or absorbing atmospheric water producing $M(OH)_2$ as shown below in (3.2), (3.3). At 870 °C the second change of quartz take place from β-quartz to tridymite, without affecting the structure of the ceramic body [12].

$$CaCO_3 \longrightarrow CaO + CO_2\uparrow \qquad CaO + H_2O \longrightarrow Ca(OH)_2 \quad (3.2)$$

$$CaMg(CO_3)_2 \longrightarrow CaCO_3 + MgO + CO_2\uparrow \qquad MgO + H_2O \longrightarrow Mg(OH)_2 \quad (3.3)$$

900°C - 1100 °C

During this transition in temperature the crystalline lattice of clay minerals is destroyed and new high-temperature crystalline phases are formed. The transformation reactions involve carbonates, calcium oxides and silicate as is reported in reactions (3.4), (3.5), (3.6), (3.7) and (3.8) [13]. The main products of these reaction are gehlenite ($Ca_2Al_2SiO_7$), diopside ($CaMgSi_2O_6$), wollastone ($CaSiO_3$) and anorthite ($CaAl_2Si_2O_8$).At the end of this range of temperature all the three principal components of the ceramic listed in the last paragraph are completely dehydroxylated. When the temperature is high enough, the sintering and vitrification processes begin. There

at 650 - 950 °C : reaction of dehydroxylation

$$\underset{\text{kaolin}}{Al_2Si_2O_5(OH)_4} \longrightarrow \underset{\text{metakaolin}}{Al_2Si_2O_7} + 2\,H_2O \quad (3.4)$$

at 650 - 950 °C

$$\underset{\text{metakaolin}}{Al_2Si_2O_7} + 3\,CaO \longrightarrow \underset{\text{ghelenite}}{Ca_2Al_2SiO_7} + \underset{\text{wollastone}}{CaSiO_3} \quad (3.5)$$

$$\underset{\text{quartz}}{2\,SiO_2} + \underset{\text{dolomite}}{CaMg(CO_3)_2} \longrightarrow \underset{\text{diopside}}{CaMgSi_2O_6} + 2\,CO_2\uparrow \quad (3.6)$$

at 1000 °C

$$\underset{\text{ghelenite}}{Ca_2Al_2SiO_7} + \underset{\text{metakaolin}}{Al_2Si_2O_7} + \underset{\text{quartz}}{3\,SiO_2} + 2\,CaO \longrightarrow 2\,\underset{\text{anorthite}}{CaAl_2Si_2O_8} + 2\,\underset{\text{wollastone}}{CaSiO_3} \quad (3.7)$$

$$\underset{\text{gehlenite}}{Ca_2Al_2SiO_7} + 2\,\underset{\text{quartz}}{SiO_2} \longrightarrow \underset{\text{anorthite}}{CaAl_2SiO_8} + \underset{\text{wollastone}}{CaSiO_3} \quad (3.8)$$

is a development of a partial fusion of the grains and the reduction of their dimension which produce a reduction in the porosity and an increasing in the hardness of ceramic. Alluminium mineral as mullite ($Al_6Si_2O_{13}$) which appears with a needle-shape plays the role of a skeleton increasing the strength and reducing the deformation during formation of the glassy phase. The presence of fluxes compound, such as calcium oxides and potassium oxides present in illite mineral, encourage the sintering and vitrification processes. In these processes particle surface begin to fuse and stick to others, pores become more spherical till they are eliminated increasing the density.

Glass formation usually begins at around 1100 °C and the loss of open porosity with the development of closed ones occurs causing physical changes as shrinkage.

Bibliography

[1] M. Vidale, *Ceramica e archeologia*, (Ed.: Carocci), **2007**.

[2] Giulia Ricci, PhD thesis, Ca'Foscari Venezia, **2016**, 203 pp.

[3] Zvi Goffer, *Archaeological Chemistry*, Google-Books-ID: TcYTNyWQM2QC, John Wiley & Sons, **2006**, 654 pp.

[4] B. Mason, L.G. Berry, *Mineralogical Magazine* **1969**, *37*, 304.

[5] G. W. Brindley, K. Robinson, *Nature* **1945**, *156*, Number: 3970 Publisher: Nature Publishing Group, 661–662.

[6] C. M. Stevenson, M. Gurnick, *Journal of Archaeological Science* **2016**, *69*, 54–63.

[7] M. P. Riccardi, B. Messiga, P. Duminuco, *Applied Clay Science* **1999**, *15*, 393–409.

[8] V. A. Drits, D. K. McCarty, *Clays and Clay Minerals* **2007**, *55*, 45–58.

[9] D. Albero Santacreu, *Materiality, Techniques and Society in Pottery Production: The Technological Study of Archaeological Ceramics through Paste Analysis*, De Gruyter Open Poland, **2014**.

[10] P. Zemenová, A. Kloužková, M. Kohoutková, R. Král, *Journal of Thermal Analysis and Calorimetry* **2014**, *116*, 633–639.

[11] Andres Ortega, M. MacÃas, F. J. Gotor, *Journal of the American Ceramic Society* **2010**, *93*, 197–203.

[12] L. Campanella, *Chimica per l'arte*, (Ed.: Zanichelli), **2007**.

[13] C. Mondelli, S. Zorzi, G. Ricci, V. Galvan, E. Balliana, R. Schweins, E. Cattaruzza, *ChemPhysChem* **2020**, *21*, 966–970.

Chapter 4

Samples and Previous Characterisations

The samples involved in this work were previously analysed in the PhD thesis of Dr. Giulia Ricci with different techniques which are listed below [1]. This chapter reports the main results of her work, necessary to support and understand the work done with neutrons. For the neutron investigation, only a part of samples coming from the excavation sites were measured and analysed. In the next pages a summary of the principal results has been reported taking into account only the samples measured with neutrons.

- Fourier-Transform Infrared Spectroscopy (FT-IR),
- Micro-Raman Spectroscopy (μ-Raman),
- Laser Induced Fluorescence Spectroscopy (LIF),
- Ultraviolet-Visible Spectroscopy (UV-Vis),
- Laser Induced Breackdown Spectroscopy (LIBS),
- X-Ray Fluorescence Analysis (XRF),
- X-Ray Diffractometry (XRD),
- Scanning Electron Microscope coupled with Energy Dispersive X-Ray Probe (SEM-EDX),
- Mercury Intrusion Porosimetry (MIP),
- Micro-Computed X-ray Tomography (μ-CT).

4.1 Characterisation of Mediterranean Ceramic Samples

The Mediterranean-named ceramics samples were obtained from excavations at Torcello, an island of the Venetian Lagoon in the 2012 -2013. These ceramic shreds came from the Mediterranean basin and are attributed to three main groups related to their stratigraphic dating: Late Antiquity (5^{th}-7^{th} centuries), Early Middle Ages (8^{th}-10^{th} centuries) and Middle Age (10^{th}-12^{th} centuries). All of these ceramic samples (apart from two of them) belong to shreds of globular amphorae mainly involved in the trade of goods. These ceramic shreds can be divided into two groups briefly described below:

1. **Late Antique Amphora** are mostly produced in the North African region, in particular in the Eastern Mediterranean as Egypt, Syrian-Palestinian Region, Turkey, Asia Minor and Aegean.

2. **Early Medieval Globular Amphorae** come from the South-Eastern part of the Mediterranean region, in particular Northern Aegean and coasts of Black Sea.

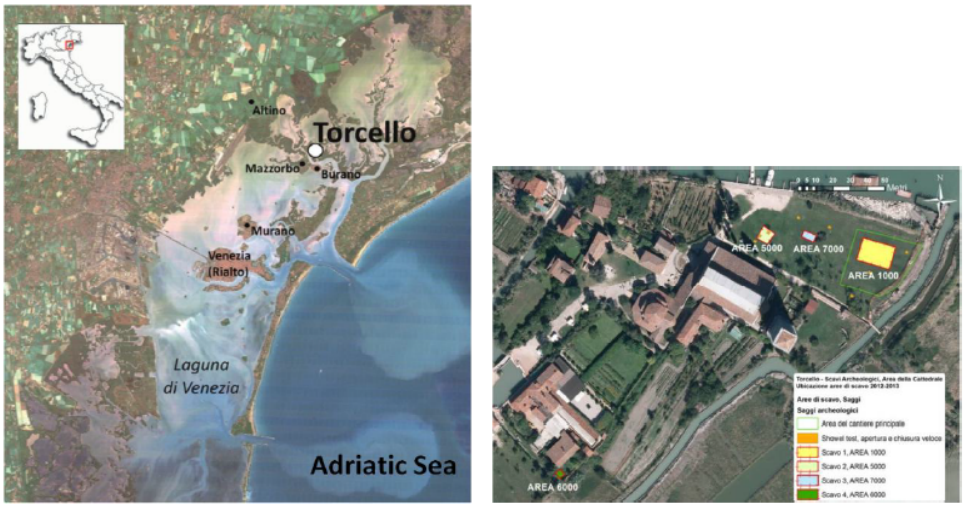

(a) Geographical location of Torcello island in the Venetian Lagoon [1]

(b) Location of the excavated areas in Torcello. Only samples coming from 5000 and 1000 sites were analysed in this thesis.

Figure 4.1: Pictures of the Torcello island in the Venetian lagoon (a) and of the excavation sites (b).

These ceramic shreds were obtained from two different excavation sites in the Torcello island (see figure 4.1), named as "1000" and "5000". The codes of the Mediterranean

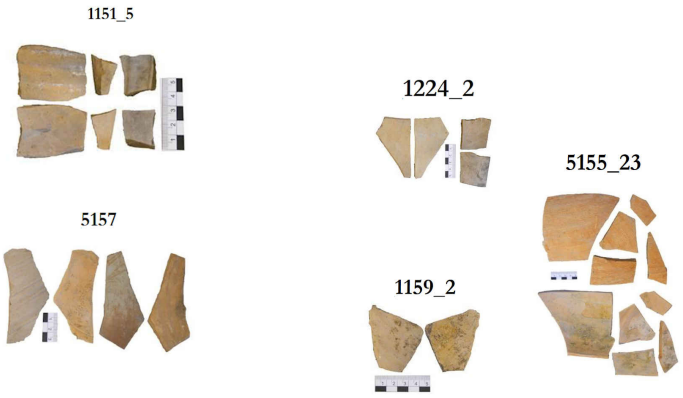

(a) Late Antique Amphorae (b) Early Medieval Globular Amphorae

Figure 4.2: Pictures of some Mediterranean ceramic shreds obtained from the excavation in Torcello (Italy).

samples refer to the two excavation sites (and they have archaeological meaning only). All the samples involved in the neutron analysis are showed in figure 4.2.

4.1.1 Previous Characterisations

Chemical characterisation of the archaeological shreds was carried out by means FT-IR and μ-Raman spectroscopy, where mineralogical attributions were performed on the basis of the data reported in literature.

FT-IR

spectroscopy allowed to identify the chemical composition of the samples and the most significant spectra are reported in figure 4.3. The obtained results showed similar chemical-mineralogical composition of the ceramic fragments mainly composed of:

1. **Quartz**:
   - Si−O stretching (1064-1089 cm^{-1});
   - Si−O symmetric stretching (794-800 cm^{-1}, 770-780 cm^{-1});
   - Si−O bending mode (685-699 cm^{-1}) [2, 3].
2. **Calcite** detected from CO_3^{2-} overtones/combination bands:
   - symmetric 1795-1797 cm^{-1};

- asymmetric 1452-1478 cm^{-1};
- 1421-1442 cm^{-1};
- asymmetric 874-875 cm^{-1};
- 711-720 cm^{-1} [4].

3. **Smectite (montmorillonite)**:

- O−H stretching band (centered at around 3400-3440 cm^{-1}) [3];
- Si−O stretching (1040-1049 cm^{-1});
- Si−O−Si banding (471-470 cm^{-1}) [5].

4. **Kaolinite**:

- Si−O−Si stretching (1030-1037 cm^{-1});
- Si−O stretching (1008-1016 cm^{-1});
- Al−OH stretching (900-933 cm^{-1}) [3].

5. **Feldspars**:

- Al−O−Si bending (727-733 cm^{-1});
- Si−O−Si benging (634-648 cm^{-1}) [6].

6. **Iron Oxides** detected through hematite and magnetite signals:

- hematite (536-557 cm^{-1});
- hematite (469-479 cm^{-1});
- magnetite (575-580 cm^{-1}).

The presence of the band related to the stretching vibration of –OH in Smectite, may indicate a firing temperature lower than 900 °C, because above this temperature montmorillonite dehydroxylates producing spinel and/or other firing products not detected in the analysed samples. Some samples showed different peaks in their FT-IR spectrum, may be due to the presence of gypsum rehydrated during burial period. Gypsum in ceramic body might be present as impurity in the clay minerals or, more probably, an alteration product due to the reactions involving the released sulphate anions and Ca^{2+} either present in water or derived by dissolution of secondary calcite [4]. The presence of gypsum as post-burial alteration detected through its −OH stretching band may interfere in estimating the firing temperature due to its overlapping with the hydroxyl signal of other minerals. Mediterranean ceramic shreds were

divided in sub-groups, further subdivision than that proposed by archaeologists (Late Antique and Early Medieval groups), on the basis of the presence of primary or secondary calcite as it is reported in table 4.1. The presence of calcite, even if secondary, and the absence of IR bands related to Ca-silicates phases (such as gehlenite, wollastonite, diopside and anorthite) suggest firing temperature lower than 900 °C, probably in the range of 700 - 850 °C. [7]. The presence of both hematite and magnetite indicate respectively an oxidising and a reductive atmosphere, which could confirm a variable atmospheric conditions during firing process.

Table 4.1: Sub-groups in the basis of the presence of primary and secondary calcite.

	Late Antique Amphorae	Early Medieval Globular Amphorae
Primary calcite	5157	1154_10, 1188_4, 1159_2, 1224_2, 1155_1
Secondary calcite	1151_5	5155_23, 1210_1, 1167_1, 1154_8

µ-Raman

analyses were performed on the ceramic body of the selected Mediterranean fragments previously embedded in polyester resin and then polished in order to obtain a flat surface. The results show a similar chemical composition for the Mediterranean samples. The main detected mineralogical phases are: **quartz**, **anatase**, **kaolinite**, **montmorillonite**, **illite**, **feldspars**, **hematite**, **gypsum**, **calcite**.

The presence of both montmorillonite and illite confirms the firing temperature inferred by FT-IR results.

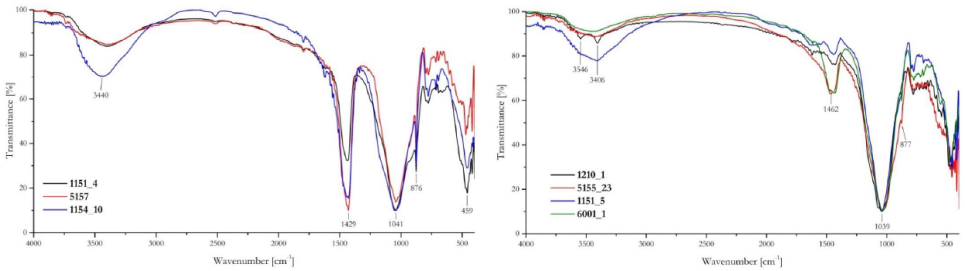

(a) primary calcite (b) secondary calcite

Figure 4.3: FT-IR spectrum of selected Mediterranean ceramic samples belonging to the two sub-group based on the presence of calcite.

SEM-EDX

technique was involved to obtain morphological and microstructural information about the ceramic matrix of selected samples. Microphotographs obtained by electron microscope allowed the evaluation of firing conditions, considering the textural features of the ceramic bulk related to firing temperature, as well as the chemical and mineralogical composition [8]. All the analysed samples show distinct and separated grains in the clay matrix, where the slightly deformed edges may indicate a beginning of vitrification process which starts at 700 °C. The results for the selected samples are shown in figure 4.4.

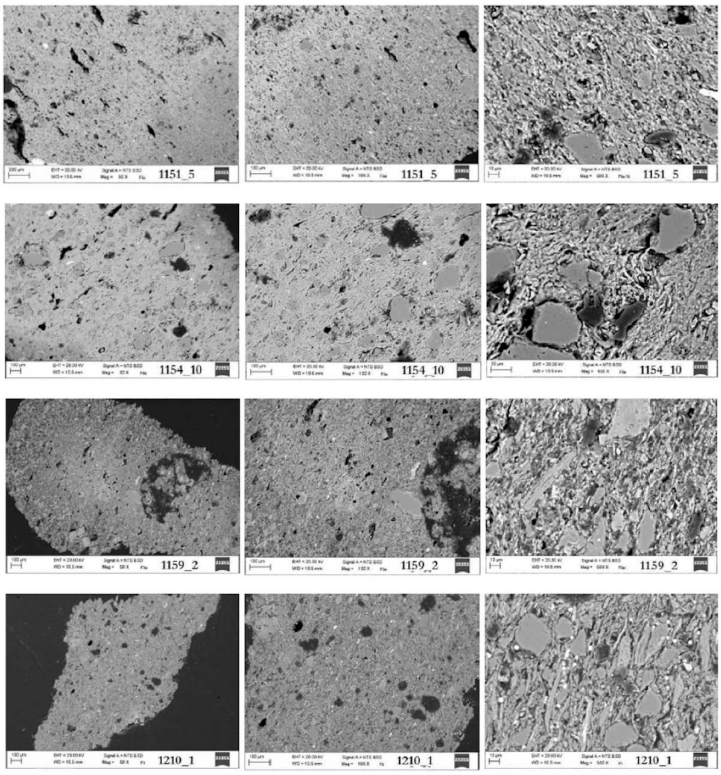

Figure 4.4: SEM images at magnification of 50x, 100x and 500x (from left to right) of Mediterranean shreds.

From these microphotographs is possible to notice that 1151_5, 1154_10 and 1159_2 samples exhibit a high density matrix. Integrating these results with the observations obtained from the chemical and mineralogical analyses (i.e. FT-IR and μ-Raman analyses) it's possible to conclude that these samples may be fired at around 800 - 850 °C. The firing temperature has to be lower than 900 °C because of the presence of calcite. The 1210_1 sample exhibits a clay matrix not molten with a low densification stage and the absence of glassy phase suggest low firing temperature, between 700 °C and 800 °C. At a low degree of magnification, the microphotographs of 1154_10 and 1159_2

samples seem to have a directional elongated-shape porosity which may be due to the forming technique adopted, while 1210_1 sample exhibit an arbitrary rounded-shape porosity. Elemental analyses for chemical elements of interest, such as **Al, Ca, Fe, K, Mg, Na, Si, Ti, S** were performed in order to provide insight on the mineralogical composition of the ceramic body with the joint of EDX punctual analyses. Chemical composition for three representative ceramic fragments is reported in table 4.2.

Table 4.2: SEM-EDX analyses of three Mediterranean shreds.

	1151_1 [%]	1159_2 [%]	1210_1 [%]
SiO_2	55.61	45.69	51.95
Al_2O_3	23.23	21.29	18.04
TiO_2	1.15	2.28	1.93
Fe_2O_3	1.15	2.28	1.93
Na_2O	5.20	6.00	3.16
MgO	0.38	0.87	0.73
K_2O	1.69	3.02	3.48
CaO	3.72	4.18	3.50
PbO	1.41	1.32	3.07
SO_3	2.23	4.66	7.01

MIP and µ-CT

analyses (which are the acronyms for Mercury Intrusion Porosimetry and X-ray Micro-Computed Tomography respectively) were carried out to obtain information about different aspects of the porosity of ceramic samples. The first one provides informa-

Table 4.3: Porosity data obtained by MIP measurements of Mediterranean shreds.

Sample	Total cumulative pores' volume [cm3/g]	Average pore radius [µm	Total porosity [%]	Bulk density [g/cm3]
1210_1	0.16 ± 0.03	0.2 ± 0.1	18 ± 2	1.16 ± 0.06
1159_2	0.26 ± 0.02	0.17 ± 0.01	28 ± 3	1.10 ± 0.05
1154_10	0.21 ± 0.01	0.25 ± 0.01	25 ± 2	1.16 ± 0.07
1155_1	0.10 ± 0.03	0.3 ± 0.1	15 ± 8	1.5 ± 0.4
1151_5	0.16 ± 0.03	0.15 ± 0.03	21 ± 8	1.6 ± 0.2
5157	0.22 ± 0.02	0.15 ± 0.05	34 ± 4	2.3 ± 0.5

tion on open macro and meso porosity between 0,01 to 10 µm while the second on

total (open and closed) porosity between 1 to 100 µm, both allow quantitative investigation. Porosity is a microstructural feature that connect both physical properties and production technique of a ceramic object [9]. Total open porosity (%) of the analysed shreds ranges between 15 to 34 % with a mean value of (23 ± 2) % and the average pore radius between 0,15 to 0,27 µm with a mean value of (0.20 ± 0.02) µm. In table 4.3 are reported the data obtained from MIP analysis for Mediterranean ceramic shreds. In Figure 4.5 and figure 4.6 are reported the cumulative pore volume and volume distributions of open porosity for selected Mediterranean shred. From the obtained MIP results it can be difficult a discrimination of the samples in base on the technological productions, however it can be notice that there are some correlation between the chemical-mineralogical composition and porosimetry results. On the basis of this correlation three group were differentiated.

1. The shreds which exhibit higher values in the unimodal pore size distribution and total cumulative pore volume are 1159_2, 1154_10 and 5157. These samples includes even primary calcite, detected by FT-IR technique which begins its decomposition due to the firing temperature at around 800 - 850 °C, forming voids.

2. 1210_1 and 1151_5 samples show lower values of the unimodal pore size distribution curves and includes secondary calcite. It might be explained by the formation of calcite crystals into the ceramics after the firing process, which may occupy part of the matrix voids.

3. 1155_1 shred present a variable pore size distribution curves, indicating a high value of heterogeneous and is characterised by a low value of total cumulative pore volume. This sample include primary calcite. The trend of these two quantities obtained from MIP, might be due to the composition of the raw materials (low calcite content) and/or low firing temperature between 700 - 800 °C, which did not allow the de-carbonation process of all the calcite crystals present in the matrix.

Four selected samples were analysed by means of µ-CT in order to investigate the total porosity in the range between 1 and 100 µm. The pore volume of both open and closed pores versus their radius distribution is reported in figure 4.7. The analysed samples show unimodal pore distribution curves and their peak related to the mean pore radius ranges between 19 and 25 µm.

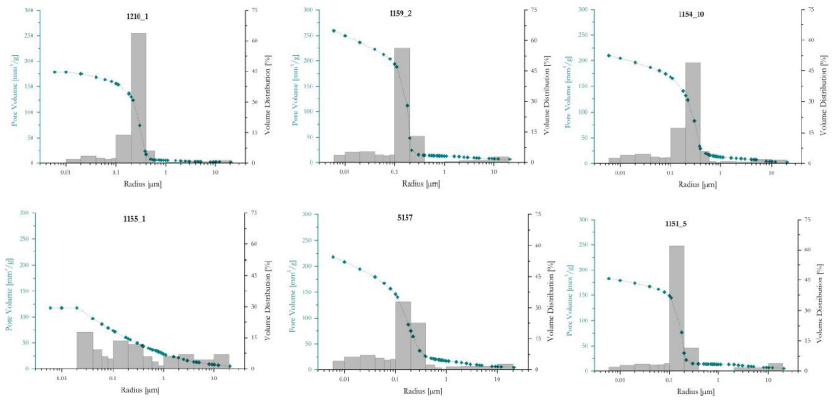

Figure 4.5: Cumulative pore volume and volume distribution versus pore radius of selected Mediterranean shreds.

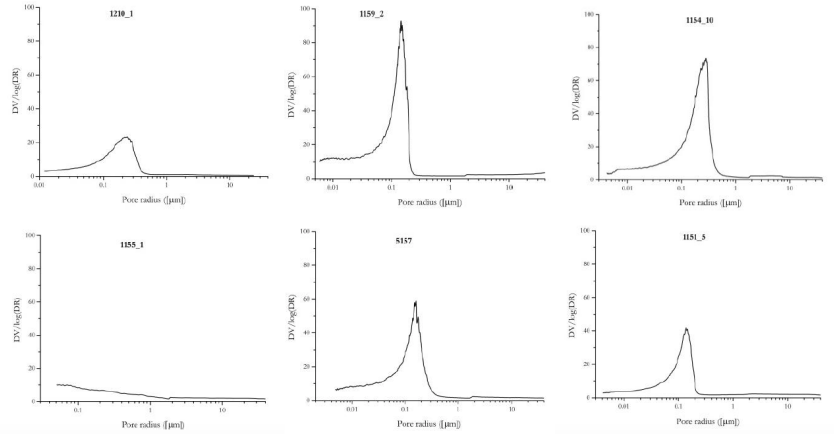

Figure 4.6: Pore size distribution curves versus pore radius of selected Mediterranean shreds.

1154_10 and 1159_2 shreds which includes primary calcite exhibit lower total porosity than that of 1210_ and 1151_5 samples, which instead includes secondary calcite. It has to be stress that the values obtained from µ-CT, accounting for both open and closed pores, cannot be compared with those obtained from MIP analyses, regarding only the open pores. Otherwise the measured µ-CT pores extend in a different range of dimension than those measured with MIP.

Conclusions

The multi-analytical approach representing the PhD work of Dr. Giulia Ricci, gives an estimation of the firing condition as well an evaluation of the chemical and mineralogical composition of Mediterranean samples, essential for the neutron study. All Mediterranean samples present a similar chemical and mineralogical composition and a low firing temperature 700 - 800 °C (1210_1 and 1151_5) and 800 - 850 °C (1154_10,

1159_2, 1151_1 and 5157). Late Antique and Early-Medieval globular amphorae are not distinguishable from a chemical and microstructural point of view. The presence of calcite mineral made possible to divide the ceramic samples in two alternative subgroups, based on the presence of primary calcite (coming from the raw materials) and the presence of secondary calcite as crystals reformed after firing during the burial period. The multi-analytical approach brings out the connection between the porosity and both firing temperature and mineralogical composition of the samples.

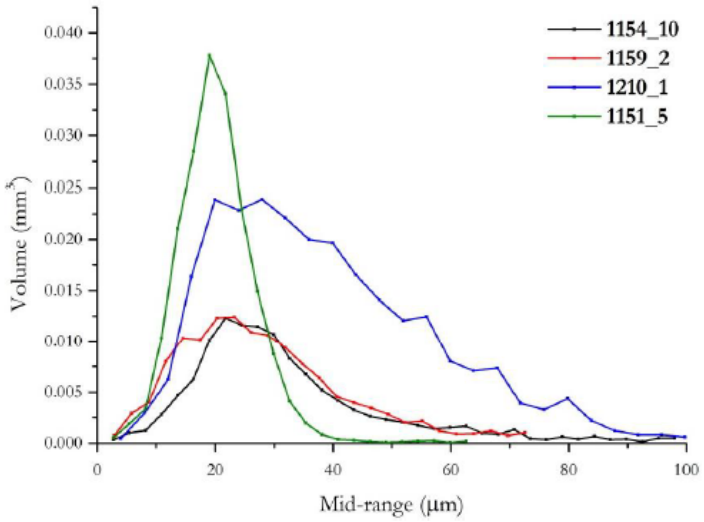

Figure 4.7: Distribution of pore volume vs pore radius, calculated through the results obtained from µ-CT analyses.

4.2 Characterisation of German Ceramic Samples

The German ceramic group of samples is composed of ceramic shreds dating from the late 13^{ht} to 19th century, coming from several excavation sites located in the Central and Eastern Germany. The group includes: stoneware, near-stoneware, unglazed earthenware and glazed earthenware that are provided from Landesamt für Archäologie Sachsen in Dresden (for information about the type of ceramics see chapter 3). The different excavation sites from which the German samples come from are: **Bautzen, Bischofswerda, Brandis, Bürgel, Coppengrave, Cottbus, Duingen, Görlitz, Kamenz, Grossalmerode**, see figure 4.8. An example of some ceramic shreds which are then analysed with neutrons are showed in figure 4.9. In Germany The production of dense sintered ceramics (i.e. stoneware-like ceramics) can be traced since around 1250, in the geographical area of Central and North Europe, especially in German. Similar manufacturing condition for ceramic material can be found only in China, where the devel-

Figure 4.8: Excavation sites located in the Central and Eastern Germany. In the picture are reported even sites from which ceramics samples not analysed with neutron techniques were recovered.

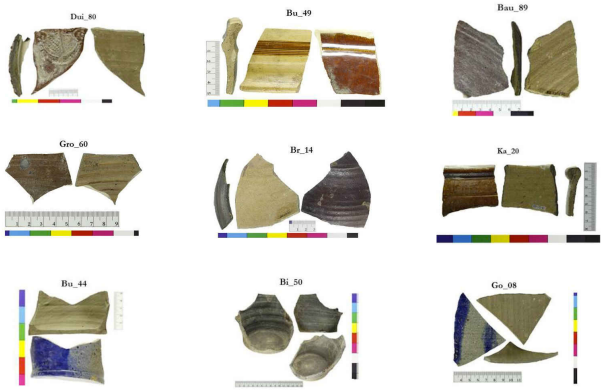

Figure 4.9: picture of some German shreds obtained from different excavation sites in Central-Eastern Germany.

opment of stoneware began in the middle of the second millennium BC [10]. Actually, the German stoneware was a production model for the neighbouring regions, representing commercial and cultural exchange material even over international boundaries, due to their properties as extremely hard body, water-repellent i.e. suitable for food and trade purpose. German stoneware is the result of firing at high temperature special and rare clay from the Tertiary period, found only in a few deposits near Coppengrave, Bengerode and Duingen (Lower Saxony, Germany).

4.2.1 Previous Characterisations

German samples were analysed with the same techniques involved in the study of Mediterranean samples, listed at the beginning of chapter 4.

FT-IR

results which are reported below concern only the German ceramic samples analysed with neutron techniques. The IR signals connected to the different minerals present

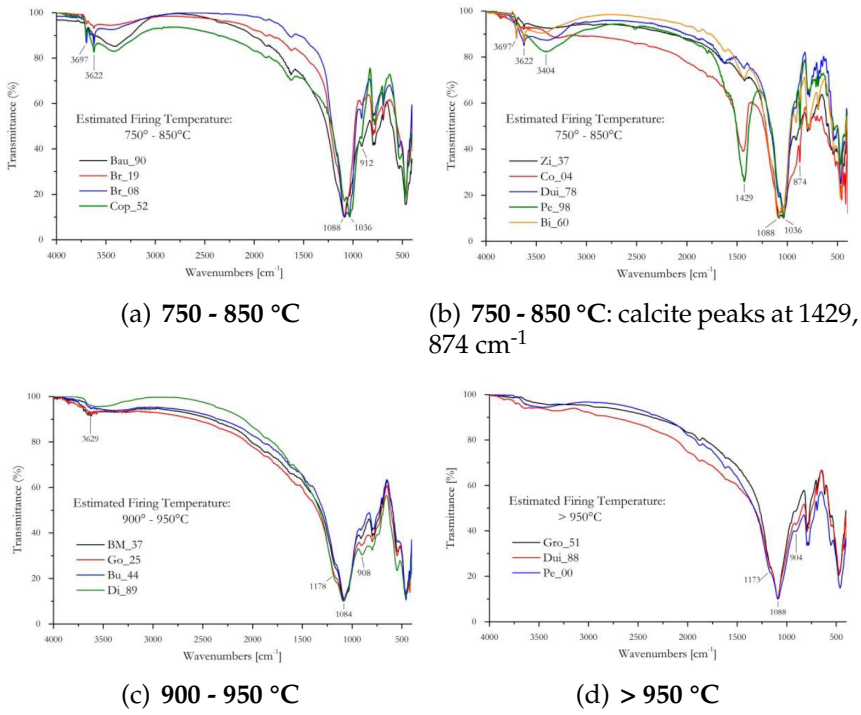

(a) **750 - 850 °C**

(b) **750 - 850 °C**: calcite peaks at 1429, 874 cm^{-1}

(c) **900 - 950 °C**

(d) **> 950 °C**

Figure 4.10: FT-IR spectra of representative Germans samples divided in the three sub-group, on the basis of the estimated firing temperature by means of FT-IR analysis. In the IR spectra even German samples not involved in the neutron analyses are reported.

in the ceramic matrix are the same which are listed in the section 4.1.1. In addition the **kaolinite** mineral was even identified in some FT-IR spectra through the two characteristic absorption peaks at 3697 and 3620 cm^{-1}, due to the stretching modes of the $-OH$ groups, (the other two of the four characteristic absorption peaks of the Kaolinite, i.e. 3670 and 3650 cm^{-1}, are not clearly visible in the IR spectra) [11]. FT-IR results allow to divide the ceramic shreds into three groups, based on the firing temperature which were related to their mineralogical composition. The FT-IR spectra are shown in figure 4.10 and the three groups are listed and summarised below.

1. **750 - 850 °C** group is formed by the following samples, which can be sub-grouped on the basis of their chemical and mineralogical composition (differentiating the presence of calcite or smectite minerals). The presence of the kaolinite detected only by means of the two characteristic peaks at 3697 and 3620 cm^{-1}, suggest that the mineral is in disordered state [6]. Furthermore the low intensity of these bands suggest that the dehydroxylation of kaolinite $Al_2Si_2O_5(OH)_4$ (to form

metakaolinite $Al_2Si_2O_7$, see section 3.4.2) is not completed. This transformation starts around 600 °C, but small amount of −OH can persist up to 750 - 800 °C. The presence of calcite are ascribed, where found, to the use of carbonatic raw materials and/or the reforamtion of secondary calcite during the burial period.
Samples as Dui_80, Bi_50, Bi_56 and Bi_60 are composed by Quartz, calcite, hematite, kaolinite and feldspar.
Samples as Br_09, Br_14, Br_19, Bau_89, Bau_91, Cop_51, Cop_57, Ka_12, Ka_22 and Ka_28 are composed by Quartz, feldspar, hematite, kaolinite, smectite (probably montmorillonite).

2. **900°-950°C** group is formed by Go_08, Bu_43, Bu_44, Bu_49, Bu_50 and Ka_20 which are composed by quartz, feldspar, hematite, kaolinite. In the FT-IR spectra, the presence of the characteristic peak of Kaolinite at 901-012 cm^{-1} due to the stretching of Al−OH and the absence of the two peaks of −OH stretching at 3690 and 3620 cm^{-1},indicate the firing temperature at around 900°-950°C.

3. **> 950 °C** group is composed by Gro_57, Gro_60, Dui_88 and Dui_90 which are composed mainly by quartz, hematite and kaolinite. The very weak intensity for the peak ascribed to the kaolinite at 912 cm^{-1} could indicate that its dehydroxylation and trasformation to metakaolinite is almost completed, followed by amorphization and destruction of alluminosilicate sheets [12].

µ-Raman

system provides punctual analyses of German ceramic shreds, collecting more than 10 points per sample. The experimental conditions for the analyses were the same involved for the Mediterranean samples (See section 4.1.1, paragraph about µ-Raman). The main detected mineralogical phases are the same which were detected for the Mediterranean samples (See section 4.1.1, paragraph about µ-Raman). In addition the German sample (Br_09) was possible to detect the rutile phase and the coexistence of anatase-rutile phase. The pure phase of rutile can be obtained only at firing temperature above 900 °C. It has to be taken into account that the temperature at which the transition from anatase to rutile occurs can be influenced by other minerals, in fact from FT-IR analysis this sample results fired at lower temperature [13]. The presence of hematite, magnetite and black carbon in some samples may suggest a variation of the atmospheric condition during firing process and/or a double step for this process. µ–Raman analyses have confirmed previous results obtained from FT-IR spectra regarding the estimated firing temperature of ceramics.

XRF

technique was involved in order to examine in depth the chemical composition of samples by means of a semi quantitative XRF analyses.

Table 4.4: Chemical composition of four representative German samples obtained from XRF analyses.

Oxides	Dui_90 [%]	Br_14 [%]	Br_49 [%]	Bu_43 [%]
SiO_2	57.25	45.38	46.86	44.64
Al_2O_3	16.07	25.48	18.46	22.64
TiO_2	5.24	7.44	5.11	4.15
Fe_2O_3	9.70	9.32	4.87	7.83
K_2O	3.79	5.95	17.75	11.95
CaO	3.43	3.40	3.40	7.92

The ceramic body of German samples are composed by the typical elements found in stoneware ceramic materials, which are **Si, Al, K, Ca, Ti, Fe** and of course **O**. These results are in agreement with the FT-IR and μ –Raman analyses previously reported. Chemical composition of four representative ceramic fragments is reported in table 4.4.

SEM-EDX

This kind of investigation was carried out to analyse the microstructure, morphology and chemical and mineralogical composition of the samples. SEM microphotographs of the ceramic bodies and glazes (when present) are shown in figure 4.11.

As can be seen, the bulk morphology of the analysed samples is quite different. Samples denominated as Br_ (which come from Brandis) show distinctive volumetric grains with irregular shape into the matrix, which appears not molten and characterised by layered and flat micrometric pores. Therefore these ceramic samples might have been fired at relatively low temperature. Furthermore, the surface present directional elongated-shape porosity, probably due to the forming technique adopted. Cop_57 (and similarly Cop_52 which is not shown in figure 4.11) shows different and arbitrary porosity, however the grains are not of regular shape and appear not completely fused in the clay matrix, suggesting not very high firing temperature [14]. Interesting are the results showed by sample from Duingen, the Dui_80. From a morphological point of view, it seems to be composed of fine grain particles, almost of homogenous distribution and with a random and low porosity. These features may suggest high firing temperature, but from FT-IR and μ-Raman analyses it results to be

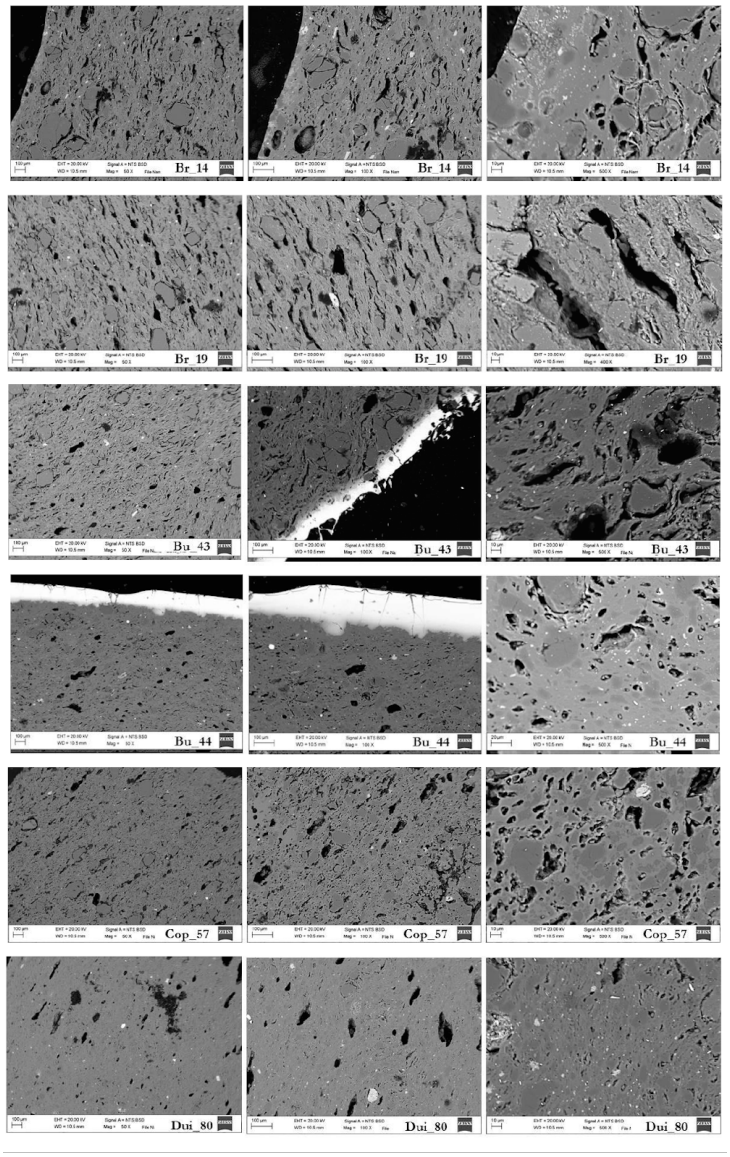

Figure 4.11: SEM images at magnification of 50x, 100x and 500x (from left to right) of six representative and selected German shreds.

fired at relatively low temperature, around 750 - 850°C. Probably, the fine grain particles can be molten easier and/or the micro grains cannot be well distinguished in the micro structure of the ceramic sample. Bürgel samples seem to be similar to Cop_57 (and Cop_52), but the borders of the grains are less pronounced, suggesting probably higher firing temperature. Elemental analyses for chemical elements of interest, as Al, Ca, Fe, K, Mg, Na, Si, Ti, S, were performed in order to provide insight on the mineralogical composition of the ceramic body with the joint of EDX punctual analyses. Chemical composition of four representative ceramic fragments is reported in table 4.5.

Table 4.5: SEM-EDX analyses of four selected German shreds.

Oxides	Cop_57 [%]	Bu_43 [%]	Br_14 [%]	Br_19 [%]
Si	73.93	47.92	49.56	46.59
Al	8.92	41.54	36.68	40.49
Ti	1.62	0.86	1.09	1.65
Fe	1.66	1.77	2.49	3.10
Na	0.09	0.24	0.00	0.16
Mg	1.25	0.22	0.30	1.08
K	1.21	4.21	4.48	1.80
Ca	0.38	0.54	1.20	1.34
Pb	0.00	0.47	0.00	0.17
S	6.32	0.52	0.38	0.46

From the semi-quantitative data provided by means of EDX analysis was possible to detect and recognise inclusions present in the clay matrix. Quartz grains, represent the main kind of inclusion and are present with different distribution size into all the analysed samples. Some samples (as Brandis Br_ ones) have shown greater size while thin particle size is observed in Dui_80 and Bürgel (Bu_) samples. Differences in particle size or angularity of quartz may provide insights able to help in distinguish quartz deliberately added by the potter and naturally present in the clay and so discriminates the different fabrics. Therefore the obtained results may suggest also different production technique in terms of raw materials selection. In general, as the quartz particles were detected in all the analysed samples, the firing temperature did not exceed 1000°C.

MIP

technique was involved to conduct porosimetry study about the ceramic matrix of German shreds. Porosity is a microstructural feature of ceramic materials which can be useful to provide information about the manufacturing process and the firing temperature [9] of historical potteries. However is necessary to underline that there is not a direct correlation between porosity and firing temperature. MIP is a destructive technique, therefore only significant samples were selected and analysed. Total open porosity of all the analysed potsherds ranges from around 2 to 27 % with a mean value of (12 ± 3) %, and the average pore radius ranges between 0.04 and 0.3 µm and the mean value is (0.11 ± 0.03) µm. In table 4.6 are reported the data obtained from MIP analysis for selected German ceramic shreds which were measured even with neutron scattering technique.

Table 4.6: Porosity data obtained by MIP measurements of selected German shreds.

Sample	Total cumulative pores volume [cm3/g]	Average pore radius [µm	Total porosity [%]	Bulk density [g/cm3]
Bu_43	0.09 ± 0.01	0.21 ± 0.01	12 ± 1	1.3 ± 0.2
Bu_44	0.03 ± 0.01	0.06 ± 0.01	7 ± 3	1.8 ± 0.2
Br_09	0.17 ± 0.01	0.05 ± 0.01	18 ± 2	1.1 ± 0.2
Br_14	0.07 ± 0.01	0.19 ± 0.02	12 ± 6	1.7 ± 0.5
Br_19	0.15 ± 0.01	0.07 ± 0.01	21 ± 2	1.6 ± 0.2
Cop_51	0.15 ± 0.01	0.08 ± 0.01	21 ± 2	1.4 ± 0.2
Cop_52	0.06 ± 0.01	0.06 ± 0.03	10 ± 7	1.9 ± 0.4
Cop_57	0.05 ± 0.01	0.08 ± 0.01	8 ± 3	1.6 ± 0.3
Dui_80	0.03 ± 0.01	0.04 ± 0.01	3 ± 1	0.97 ± 0.05
Dui_88	0.09 ± 0.01	0.29 ± 0.01	15 ± 4	1.6 ± 0.5

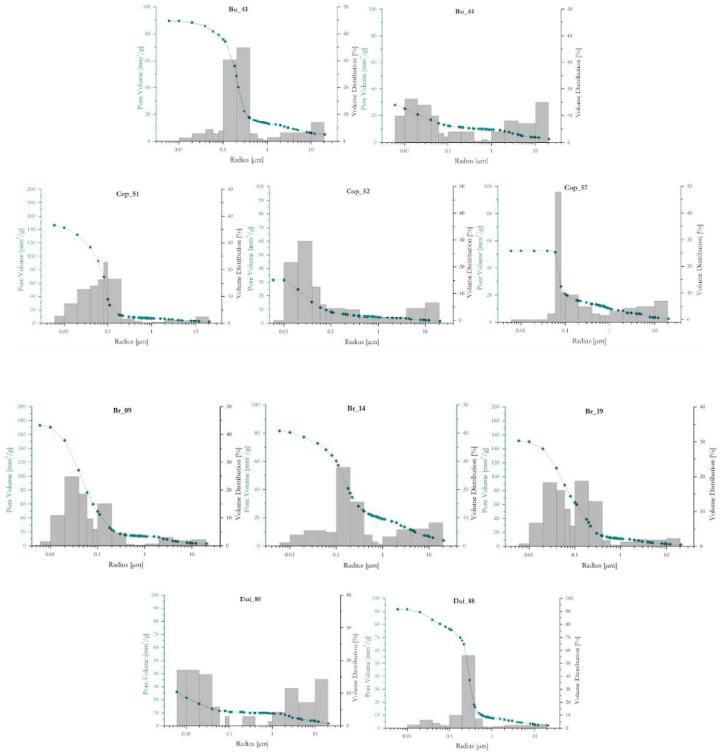

Figure 4.12: Cumulative pore volume and volume distribution versus pore radius of selected shreds from Germany.

In Figure 4.12 and figure 4.13 are reported the cumulative pore volume and volume distributions of open porosity for selected German shreds. Unimodal and polymodal curves may provide insights on the ceramic texture [15]. Bimodal and polymodal curves are observed in Brandis samples suggesting non homogeneous texture and two different population of pore dimension, while unimodal curves may indicate fine

and/or homogeneous texture. Porosimetry results of Dui_80 sample are in agreement with those obtained by means of SEM observations: the shred seems to be composed by fine grain particles which may produce a ceramic body with low porosity even if the estimated firing temperature does not exceed 850°C. Therefore the importance of the dimension and the composition of raw materials which influence the porosity of the ceramics matrix emerges. Ceramic shreds from Coppengrave (Cop_51, Cop_52 and Cop_57) exhibit very different pore distribution curve as well as total open porosity calculated by MIP. Cop_51 has greater open porosity than Cop_52 and Cop_57 potteries, which appear to be similar at SEM and FT-IR analyses (for SEM microphotograph of Cop_51 sample see [1]). Furthermore, although the chemical and mineralogical results affirmed similar composition for these ceramics from Coppengrave, differences in morphology and microstructure suggest a different production techniques probably referred to the raw material manufacturing processes.

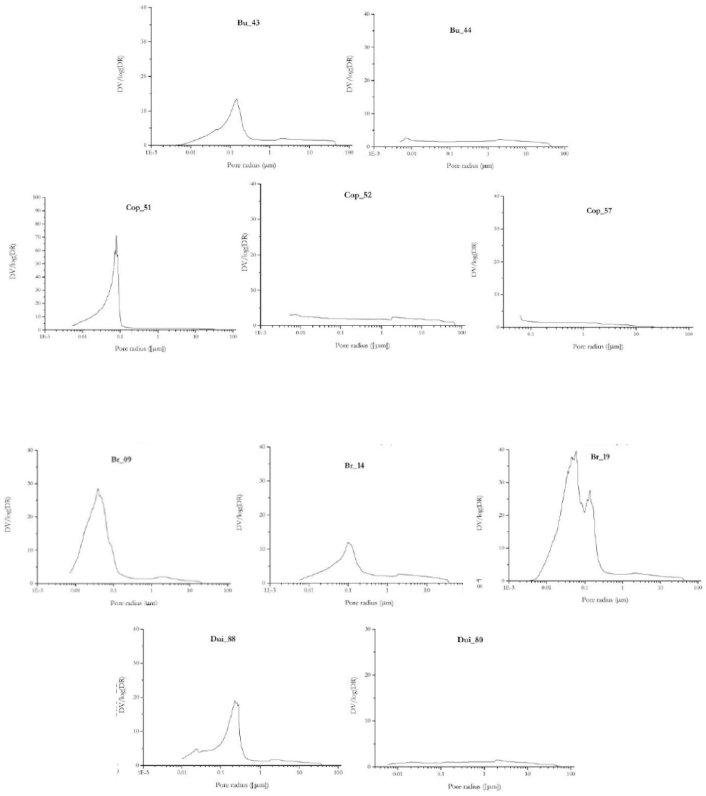

Figure 4.13: Pore size distribution curves versus pore radius of selected shreds from Germany.

Results obtained from ceramic materials made in laboratory showed how the differences in terms of grain size of the raw materials used can affect the microstructure although the composition and firing temperature are similar (these samples are not discussed in this thesis, for more detail see [1]). Brandis shreds (denoted as Br_) show a high open porosity in comparison with the other German shreds. Due to this fact

their estimated firing temperature result to be confirmed not only from FT-IR analyses but even from porosity analyses by means of MIP technique. Bu_43 and Bu_44 also showed a similar chemical composition but different morphology and MIP results allowed to quantify the diversity of these samples. Bu_44 shreds exhibits a low total open porosity of around 6% and Bu_43 around 11%.

Conclusions

The multi-analytical approach adopted in the Ricci's thesis to study the historical German shreds allowed to estimate the firing conditions and the raw materials used in the production techniques of the ceramic materials. Spectroscopic techniques such as FT-IR and μ-Raman, have provided the composition of the ceramic shreds from which information about the firing temperature have been extracted. The German shreds can be divided into 3 subgroups based on the range of the firing temperature, which are 750°-850°C, 900°C-950°C and above 950°C. Most of the German samples measured with SANS belong to the first subgroup which firing temperature is comparable to the Mediterranean ones.

Bibliography

[1] Giulia Ricci, PhD thesis, Ca'Foscari Venezia, **2016**, 203 pp.

[2] R. Ravisankar, S. Kiruba, A. Chandrasekaran, P. Jebakumar, *Indian Journal of Science and Technology* **2010**, *3*, DOI 10.17485/ijst/2010/v3i7/29813.

[3] S. Akyuz, T. Akyuz, S. Basaran, C. Bolcal, A. Gulec, *Vibrational Spectroscopy* **2008**, *48*, 276–280.

[4] N. Chukanov, *Infrared spectra of mineral species: Extended library*, Springer Netherlands, **2013**.

[5] J. Madejová, P. Komadel, *Clays and Clay Minerals* **2001**, *49*, _eprint: https://pubs.geoscienceworpdf/49/5/410/3270398/clmn-49-05-0410.pdf, 410–432.

[6] R. Ravisankar, S. Kiruba, P. Eswaran, G. Senthilkumar, A. Chandrasekaran, *E-Journal of Chemistry* **2010**, *7*, S185–S190.

[7] B. Fabbri, S. Gualtieri, S. Shoval, *Journal of the European Ceramic Society* **2014**, *34*, 1899–1911.

[8] G. Velraj, K. Janaki, A. M. Musthafa, R. Palanivel, *Applied Clay Science* **2009**, *43*, 303–307.

[9] G. Cultrone, E. Sebastián, K. Elert, M. de la Torre, O. Cazalla, C. Rodriguez–Navarro, *Journal of the European Ceramic Society* **2004**, *24*, 547–564.

[10] T. Majewski, D. Gaimster, *International Handbook of Historical Archaeology*, Springer New York, **2009**.

[11] A. Tironi, M. Trezza, E. Irassar, A. Scian, *Procedia Materials Science* **2012**, *1*, 343–350.

[12] A. Lavat, M. Grasselli, J. Tasca, *Ceramics International* **2007**, *33*, 1111–1117.

[13] D. de Waal, *Journal of Raman Spectroscopy* **2004**, *35*, _eprint: https://onlinelibrary.wiley.com/doi646–649.

[14] A. Krapukaityt, S. Tautkus, A. Kareiva, *Lithuanian Journal of Physics* **2006**, *46*, 383–388.

[15] C. Volzone, N. Zagorodny, *Applied Clay Science* **2014**, *s 91–92*, 12–15.

Chapter 5

SANS Measurements and Data Reduction

The main work for this thesis consisted in the data reduction and analysis of a huge amount of SANS data collected on the SANS instrument D11at the Institut Laue - Langevin in Grenoble. The collected data were reduced with the Large Array Manipulating Program (LAMP) [1], which is a program for the neutron scattering data reduction developed at ILL. The reduced data were analysed by means of two main computer programs. For the data manipulation I have used Origin software. The $I(Q)$ curves obtained by the data reduction contains a lot of information of the systems like form factor, structure factor, voids, fractal exponent, details on the interfaces nature of separated phases an so on. The curves has been fitted to obtained by using SasView program, that is a Small Angle Scattering Analysis Software Package, managed by an international collaborations of worldwide Large-Scale facilities such as the ILL [2], containing a rich library of models.

5.1 Experimental Method

5.1.1 Measurement Setting

In this section the instrumental settings used to collect the SANS raw data from the ceramic shreds are reported. Samples have been analysed at 3 different neutron wavelength, that are 4,6 Å, 6 Å and 13 Å, in order to obtain the widest Q range available on D11. For both 4.6 and 6 Å neutrons wavelengths, 3 sample to detector distances (SDD) were: 1, 8 and 39 m. The data have been collected for 6, 4 and 2:30 minutes respectively for 39, 8 and 1 m. After the collection and the reduction of the data (see

section 5.2), the scattering curves obtained from the distances were merged in order to obtain a continuous data set, indicated as "merged curve", in the follow sections (for the merging procedures see section 5.2). For the 6 Å these 3 distances allow to cover the Q range from $1.6x10^{-3}$ $Å_{-1}$ to $4.2x10^{-1}$ $Å_{-1}$. For the 4.6 Å wavelength, these instrumental settings allow to explore the Q range from $2.5x10^{-3}$ to $5.8x10^{-1}$ $Å_{-1}$. In addition a wavelength of 13 Å has been used to explore a very low Q region, obtaining information about the scattering of larger objects and larger correlation distances (600 nm). These measurements were performed for a sample-to-detector distance of 39 m for 15 minutes. This additional instrumental setting allows to enlarge the Q range up to $6x10^{-4}$ $Å^{-1}$.
The transmission of the sample was obtained at a SDD of 8m.
The calibration procedure was done by means of a H_2O measurement to determine the absolute scale and the detector efficiency [3].
The ceramic shreds were loaded on a multiple samples holder of 22 slots with a window of 6x10mm. The sample holder was mounted on movable rail allowing a remote program to select the samples.

5.1.2 Experimental Procedures

In this section the experimental procedures used to obtain and analyse the SANS data are reported.

Pre-measurement operations

In this thesis I analysed historical ceramic samples obtained from archaeological excavation sites (In Germany and in Torcello, Italy, see chapter 4) by means of SANS techniques. The historical samples were recovered in the form of pieces of different type of ceramic objects that originally were amphorae or other ceramic objects used as a food containers, for example objects employed in the trade of goods or in the common day life of people as plates or vessel. To avoid the multiple scattering during the measures, thin slices of the ceramic shreds were cut from the original samples. The preparation of the samples is crucial and 3 steps were necessary for that:

1. The first step consisted in the removal (if is present, and this is particularly true for German samples) of the glaze on the ceramic external surface. This glaze contains a large number of metals, especially the heavy ones like Fe, Pb, Cu and Co which have a high value of the absorption cross section and a high degree of Radioactive activation [4]. For these reasons they complicate the measurement reducing the transmission of neutrons and activating the samples.

2. The second step consist in the extraction of a slice of ceramic matrix from the historical shreds. This was achieved using a diamond wire saw, cutting a thin longitudinal cross section from the ceramic matrix. Due to the fragility of the historical ceramic objects, this step required a high level of expertise in the use of the cutting tools and very long time.

3. The third step of the preparation of the ceramic samples concern the reduction of the thickness of the sliced ceramic samples with a fine-grained sand paper.

Samples have been measured in different environments and different instrumental configurations. In the paragraphs below the various experimental methods were reported. They are briefly summarised here:

- Samples measured at 6Å for 3 SDD;
- Samples measured at 4.6Å for 1 SDD;
- Selected samples measured at 4.6Å for 3 SDD;
- "Dry" samples measured at 6Å;
- "Wet" samples measured at 6Å, immersed in D_2O.

SANS Measurements with Different Wavelength

Samples measured at 6Å for 3 SDD. The first SANS measurements have involved ceramic shreds of 1 mm average thickness, with a neutron wavelength of 6 Å. Each sample has been measured at the 3 sample to detector distances mentioned above (see section 5.1.1). In addition to extend the Q range, samples were measured at 13 Å for a SDD of 39 m.
After the data reduction, the 3 SDD merged curve obtained at 6Å and the 1 SDD curve obtained at 13 Å were plotted together for each sample. From these plots is possible to notice that in the intersection zone the trend of the two curves is not the same. This discrepancy, is due to the undetermined effect of multiple scattering, which occurs when a scattered neutron is scattered twice or more times in the sample (see section 5.2.3). In the figure 5.1 are shown 3 examples of 6 Å and 13 Å SANS curves in which are present the multiple scattering effect. This effect smear the true intensity coming from the scattering of the samples, complicating and falsifying (if its contribution is high enough) the data interpretation. For this reason, the samples has been reduced in thickness and measured again, as reported in the following section.

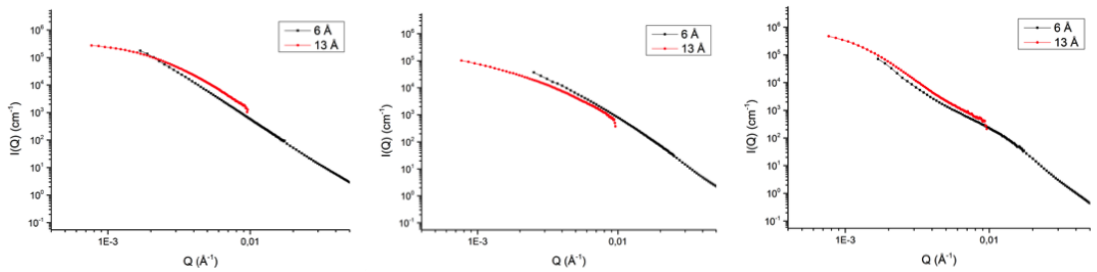

(a) (b) (c)

Figure 5.1: Example of multiple scattering in three samples form bot German and Mediterranean groups.

A picture of samples measured in the condition of thickness and wavelength reported above, and mounted on the samples holder is reported in figure 5.2.

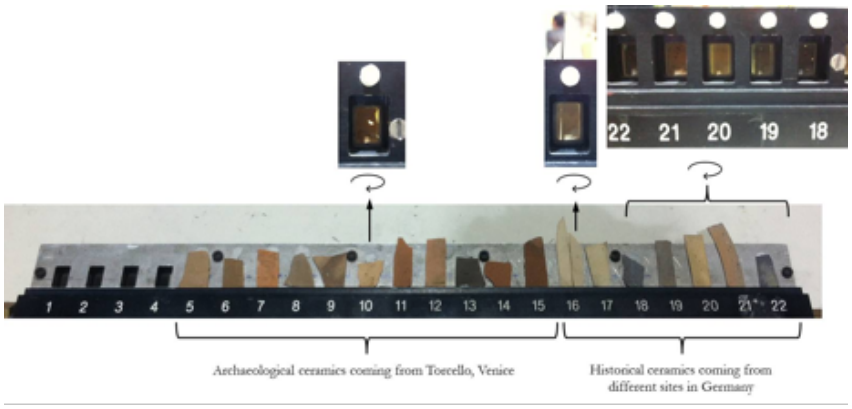

Figure 5.2: Picture of the samples holder loaded with samples measured at 6 Å for 3 SDD.

In table 5.1 the samples measured at 6 Å for 3 SDD are listed. In these samples name, the suffix "G" have been added to specify their average thickness of 1 mm. The first 4 slots were used for the calibration measurements, which are reported later.

Samples measured at 4.6 Å at 1 SDD. In order to reduce the probability of multiple scattering and increase the transmission values, the samples measured at 6 Å for 3 SDD reported above, have been measured at 1 SDD of 39 m with a neutron flux of wavelength of 4.6 Å. That is because the probability the multiple scattering is more probable when wavelength increases. Comparing the curves obtained from measurements done at 4.6 and 6 Å and showed in figure 5.3, no differences emerge between the trend of these curves especially in the low Q region. These results indicate that there are no essential differences between the samples measured at 4.6 or 6 Å, and than is possible to conclude that the 6 Å measurements are not affected by a relevant multiple scattering. On the contrary it affects considerably the measurements done

N°	Sample	Thickness [mm]
5	1154_10	1.23 ± 0.05
6	1154_8	1.31 ± 0.02
7	5155_23	1.00 ± 0.04
8	1210_1	1.03 ± 0.09
9	1224_2	1.31 ± 0.06
10	1159_2	1.01 ± 0.05
11	1188_4	0.90 ± 0.07
12	5157	1.0 ± 0.1
13	1151_5	1.17 ± 0.05
14	1155_1	1.1 ± 0.1
15	1167_1	1.2 ± 0.1
16	Bu_49	1.11 ± 0.06
17	Bu_50	0.9 ± 0.2
18	Bi_50	0.8 ± 0.1
19	Ka_20	0.82 ± 0.04
20	Dui_88	0.96 ± 0.01
21	Dui_90	1.13 ± 0.04
22	Br_14	0.73 ± 0.02

Table 5.1: List of Samples loaded in the sample holder shown in figure 5.2 and measured at 6 Å for 3 SDD.

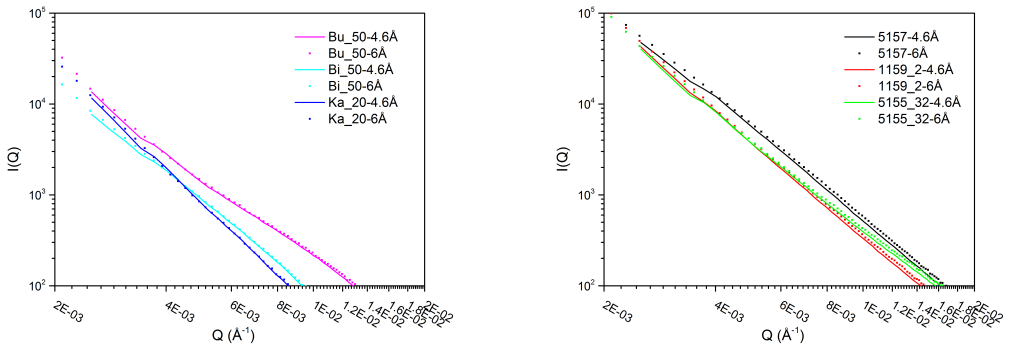

(a) (b)

Figure 5.3: Comparison between data obtained at 4.6 Å (represented with lines) and 6 Å (represented with scatters) for: (a) German samples, (b) Mediterranean samples. Three representative curves for each historical group are shown.

at 13 Å, as shown in figure 5.1. Due to the fact that a larger number of samples have been measured at 6 Å than 4.6 Å, and these two measurements have the same multiple scattering contributions, the data analyses (which are reported later on the chapter 6)

have been performed on samples measured at 6 Å, giving a more extended Q region toward the low angle part.

Samples measured at 4.6 Å for 3 SDD. During the same experiment, 11 samples selected from the first run of measurements done at 6 Å and reported in table 5.1, were reduced in thickness from 1mm up to averagely 0.5 mm and measured at 4.6 Å for 3 SDD. The reduction of the thickness has been done in order to reduce more and more,

N°	Sample	Thickness [mm]
7	1210_1	0.54 ± 0.03
8	1151_5	0.50 ± 0.02
9	1155_1	0.555 ± 0.007
10	1154_8	0.43 ± 0.04
11	Dui_88	0.49 ± 0.01
12	Br_09	0.43 ± 0.04
13	Br_14	0.465 ± 0.007
14	Br_19	0.46 ± 0.02
15	Bu_43	0.47 ± 0.04
16	Cop_57	0.565 ± 0.007
17	Cop_51	0.50 ± 0.02

Table 5.2: List of Samples measured at 4.6 Å for 3 SDD.

the probability of multiple scattering and to attempt to obtain data in the very low Q region available on D11. These selected samples are reported on table 5.2.

SANS Measurements in Different Environments

SANS measurements conducted in different environments, which can be for example a specific solvent or a mixture of solvents rather than air, can be a precious way to obtain more detailed information about the systems under study. The different cross section of hydrogen and deuterium is used to implement a so called "Contrast method" [5]. This allow to distinguish solvent from systems and to enance the scattering from different part of the sample. Furthermore the use of heavy water allow to reduce the background due to the incoherent present in the H_2O. In this work of thesis, the contrast method has been involved in the study of open and closed pores (see section 6.4). In the following paragraphs the experimental conditions for the two measurements conducted in the two different environment are reported, that are:

- measurements conducted in air environment (samples named with the suffix "Dry");

- measurements conducted in liquid environment, which is constituted by a mixture of H_2O/D_2O.

"Dry" samples measured at 6Å. The samples reported in the previous paragraphs, were measured in air environment and can be identified with the suffix "Dry" if it is necessary for the better comprehension. This environmental condition was achieved exposing the samples directly in air at atmospheric pressure, temperature and humidity. The samples were not dry in the strict sense but the word Dry is to distinguish them from the samples prepared by immersion in heavy water. These measurement were performed as reported in previous paragraphs (see figure 5.2).

"Wet" samples measured at 4.6Å and 6Å. In these experiments samples were measured in both "Dry" and "wet" conditions. Dry samples were measured in air and loaded in quartz Hellma cells of 1 or 2 mm depending on the thickness of the sample itself. After the measurement in air of the dry samples (at two wavelength already cited), the cells were filled with a mixture of H_2O/D_2O based on the calculated scattering length density (for better detail of the Contrast Methods and the scattering length density calculation, see section 6.4), in order to apply the contrast method and to distinguish closed and open pores. The samples were soaked 24h before performing the measurements, to allow a good penetration in the open pores. A picture of the samples measured in the "Wet" conditions is reported in figure 5.4.

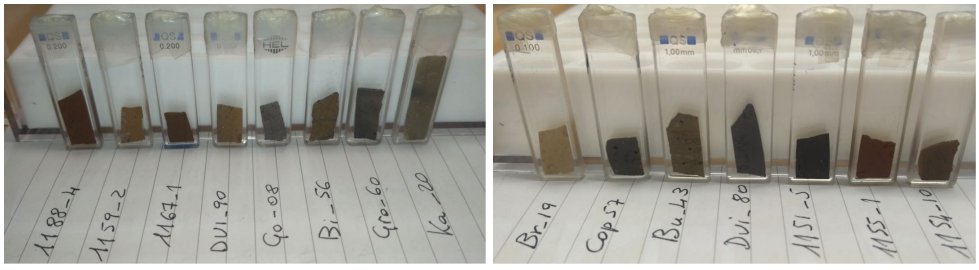

(a) (b)

Figure 5.4: Two photos of some samples loaded in the cuvettes and filled with the mixture of H_2O/D_2O, for the measurements in "Wet" condition. (a) Samples of 1 mm average thickness in 2 mm cuvettes, (b) samples of 0.5 mm average thickness in 1 mm cuvettes.

5.2 Data Reduction

The data reduction is the first step that has to be done before treating the data in the way to extract information from them. It is a procedure that consist of a series of operations performed by specific software which aim is to obtain, at the end, the scattering intensity $I(Q)$ in absolute scale, i.e. in cm^{-1} The different steps of the data reduction consist of [6, 7]:

- the calculation of the **beam centre**, for the different configurations used, necessary to determine the neutron's scattering angle;
- the creations of the **mask files**, which virtually reproduce on the 2D detector image, the physical beam-stop, placed in front of the detector to block and reduce the high intense primary beam;
- the measurement of the **empty cell** (for soft matter samples), that is subtracted from the measured intensity;
- the calculation of the transmission;
- the radial averaging, giving the intensity as a function of Q for isotropic scattering, for the anisotropic ones the average is performed by sectors along the directions of anisotropy;
- the obtainment of the absolute intensity.

The obtainment of an absolute intensity can be performed after the integration of the scattered image printed on the detector. When a coherent beam with a flux ϕ_o illuminate a sample of volume V and a thickness e, during a time t, a given fraction of the incident flux ΔN is elastically scattered in the direction Q within a solid angle $\Delta\Omega$:

$$\Delta N(Q) = \phi_0 t Tr \frac{d\sigma}{d\Omega}(Q)\Delta\Omega \tag{5.1}$$

where Tr is the transmission coefficient of the neutrons flux through the sample and σ is the scattering cross section. $\frac{d\sigma}{d\Omega}(Q)$ is the differential scattering cross section characteristic of elastic interaction between sample and neutrons. It correspond to the number of neutrons scattered per second within the solid angles $\Delta\Omega$. Then the intensity $I(Q)$ scattered per unit volume is:

$$I(Q)[cm^{-1}] = \frac{1}{V}\frac{d\sigma}{d\Omega}(Q) = \frac{\Delta N(Q)}{\phi_0 t Tr \Delta\Omega e} \tag{5.2}$$

From the 5.2 is possible to define the differential of the macroscopic scattering cross section $\Sigma = \frac{N}{V}\sigma$ as a function of the intensity $I(Q)$:

$$(\frac{d\Sigma}{d\Omega})_{Total} = \frac{1}{\phi_0 t Tr \Delta\Sigma(Q) e(Q)} I(Q) \tag{5.3}$$

In a SANS measurement, especially in soft condensed matter, the sample are generally filled in a quartz cell that contributes to the neutron scattering, affecting the total $I_tot(Q)$. The scattering contribution from the empty cell $I_EC(Q)$ is subtracted from the total scattering:

$$(\frac{d\Sigma}{d\Omega})_{sample} = (\frac{d\Sigma}{d\Omega})_{\text{total}} - (\frac{d\Sigma}{d\Omega})_{\text{EC}} \tag{5.4}$$

The transmission is calculated with respect to the empty beam.

5.2.1 Normalisation With Standard Sample

The normalisation procedure to obtain an absolute scaling for the $I(Q)$, and even to correction the variation in efficiency of cells, is done by a standard sample such as light water (H_2O) or vanadium (V). These samples are chosen for their quasi total incoherent scattering. The incoherent scattering can be imagined as the scattering coming from the correlation of one nucleus with itself individually [8]. For the SANS measurements the common calibration sample is the light water for its availability and its strong incoherent scattering intensity. Due to the fact that for the H_2O, the scattered neutrons are not uniform in 4π, a wavelength-dependent correction factor has to be introduced to write the real scattering cross section. The differential of the macroscopic scattering cross section normalised with the H_2O can be written as:

$$(\frac{d\Sigma}{d\Omega})_{sample} = \frac{I_{sample}}{I_{\text{H}_2\text{O}}} (\frac{d\Sigma}{d\Omega})^{real}_{\text{H}_2\text{O}} \tag{5.5}$$

The calibration is measured only for low distance sample-detector, because high distance measure would take long time to obtain a reasonable signal. Water scattering measure on different instrument could be very different. Due to the multiple scattering and inelastic effect, scattering measure depends deeply on the neutrons wavelength and on the geometry of the instrument. For these reasons, a universal calibration curves does not exist in SANS measurements.

5.2.2 Transmission

The transmission is the ratio of the intensity of neutrons flux at $Q = 0$ between the beam through the sample ($I_s(2\theta)$) and the white beam (I_0). It depends on the sum of coherent, incoherent and absorption cross-section and also from the scattering angle.

$$Tr(2\Theta, \lambda) = \frac{I_s(2\theta)}{I_0} = e^{-(\mu(\lambda)e(2\Theta))} \tag{5.6}$$

$$where \quad \mu(\lambda) = N\sigma(\lambda) = \frac{1}{\Lambda(\lambda)} \tag{5.7}$$

The $\mu(\lambda)$ is the mass adsorption coefficient dependent on wavelength and $\Lambda(\lambda)$ is the mean free path of the radiation in the sample. The $\sigma(\lambda)$ is the scattering cross section that could be calculated from the transmission measured at $\theta = 0$, and is the sum of three terms:

$$\sigma(\lambda) = \sum_i \sigma_{coh,i} + \sigma_{incoh,i} + \sigma_{abs,i}(\lambda) \tag{5.8}$$

where the index i is referred to the different atoms and isotopes. The $\sigma_{abs,i}(\lambda)$ is the absorption cross-section due to nuclear capture process. It is inversely proportional to the wave vector $k = \frac{2\pi}{\lambda}$ and thus proportional to λ. For these reason the absorption of a neutron is higher for a neutron flux of 13 Å than 6 or 4.6 Å. For a neutron wavelength λ used in a neutron scattering experiment, $\sigma_{abs}(\lambda) = \frac{\sigma_{abs}(\lambda)\lambda}{1.8}$.

	Atomic Number	b_{coh} (10^{-12} cm)	σ_{coh} (10^{-24} cm^2)	σ_{inc} (10^{-24} cm^2)	$r_e f(s)$ (10^{-12} cm)	
					$s = 0$	$s = 1$ Å^{-1}
^{1}H	1	−0.374	1.76	79.9	0.28	0.02
^{2}D	1	0.667	5.59	2.04	0.28	0.02
C	6	0.665	5.55	0.001	1.69	0.48
N	7	0.936	11.01	0.49	1.97	0.53
O	8	0.580	4.23	0.000	2.25	0.62
^{19}F	9	0.565	4.02	0.001	2.53	0.75
^{23}Na	11	0.363	1.66	1.62	3.09	1.14
Si	14	0.415	2.16	0.015	3.95	1.72
^{31}P	15	0.513	3.31	0.006	4.23	1.83
S	16	0.285	1.02	0.007	4.5	1.9
Cl	17	0.958	11.53	5.2	4.8	2.0
K	19	0.371	1.73	0.25	5.3	2.2
V	23	−0.0382	0.018	5.19	6.5	2.8
Ni	28	1.03	13.3	5.2	7.9	3.6
Br	35	0.680	5.80	0.10	9.8	4.7

Figure 5.5: Scattering length and cross section for some common elements and isotopes [9].

In Figure 5.5 [9] are listed the values of the absorption cross section for some nuclei and isotopes, registered for a neutron wavelength of 1.8Å (i.e. neutron velocity of 2200

Element	Atomic Number	Absorption Cross-Section σ_{abs} (10^{-24} cm^2)		Mass Absorption Coefficient $\mu/\bar{\rho}$ (cm^2/g)	
		x-Ray	Neutron	x-Ray	Neutron
H	1	0.655	0.3326	0.391	0.199
D	1		0.00051		0.00015
Li	3	5.76	70.5	0.500	6.12
Be	4	16.6	0.0076	1.11	0.00051
B	5	41.5	767	2.31	42.7
C	6	89.9	0.0035	4.51	0.00018
N	7	173	1.90	7.44	0.0817
O	8	304	0.00019	11.5	7.2×10^{-6}
F	9	498	0.0096	15.8	0.000304
Na	11	1140	0.530	29.7	0.0139
Al	13	2220	0.231	49.6	0.00516
Si	14	2970	0.171	63.7	0.00367
P	15	3880	0.172	75.5	0.00335
S	16	4970	0.53	93.3	0.0100
Cl	17	6240	33.5	106	0.569
K	19	9400	2.1	145	0.0324
Fe	26	28000	2.56	302	0.0276
Ni	28	4760	4.49	48.8	0.0461
Cu	29	5470	3.78	51.8	0.0358
Cd	48	41500	2520	222	13.50
Gd	64	105000	48890	403	187.2
Pb	82	79800	0.171	235	0.00050

[a] The absorption values for x-rays are for the Cu$K\alpha$ radiation ($\lambda = 1.542$ Å), and those for neutrons are for $\lambda = 1.8$ Å. The neutron data are from Bée[8] and are for the elements with the natural abundance of isotopes, except for H and D. The x-ray data are from the *International Tables of Crystallography*.[9]

Figure 5.6: Absorption Coefficients for x-rays and neutron. The absorption values for x-rays are for the Cu$k\alpha$ radiation (λ=1.542 Å) [10], and those for neutron are for λ=1.8 Å [11].

m/s). Typical values range from 0.1 to 10 barns (10_{-24} cm^2) but can be very high for certain atoms like Boron (3835 barns), Cadmium (2520 barns) and Gadolinium (49700 barns). In figure 5.6 are reported the values for the absorption cross-section and mass absorption coefficient for both neutron and x-rays. The numbers there show clearly that neutrons are generally far more penetrating than x-rays through matter [12].

5.2.3 Multiple Scattering

Multiple scattering is a phenomenon which occurs when a scattered neutron is scattered again in the sample. In figure 5.7 is schematically depicted the multiple scattering phenomenon. There is always a probability that such event occurs but it must not dominate the total scattering intensity. Multiple scattering smears the true intensity since the total intensity is the sum of intensities due to the single, twice or more scattering vectors at unknown angles.
There is no general method to correct data from multiple scattering but there are some evidences that could indicate if the multiple scattering contribution is considerable, for example a low transmission coefficient (<0.5). In case of "weak" multiple scattering different methods are proposed to correct the scattering intensity [13, 14]. Different

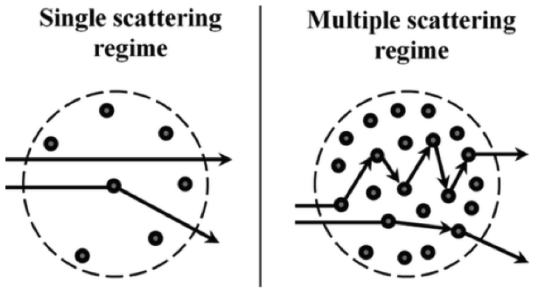

Figure 5.7: Illustration of the single scattering (left) and multiple scattering (right) events.

scattering distortion are observed in case of low multiple scattering. First evidence is that curves measured at different configuration (i.e. wavelength or distance between sample and detector) do not overlap even after the merging operation (see in figure 5.1, the multiple scattering evidence for the curves obtained at 13 Å). Another example of multiple scattering effect is shown in figure 5.8, in which three different curves for a dispersion of carbon black particles contained in a matrix of styrene-butadiene rubber are reported, for three different sample thickness. It's possible to notice that reducing the thickness and wavelength of neutrons, different features are observed and the tendency to a plateau at lower values of Q is lost. This is due to the reduction of the multiple scattering events [15]. To reduce multiple scattering effects is possible to:

- use thinner and diluted samples;
- use shorter wavelength to increase the mean free path $\Lambda(\lambda)$;
- decrease the contrast $\Delta\rho$ between the phases.

5.2.4 Averaging and Merging Operations

The further step concern the radial (or sector) averaging along the 2D monitor, in order to obtain the intensity ($I(Q)$) vs the scattering vector (Q) data. In figure 5.9 the 2D detector images obtained for isotropic and anisotropic samples are shown. In the anisotropic ones (figure (b)), the sectors directed along the two axis of anisotropy, through which the radial integration is performed, are shown.
In SANS experiments changing the instrument configuration, as wavelength and sample-detector distance, permit to optimise the efficiency of the measure, acting on the measurable Q range. A common procedure to obtain the largest Q range possible, without changing the wavelength (that is a procedure requiring a lot of beam time) is to set a

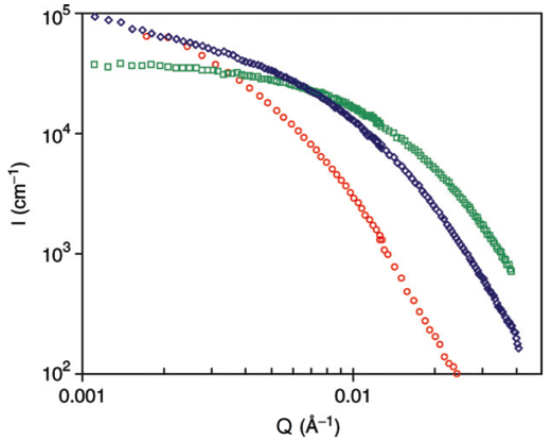

Figure 5.8: Evidence of multiple scattering on a sample made of carbon black particles dispersed in an elastomer matrix. Green square correspond to a sample thickness e=1.3 mm, λ=20 Å, blue diamond e=0.63 mm, λ=20 Å and red circle e=1 µm, λ=5 Å.

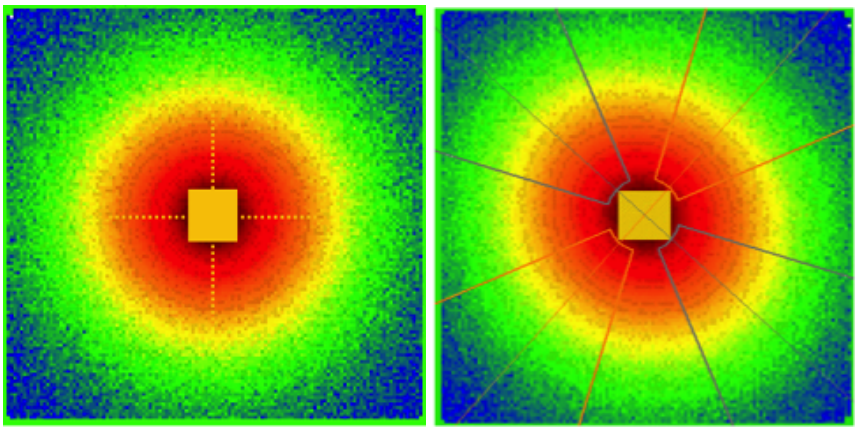

(a) (b)

Figure 5.9: 2D images of the detector for (a) isotropic sample, (b) anisotropic sample. In the anisotropic image is possible to notice the two different sectors along the two directions of the anisotropy. Yellow and orange rectangles in the centre of the two images are the mask files created to virtually reproduce the beam stop on the detector image.

determined wavelength and measure the sample at different distance from the detector (sample to detector distances). After that the $I(Q)$ data obtained for each distance have to be merged, to produce a continuous set of data that cover the wider Q range possible, by a re-scaling procedure. This is done by the LAMP program [1], with the same procedure for each sample, in a consistent way to reduce the error arising from the different resolutions for the 3 curves, due to the different sample to detector distance. In the procedure, the middle Q is used as references and the other two curves at low Q and high Q are re-scaled on the reference by a multiplicative factor for each ones. In this work of thesis the curves at low Q and high Q are the ones obtained for

a SDD of 1 and 39 m respectively. The reduced data are then exported in a common ASCII file, composed of 4 column, which are: Q[Å^{-1}], $I(Q)$[cm^{-1}], the errors of the intensity $\Delta I(Q)$[cm^{-1}] and the errors of scattering vector ΔQ[Å^{-1}].

5.2.5 Background Subtraction

The incoherent scattering, mainly coming from the hydrogen molecules, gives rise to a flat background that is necessary to subtract before the data analysis. It is a delicate operation, because a wrong estimation of the incoherent value could alter the data interpretation and the results obtained from the data analysis. A number of different methods are employed to correct the incoherent background.

- Estimation of the incoherent background through the measurement of $I(Q)$ at the highest possible scattering vector Q (>0.4 Å), because in most of the cases in condensed matter, objects are big enough to neglect coherent scattering at high Q

- Subtraction of the scattering from the solvent in case of very diluted and deuterated compound within a hydrogenated solvent.

- Measuring of a reference sample with no structure that contains the same amount of H and D atoms of the sample (for example, a mixture of H_2O/D_2O). This requires to know exactly the sample composition to prepare a mixture having the same transmission as the sample.

- If the scattering cross section has a Q dependence, is possible to write that $I(Q) \propto AQ^{-d} + B$, where B represent the background. At high Q, one can suppose that the Porod regime is reached, so $d = 4$ and then $I(Q)Q^4 \propto A + BQ^4$. The slope gives the value of the incoherent background.

- The incoherent background can be evaluated in principle with the tabulated values of the bound incoherent scattering length b_{inc} (which is smaller than the real ones in the case of free atoms), with which is possible to calculate the scattering length density SLD

$$SLD = \frac{\rho N_\alpha \sum_i b_{i,inc}}{\sum_i c_i M_i} \tag{5.9}$$

  where ρ is the bulk density of material, N_a is the Avogadro's number, M_i is the molecular weight of the atom i and c_i is a weighting number (which are the stoichiometric numbers in a chemical formula). In the formula the incoherent contribution coming from the spin is not taken into account.

5.2.6 Data Files

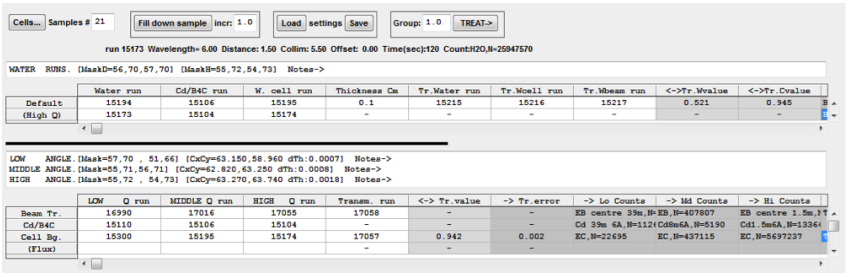

Figure 5.10: The capture of the part of the LAMP screen in which are present the calibrations.

In the previous paragraphs are reported all the common calibrations involved in a SANS measurement to finally achieve the data reduction and so the absolute scattering intensity $I(Q)$[cm^{-1}]. In order to obtain the four column reduced data, all of these calibration data files have to be uploaded in the working path of the LAMP Program. In figure 5.10, is reported an image of how a common interface of LAMP for a SANS data treatment appears. In the cells are reported the number referred to the measurement related to a specific calibration, for example the numor "15173" is referred to the measurement of the H_2O at high Q.

Bibliography

[1] D. Richard, M. Ferrand, G. J. Kearley, *Journal of Neutron Research* **1996**, *4*, 33–39.

[2] ILL web site, Library Catalog: www.ill.eu, `https://www.ill.eu/`.

[3] Peter Lindner, Ralf Schweins, *Neutron News* **2010**, *21*, 15–18.

[4] *Neutron data booklet*, 2nd ed, (Eds.: A. J. Dianoux, G. H. Lander, I. Laue-Langevin), Old City, Philadelphia, PA, **2003**, 1 p.

[5] O. Glatter, O. Kratky, *Small angle x-ray scattering*. _eprint: https://onlinelibrary.wiley.com/doi/ London: Academic Press, **1982**, 296 pp.

[6] I. Grillo in *Soft Matter Characterization*, (Eds.: R. Borsali, R. Pecora), Springer Netherlands, Dordrecht, **2008**, pp. 723–782.

[7] R. E. Ghosh, S. U. Egelhaaf, A. R. Rennie, *ILL report 06GH05T* **1989**, 156.

[8] G. L. Squires, *Introduction to the Theory of Thermal Neutron Scattering*, 3rd ed., Cambridge University Press, Cambridge, **2012**.

[9] V. F. Sears, *Neutron News* **1992**, *3*, 26–37.

[10] M. Bee, Quasielastic neutron scattering. Principles and applications in solid state chemistry, biology and materials science, (Ed.: A. Hilger), **1988**.

[11] A. J. C. Wilson, V. Geist, *Crystal Research and Technology* **1993**, *28*, _eprint: https://onlinelibrary.v 110–110.

[12] R. Roe, *Methods of X-ray and Neutron Scattering in Polymer Science*, Oxford University Press, **2000**.

[13] J. Lal, J. M. Widmaier, J. Bastide, F. Boue, *Macromolecules* **1994**, *27*, 6443–6451.

[14] J. Schelten, W. Schmatz, *Journal of Applied Crystallography* **1980**, *13*, 385–390.

[15] I. Morfin, F. Ehrburger-Dolle, I. Grillo, F. Livet, F. Bley, *Journal of Synchrotron Radiation* **2006**, *13*, 445–452.

Chapter 6

Data Treatment

In this chapter all the different methods employed to analyse the SANS data are reported. The data obtained after the reduction have been organised in 2 different groups, related to the 2 sample's origins: the Mediterranean group (in which samples were recovered in Torcello, Italy) and the German group (containing samples recovered in the regions of Sachsen and Türingen).

6.1 Isotropic and Anisotropic Behaviour

In the nanometric scale of SANS investigation, isotropic and anisotropic data have been obtained from samples. This behaviour is reflected in the images registered on the detector screen. An isotropic sample gives back an image that is uniform along all the directions, "painting" through the diffused neutrons a series of circular ring on the detector screen. Anisotropic samples give back images that are characterised by two or more preferential direction for the scattered neutrons. Two examples of the 2D detector screen are reported in figure 5.9 (see chapter 5, section 5.2). A first preliminary and qualitative analysis based on the isotropic or anisotropic behaviour of the samples has been employed. The obtained results, listed in table 6.1, can give an evaluation of the fraction of the isotropic and anisotropic samples, in the two groups.

Table 6.1: Isotropic and anisotropic behaviour of the 2 groups of samples.

	Total samples [%]	Isotropic samples [%]	Anisotropic samples [%]
German	28	71	29
Mediterranean	11	45	55

Table 6.1 shows that the Mediterranean group has a major percentage of anisotropic

samples compared with the other two groups. This behaviours could be related to different factors: the preferential orientation of pores, the low homogeneity of the ceramic matrix, the different size of grains and the different manufacturing process in the production of the potteries. For example the use of wheel thorowing [1] compared to the slipcasting [2] could have a different effect on the orientation of particles and pores inside the matrix [3]. It is also true that due to the high level of complexity of the ceramic systems, is not easy to correlate the anisotropic behaviour of the ceramic matrix with the factors listed above. From these first preliminary results, it is possible to notice that differences exist between the two historical groups (German and Mediterranean). Differences between the two historical groups lie even in the shape and trend of their SANS curves. In figure 6.1 are reported two curves for both the historical groups representative of the differences existing between them. These two qualitative results, enhance the fact that these two historical systems are effectively different even in the nanometric scale of the SANS, believing that these differences could be measured and discriminated through the SANS techniques.

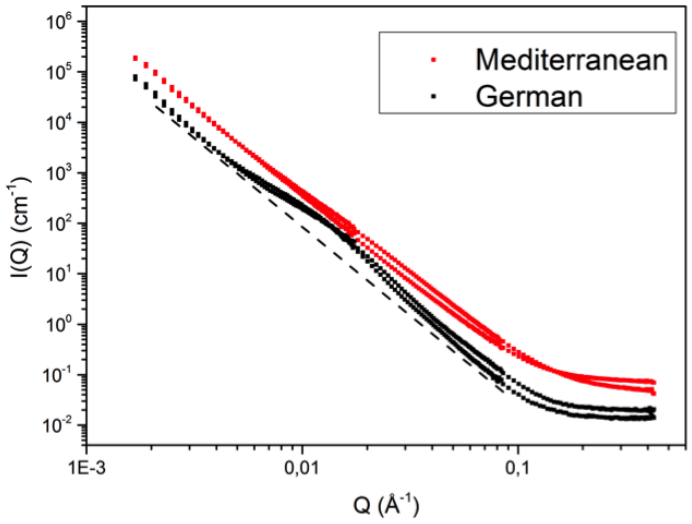

Figure 6.1: Example of SANS curves for the German group (black) and the Mediterranean group (red).

These differences regard the slope of the curves in log-log plot, the position of the signals on the Q axis and the incoherent scattering value
The linear trend (in the so called Porod Plot, i.e. a log-log plot), which constitute a sort of "linear" background characterised by a slope, has been related to the contribution of the bigger "object" inside the ceramics, which is assumed to result from the presence of the larger pores from few hundreds of nm to some µm (ceramic samples are assumed to be an ideal two phase system, for better detail see the following section). In this

region of linearity the scattering intensity $I(Q)$ have an exponential proportionality respect to the scattering vector Q $I(Q) \propto Q^{-d}$ where d is the slope in log-log plot. In a Porod plot, the value of the exponent could give information about the so called "fractal dimension", based on the value of the exponent d [4]. This shape of the curves will be subsequently treated in more detail in the next section 6.2. The background constant values visible at the high Q region of the curve is related to the incoherent scattering, which is Q independent. Incoherent scattering cross section for neutrons depends on the specific atoms and isotope which generate the scattering event. The composition of the ceramic matrix of the samples is determined by large amount of different compounds as oxides and minerals, defining ceramics as a complex system in this sense.

6.2 Surface fractal Analysis

Huge amount of information are contained inside the SANS data. By using the right mathematical instrument is possible to select and extrapolate specific information. As just wrote previously, ceramics analysed in this work are defined as a complex system of different compounds. In order to obtain primary knowledge about the system it has been performed a preparatory evaluation to study the behaviour of the surface of pores (in the range of dimension probed by the SANS), which is the surface fractal analysis [5].
The fractal analysis is involved to understand the relative degree of roughness of the interface between pores and matrix. correlating the roughness with the surface fractal dimension of the pores boundary interface. Ever since Mandelbrot promulgated the description of complex patterns in nature in terms of fractal geometry [6], this concept has been applied to the study of irregular objects and complex system in all branches of science [7, 8].

6.2.1 Fractal Structures

Fractal structures are classified into two categories, i.e., deterministic fractals and random fractals. A typical example of deterministic fractal structures are the Mandelbrot-given fractal, the Von Koch snowflakes fractal, etc., which are shown figure 6.2 [9]. A random fractal structure is less easier to explain. An example can be a Brownian motion or a fractal percolation, which are shown in figure 6.3 together with the pictures of typical fractals [9].

The fractal analysis is based on the Mandelbrot's idea of fractals , that are objects

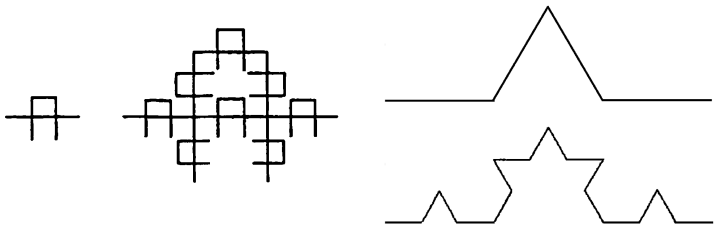

(a) (b)

Figure 6.2: Examples of deterministic fractal structures: (a) Mandelbrot-given fractal and (b) Von Koch snowflakes fractal.

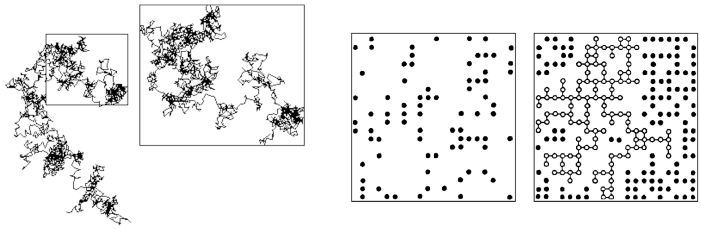

(a) (b)

Figure 6.3: Examples of random fractal structures: (a) Brownian motion and (b) fractal percolation.

possessing a dilation symmetry, that is, it retains a self-similarity under scale transformation [10]. In other words, if a fractal object is considered on a small scale, magnifying part of its structure, the enlarged portion looks like the original. Figure 6.4 shows a fractal shape, the Koch curve [11]. Observing the Koch curve is possible to understand the meaning of fractal; magnifying by three the part of the Koch curve in the interval $[0 \div 1/3]$, this part is similar to the whole shape. The same result appears if the part between $[0 \div 1/9]$ is enlarged to 1. In other words the structure of the object is independent of the characteristic length scale of observation.

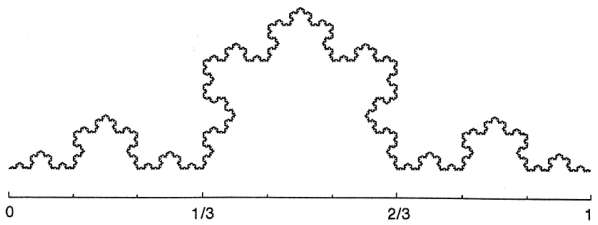

Figure 6.4: Representation of the Koch curve.

It is clear that such a situation will break down at some scale in a real experiment. This means that in a real world, an object can be considered as a fractal object and be

described by a fractal law only within some spatial range, covering at least one decade [10].
Every fractal objects are defined with two properties, the self-similarity and the fractal dimension. Taking for example a line and a plane, their spatial dimension are 1 and 2 respectively, and it can be easier to understand even the meaning of 3D space. These spatial dimensions are called euclidean dimensions, which take integer values. One definition for this quantity is as follows: supposing to divide a line a square and a cube into identical forms whose side are half the length, as it is shown in figure 6.5. The numbers of parts that now divide these geometric figures can be related to D by $N(2) = 2^D$, where the euclidean dimension D (=1,2,3) is given by:

$$D = \frac{logN(2)}{log2} \tag{6.1}$$

Generalising now this definition of dimension to fractal structure: for a deterministic fractal structure, $N(a)$ is the number of identical parts of size $1/a$ that compose the fractal object. Its dimension is now defined by

$$d_f = \frac{logN(a)}{loga} \tag{6.2}$$

where the quantity d_f is not restricted to integer values. This implies

$$N(a) = a^{d_f} \tag{6.3}$$

The exponent d_f is called the similarity dimension.

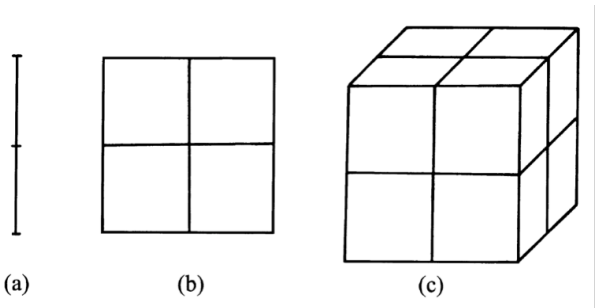

Figure 6.5: Example of the division of three geometric figures, which are: (a) a line divided into two segments, (b) a square divided into four parts, (c) a cube divided into eight parts.

Taking into account the Mandelbrot fractal shown in figure 6.6, it is composed of 8 parts of size $1/3$. Hence from the equation (6.2) the similarity dimension d_f for this

structure is

$$d_f = log_2 8 = 1.89278.. \tag{6.4}$$

Although the similarity dimension d_f extends the concept of euclidean dimension to non-integer values, it can be defined only for deterministic fractals.

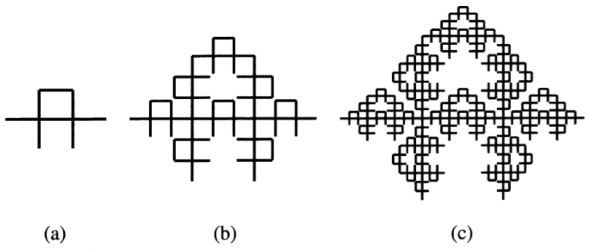

Figure 6.6: Construction of the Mandelbrot-fractal. (a) The initial structure, (b) the object obtained by replacing each line segment of (a) by the initial structure itself (second stage), (c) the third stage of the Mandelbrot-fractal obtained by replacing each line segment of the second-stage structure by the initial structure.

In order to allocate a dimension even to a random fractal structure, it is necessary to introduce another definitions of dimensions. The capacity dimension and the Hausdorff dimension are suitable for this purpose [12]. These dimensions are based on the coverage procedure [13]. The coverage method is based on the calculation of the numbers of the simple geometrical figures (like squares or circles) needed to cover the analysed random fractal. For example this procedure is now applied to the three objects in figure 6.5, with sphere of radius l. In this case the number of spheres $N(l)$ required would be proportional to (L/l), $(L/l)^2$, and $(L/l)^3$ for the line segment, the square, and the cube, respectively, where L is the size of shapes. This gives a new definition of to the numbers of identical particles needed to cover the fractal $N(a)$, expressed in equation (6.3), which becomes

$$N(l) \propto l^{-d} \tag{6.5}$$

where d is the capacity dimension, which coincides with the fractal dimension d_f written in equation (6.2).

Mass Fractal

If a sphere of radius r is drawn on a point of the fractal object, the fractal dimension describing its fractal behaviour is related to the mass contained inside this sphere. If the object is a line, the mass $M(r)$ within the sphere will be proportional to r. If it is a sheet, $M(r) \propto r^2$. If it is a solid three-dimensional object $M(r)$ would be proportional

to r^3. In a fractal the following general relation is obeyed,

$$M(r) \propto r^d \tag{6.6}$$

where the fractal dimension d is a number between 1 and 3. Since the volume of the sphere is proportional to r^3, the density $\rho(r)$ of actual material embedded in it is

$$\rho(r) \propto r^{d-3} \tag{6.7}$$

The range of validity of 6.7 is $R >> r >> a$, where R is the overall dimension of the object and a is the size of the building block of the structure (which could be if at all as small as an atom or a molecule). The 6.7 can be related to the scattering intensity $I(Q)$ in the case of a mass fractal. Therefore in the Porod regime, $1 << QR$ the scattering intensity of isotropic samples could be simply written as

$$I(Q) \propto Q^{-d_m} \tag{6.8}$$

where d_m is the mass fractal dimension [14]. Regarding this work of thesis, the Porod regime is consistent with the assumption that the sloping trend of the curves, which is analysed in this section with the fractal analysis, is due to the larger pores inside the matrix. In fact their overall dimension R is expected to be some thousand of Å or more, therefore the product between R and Q is certainly $<< 1$ (in the low Q region which goes approximately from $2x10^{-3}$ Å^{-1} to $3x10^{-2}$ Å^{-1}.

Surface Fractal

If objects posses rough surface and exhibit fractal properties, such objects are called surface fractal and are defined by the self-similarity under scale of transformation. An example of three-dimensional surface fractal is the clump of a cauliflower, while an island with a fractal coastline is an example of two-dimensional one. To understand better this concept of fractal dimension, it's easier to apply concept to a real object as an island. Covering it along its coastline with square tiles of edge length l, and marking those tiles that at least partially overlap the coastline. $N(l)$ is the number of marked tiles. If the coastline is smooth and nearly straight, $N(l)$ will be proportional to l^{-1}, in the same way even if tiles of different size would be employed. If the coastline is irregular and fractal, the number $N(l)$ of marked tiles depends more strongly on l, and is proportional to l^{-d_s}, where d_s is a number larger than one. The length $L(l)$ of

the coastline can be regarded as equal to $lN(l)$ or

$$L(l) \propto l^{1-d_s} \tag{6.9}$$

where d_s is the fractal dimension of this two-dimensional surface fractal. The fractal dimension of a three-dimensional surface fractal can be defined in a similar way. The d_s for a surface fractal in three-dimensional space ranges from 2 to 3, respectively indicating a perfectly smooth surface and highly rough surface.
An object can possess fractal behaviour related through its mass, its surface or even both of them. The difference between these two fractals is related even to the scale of probing with which the object is observed. In figure 6.7 is reported an example of the different regions in Q in which the two fractal behaviours could be found [15].

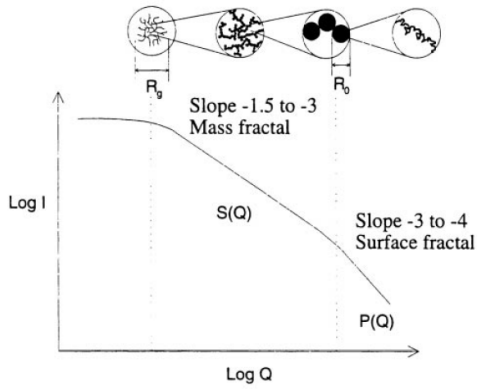

Figure 6.7: The sketch of the scattering intensity's behaviour in the case of both mass and surface fractal, which appear in different Q regions [15].

It is assumed that the system obey the ideal two-phase model, except for the interface boundary, instead of being smooth, is now fractal [11]. In this case one of the two phases is called empty phase described by the pores volume and is assumed a vacuum, the other phase is the matrix, assumed as homogeneous ceramic body. Form this assumption is possible to derive the correlation function from which the $I(Q)$ could be obtained. Even in this case (as has been done for the mass fractal), the surface fractal dimension can be extracted from the scattering curve in the regime $Q > a^{-1}$ as

$$I(Q) \propto Q^{-6+d_s} \tag{6.10}$$

where d_s is the surface fractal dimension [16]. In a Porod plot (log-log plot of $I(Q)$ against Q) the $I(Q)$ will therefore give a straight line, with the slope equal to $6 - d_s$. In the case of three-dimension surface fractal, d_s is between 2 and 3, so the exponent of Q has to be between -3 and -4. If the surface fractal dimension d_s is equal to 2,

the exponent of Q is -4. In this case the scattering law corresponds to the Porod law, and it indicates scattering arising from smooth interface boundary, i.e. smooth pore's surface. Value of d_s equal to -3 correspond to a highly rough fractal surface [11].

6.2.2 Data Analysis

Scattering curves measured at 6 Å for 3 SDD have been analysed with the surface fractal approach described above. The exponent of SANS curves of the Mediterranean and German samples have been obtained through their Porod plot, from the relationship between $I(Q)$ and Q, reported in the equation 6.10. Then the surface fractal dimension d_s has been calculated from the exponent α through the following equation

$$d_s = 6 - \alpha \tag{6.11}$$

The obtainment of the α exponent has been obtained from the slope of the linear fit, which has been calculated in the Q range from $2x10^{-3}$ Å^{-1} to $3x10^{-2}$ Å^{-1}. In figure 6.8 is reported an example of the linear fit done for a German sample (Bi_50). The fit

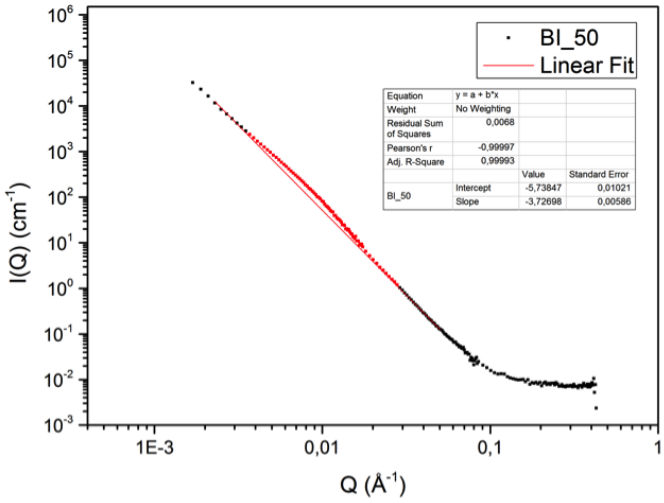

Figure 6.8: Example of a SANS curve of German historical sample, analysed with the surface fractal method. The red line is the linear fit of the curve in the log-log plot. The excluded region is defined by red data points showed in the figure.

has been calculated in the same data range for each SANS curves analysed with the surface fractal method.
The data input of the fit has been chosen in the way to conserve only the linear part of the log-log plot, excluding data points that are not related to the scattering of fractal objects (which are the red point in the figure 6.8). For this reason, it has been necessary

to mask the data range in which the signal ascribed to the nanometric pores appears, which goes approximately from $3.5x10^{-3}$ Å^{-1} to $2.5x10^{-2}$ Å^{-1}.

Results

Values obtained for the surface fractal dimensions d_s have been plotted in figure 6.9.

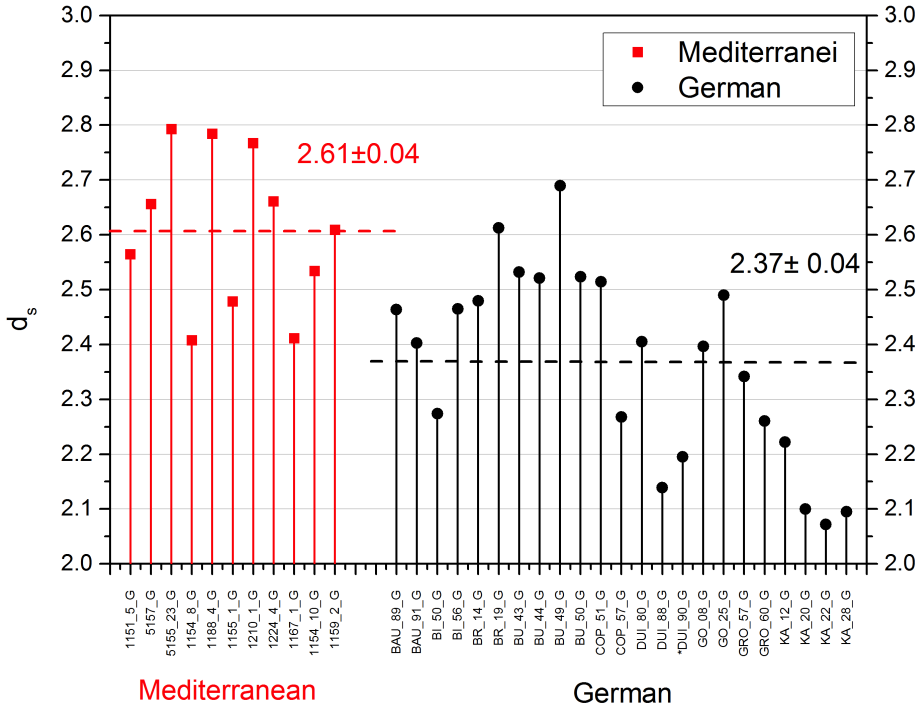

Figure 6.9: Surface fractal dimension d_s obtained from the fractal approach for the two different historical groups. The red squares indicate Mediterranean historical samples, the black dots indicate the German ones. Errors bars are not shown because the relative error are less than 1%.

From the figure 6.9 is possible to notice that Mediterranean samples have an average surface fractal dimension larger than the German ones, which are 2.61±0.04 and 2.37±0.04 respectively. Due to the fact that a d_s values of 3 is related to a rough fractal structure, Mediterranean samples show averagely a coarsest pore's surface. This result can be related to different aspects which characterise the two historical groups.
The firing Temperature is the first aspect which has to be taken into account. As it has been concluded in chapter 4, German samples can be divided into 3 different subgroup based on their firing temperature which are 750 - 850 °C, 900 - 950 °C and >950 °C. More than a half of the German samples analysed with the fractal analysis belong to the first subgroup.
All of the Mediterranean samples were fired at relative lower temperature (from 700 -

850 °C) compared to the German ones [17]. The firing temperature plays an important role on the morphological characteristics of the ceramics, in fact the higher the firing temperature, the more advanced the vitrification process on ceramic bodies is. This process (literally "turning into glass") is defined as the progressive partial fusion of a clay. It increases the intimacy of grains composing the ceramic's body, reducing the space between these grains and then the apparent porosity, producing a more homogeneous matrix. Due to the beginning of the partial fusion of grains (that starts from the surface and then goes gradually on the core of the grains), this process also produces a smoothed boundary surface and so pore's surface with a lower degree of roughness. It's possible to confirm that vitrification is a parameter that influences the smoothness of the pore's surface, through the observation of d_s values for the German samples fired at relatively higher temperature (T>950°C). In fact the d_s values for the Dui_88, Dui_90 and Ka_20 are relatively low (from 2.1 to 2.2) respect to the other German d_s values. Furthermore observing samples obtained from Duingen (labelled as "Dui"), it is possible to confirm that for these three samples the different firing temperatures have produced variations on the surface fractal dimension. Lower values of d_s are due to higher firing temperature, as reported in table 6.2. For other German samples, the relationship between smoothness of pores and the firing temperature, appears not as simple as it is reported above. In fact, comparing the d_s values for the Ka_12, Ka_20, Ka_22 and Ka_28, it is possible to notice that these relationship is not conserved. The Ka_20 which is fired at higher temperature (900 - 950 °C) than the others Ka_ samples (fired at 750 - 850 °C) does not have the lowest value of d_s, (which is 2.10), whereas the ka_22 has the d_s of 2.08.

Table 6.2: d_s values and firing temperature for German potteries recovered in Duingen (lower Saxony). The relative errors of the d_s are not shown because less than 1%.

Sample	d_s	Firing Temperature [°C]
Dui_80	2.405	750-850
Dui_88	2.139	>950
Dui_90	2.195	>950

Another example of missed relationship is the sample Bu_49 which is fired at 900 - 950 °C but exhibit the highest value of surface fractal dimension of its group (2.69), even higher than that of some Mediterranean samples. Due to these facts, it's possible to affirm that the firing temperature is only a factor that influences d_s and even the vitrification process.

The grain size of the raw materials employed to produce the ceramic objects is another

aspect that has to be taken into account. As the vitrification process start from the edge of grain, for smaller grains this process is quicker and even more efficient, especially if the firing temperature of ceramic samples is not higher enough to produce the complete melting of the ceramic body. From the SEM images shown in figure 4.4 and 4.11 (see chapter 4), the Mediterranean late antique amphorae exhibit a larger grains and less homogeneous matrix than the German shreds. This is due to the relative low temperature, the different raw materials, which are confirmed to be more rough and less finer than the German ones [18], and the different production techniques employed in the manufacturing process. It's important to stress that SEM images investigate dimension which are at least of one order of magnitude larger than the largest dimension detected by SANS, in the instrumental configurations employed. It is possible to conclude that the higher d_s values for the Mediterranean samples are influenced by their less homogeneous matrix. Their uneven ceramic matrix is due to different factors reported above. However due to the fact that the firing temperature of Mediterranean samples are similar to that of the majority of the German samples, which have averagely a lower value of d_s, the factor that mainly influences the matrix and so the d_s could be the characteristics of the raw materials in terms of roughness and fineness.

6.3 Porod's Invariant

The porosity is a dominant factor which affects the performance of materials such as the ceramic ones. Depending on the size of their nanopores, materials are usually classified/sorted as follows: microporous (pore sizes less than 2 nm), mesoporous (pore sizes of 2–50 nm), and macroporous (pore sizes over 50 nm). It is easy to imagine that nanoporosity influences hardness, density, high temperature mechanical strength, creep resistance and corrosion resistance in structural ceramics as well as in nanocomposite materials used for applications in engine parts, cutting tools, wear components, heat exchangers, and so on [19–22].
Small angle neutron scattering is a powerful tool to characterise the porosity of different type of materials such as the ceramic materials as it is reported later in this section [14]. SANS technique in this thesis is the means used to perform a non-destructive approach for the study of specific features of a pottery matrix that could open in future a route (based on the study of both open and closed nanopores) for exploring both historical and innovative ceramic-based materials. The Porod's invariant, applied in the specific case of a two phases system, is a useful analysis tool that can be applied to SANS curves to calculate the volume fraction and/or the specific area of the two phases of the measured sample. Contrary to other type of analysis in the neutron's

field, the strong point of the Porod's invariant is its dependence on the particle's volume only and not on its form.

6.3.1 The Invariant

The invariant was originally defined by Porod for the small-angle scattering [23]. The invariant Q_p is defined as the quantity obtained when $I(Q)$ is integrated with respect to Q throughout the whole reciprocal space, that is,

$$Q_p = \int I(Q)dQ = \frac{1}{(2\pi)^3}\int I(Q)dQ \tag{6.12}$$

In the case of an isotropic material for which $I(Q)$ depends only on the magnitude of Q, the equation 6.12 can be written as

$$Q_p = 4\pi\int_0^\infty Q^2 I(Q)dQ = \frac{1}{2\pi^2}\int_0^\infty Q^2 I(Q)dQ \tag{6.13}$$

The integration in 6.13 is extended to infinity, but in the context of small-angle scattering it is usually confined to small Q regions and the intensity at large Q is ignored, because assumed to be zero after the background subtraction.
Now the concept of invariant is applied to a real sample, on the assumption of the **ideal two-phase system**. This assumption impose that:

1. the system is composed of two different regions (or phases), each of constant scattering length density ρ_1 and ρ_2,

2. the two phases are well defined and the boundary between them is sharp. This second assumption does not agree with reality and meaningful results can be obtained even for the real case.

G. Porod has demonstrated that normalising the intensity $I(Q)$ in absolute unit, the equation 6.13 can be written in terms of the square differences between the scattering length density of the two phases [23, 24].

$$Q_p = \int_0^\infty Q^2 I(Q)dQ = V(\Delta\rho)^2\phi_{voids}(1-\phi_{voids}) \tag{6.14}$$

where $\Delta\rho$ is the difference between the scattering length densities of the two phases and V is the total volume measured for the sample. In the present case of study, the two phases are the voids (ceramic pores) and the ceramic matrix, which are defined by the volume fractions ϕ_{voids} and $\phi_{solid} = (1-\phi_{voids})$ respectively.

The invariant can be considered of the overall scattering power of the sample independently on its geometry. The word "invariant" stress the fact that its value depends only on the mean square fluctuation of the scattering length density between the two phases and on their volume fraction. The scattering length density of a composite ρ (or usually indicated as SLD) could be imagine as the scattering power density of the atoms in the sample (its formula is shown in equation (5.9), in chapter 5, section 5.2). It is calculated with the scattering lengths b_i of the atoms composing the sample. The scattering length of an atom is a distance which is connected to the interaction of the neutron with the nucleus of that i-atom, during the scattering event.

In this work of thesis, the Porod's invariant has been involved to study the sample's porosity in two different ways.

1. The Porod's Invariant has been calculated for the samples measured at 6Å for 3 SDD in "Dry" conditions (i.e. in atmospheric air environment, see chapter 5, section 5.1). This analysis has allowed to obtain information about the total porosity.

2. The Porod's invariant has been calculated for samples measured at 6Å for 3 SDD in "Wet" conditions (i.e. soaked in a mixture of H_2O/D_2O). The results obtained for this analysis are reported in the next section 6.4. This analysis has allowed to obtain information about the ratio between the closed pores on the total ones.

6.3.2 Total porosity with the Porod's Invariant

The results obtained for the Porod's Invariant analysis applied for the ceramic samples measured at 6Å for 3 SDD in "Dry" condition are reported in this section. Due to the fact that the samples were measured directly in atmospheric air environment, the $I(Q)$ obtained from the data reduction is related to the scattering coming from the whole samples. In this conditions neutrons are probing completely all the two phases (ceramic matrix and voids) and so the Q_p is related to the volume fraction of the total pores (open plus closed ones). In fact one of the factors that makes the neutron techniques a unique tool in the characterisation of the morphology and especially the porosity is that neutrons can pass through the whole samples. Other techniques capable of probing the porosity, like the MIP or the N_2 adsorption, are limited to the open pores only. In fact for the further comparison between MIP and SANS results reported below, it is important to remember that the MIP ones are restricted to the open porosity only.

6.3.3 Data Analysis

The procedure for the data analysis is divided in two steps:

- the calculation and the removal of the background;
- the integration of the $I(Q)Q^2$ with respect to the Q.

The **first step** is very thorny and has to be carried out judiciously and correctly. For the Porod's Invariant analysis, the behaviour of the scattering intensity at higher scattering vectors plays a significant role. The higher angle part of the $I(Q)$ corresponds to the small interparticle distances, therefore in the high Q regime the scattering from the internal structure and in particular near the particle surface is dominating. In this region the incoherent scattering background becomes more relevant, because the $I(Q)$ value decrease with the increasing of the scattering vector Q. In the case of condensed matter it is possible to achieve the incoherent scattering value, measuring the $I(Q)$ for $Q > 0.4$ Å^{-1} [25]. The background of the samples curves have been obtained averaging

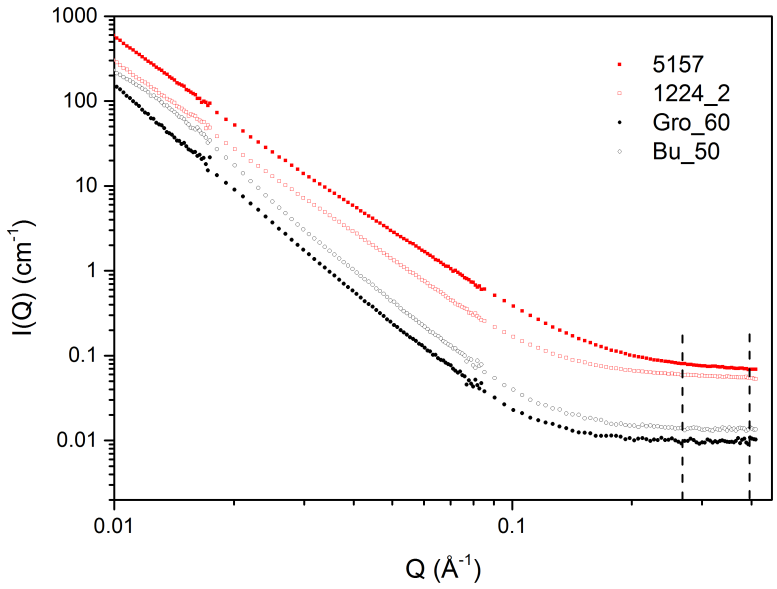

Figure 6.10: Magnification of the high Q part for two historical samples. In black are reported the German samples Gro_60 and Bu_50 while in red are reported the Mediterranean samples 5157 and 1224_2.

the flat part of the $I(Q)$ at high Q, which ranges averagely from 0.25 Å^{-1} to the highest Q value, which for the curve obtained at 6 Å is 0.427 Å^{-1}. The flat range in the high Q varies for the samples, therefore the lower Q limit for the quantification of the incoherent background depends on the samples. In figure 6.10 is shown a magnification of the

high Q part of two SANS curves for each historical group. The incoherent background values obtained were then subtracted to each $I(Q)$ curve.
The second step now concern the integration of the $I(Q)Q^2$ with respect to the Q as it's reported in equation 6.14 obtaining the Q_p value for each sample. The integration was performed in the Q range from 1.68x10^{-3} to 4.27x10^{-1} Å^{-1}.

Results

The Q_p values obtained were normalised on the highest Q_p values calculated which belong to the Mediterranean sample 5157. The normalised Porod's Invariant values $Q_{p,norm}$ are reported in figure 6.11. From the results obtained for the normalised

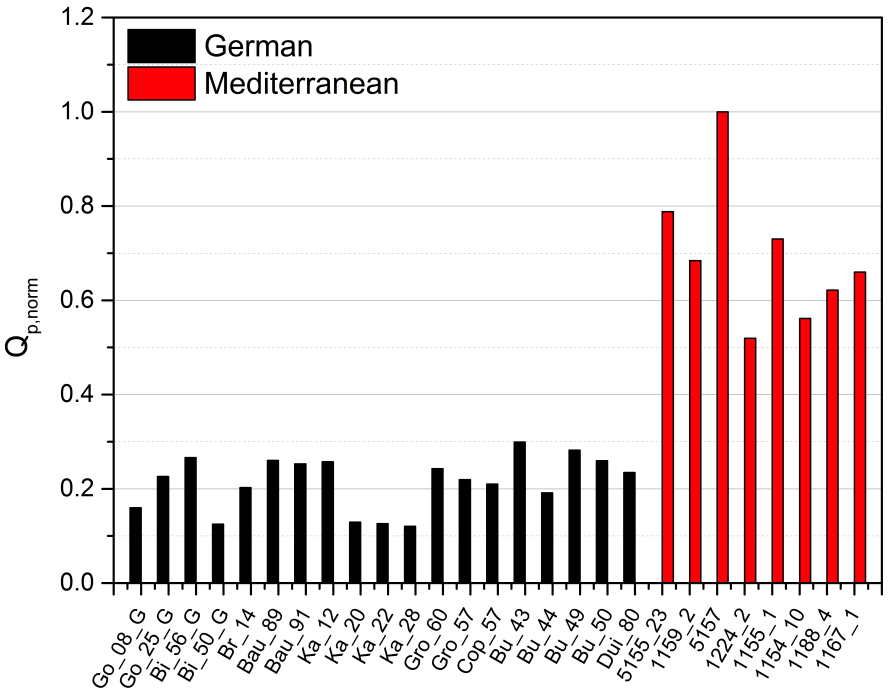

Figure 6.11: Diagram reporting the Porod invariant, $Q_{p,norm}$, for samples from the German group (black lines) and from the Mediterranean group (red lines). $Q_{p,norm}$ values are normalised to the maximum value. Reported values are significant for the total pore volume (open and closed pores).

Porod's Invariant, it is possible to notice a distribution of the $Q_{p,norm}$ values in two well-distinguished groups, corresponding to the origin of the samples. This trend underline the existence of differences between the two groups of potteries. The mean value of the normalised total porosity for the German samples is 0.21±0.01, which is much less than the value for the Mediterranean samples (0.70±0.05). As reported above, the $Q_{p,norm}$ values give information about the total volume and the volume fraction of the pores. From the results obtained with this analysis is evident that Mediter-

ranean samples are characterised by a higher pores volume. This is particularly true in this case for the ceramics samples analysed, because the SLD values are averagely the same for the two historical groups which is about $2x10^{-6}$Å^{-2} (see the next section for the Contrast method). The composition and consequently the scattering length density of samples do not influence their Q_p values; for example the 5157 Mediterranean sample (used for the normalisation) possesses a SLD value ρ_{solid} = $2.31x10^{-6}$ Å^{-2} and Q_p = 1 (normalised value), while for the German sample Cop_57 the normalised Porod's Invariant is Q_p = 0.21 even if it has the same SLD value (ρ_{solid} = $2.31x10^{-6}$ Å^{-2}).
Another confirmation that the Mediterranean samples are characterised by pores with larger volumes comes from the comparison between the incoherent scattering value obtained at high Q (the procedure employed to obtain these values are reported above, see the data treatment section). In fact the incoherent value evaluated for each SANS curves could be related to the amount of atmospheric H_2O inside the open pores of the ceramic shreds. This is particularly true in this case for different reasons. Firstly the coherent SLD of the ceramic matrix are averagely the same for the two historical groups as it is reported above. Furthermore the incoherent cross section σ_{incoh} of the Hydrogen atoms is at least of three orders of magnitude higher than the incoherent cross sections of the atoms composing the ceramic matrix (see figure 5.5 in chapter 5, section 5.2). The incoherent scattering value which appears in the SANS curves is mainly due to the presence of hydrogen atoms of the H_2O trapped in the open pores. The contribution coming from the H atoms of the hydroxyl groups of the ceramic are neglected. The main contribution to the presence of hydrogen atoms inside the matrix is due to the presence of re-hydrated Gypsum in the surface of ceramics during the burial periods and the presence of Kaolinite, Montmorillonite and Illite not completely dehydroxylated. These minerals are wide used as raw materials and their dehydroxilation reaction have been widely studied. Nevertheless the removal of water and the dehydroxilation reaction are complex reactions and their evolution depends upon the structure of ceramics matrix [26]. Therefore the estimation of the amount of hydrogen atoms inside the ceramics becomes excessively complex. Trying to evaluate the presence of hydrogen atoms inside the ceramics matrix, that cannot be detected with SEM-EDX and XPS, the FT-IR and Raman analyses are involved (see chapter 4). Due to the fact that the firing temperature of ceramics is equal or higher that 750 °C, we can consider the montmorillonite and illite as almost completely dehydroxylated and neglect their contribution to the amount of hydrogen atoms [26]. The presence of Kaolinite (which dehydroxylation reaction take place at lower temperature but can persist until 950 - 1100 °C) and the re-hydrated Gypsum have been evaluated through both FT-IR and Raman Intensity signals and XRF and SEM-EDX analyses. It is possi-

ble to assume that for the qualitative purpose of this analysis, the amount of hydrogen atoms coming from these two compound is not so relevant and is negligible. In figure 6.12 are then reported the incoherent values obtained from the SANS curves of samples analysed thorough the Porod's Invariant analysis.

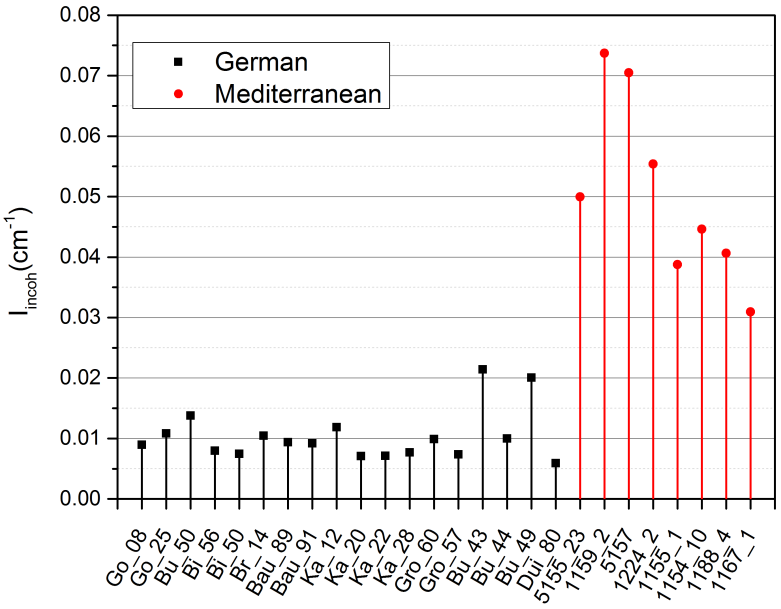

Figure 6.12: Trend of the incoherent scattering values obtained from the SANS curves of both German and Mediterranean samples measured at 6 Å for 3 SDD.

As it is possible to notice the incoherent scattering trend simulate quite well the Q_p ones, which is observable in figure 6.11. There is a little differences between these two, regarding for example the higher incoherent value which do not belong to the 5157 sample ($I_{incoh} = 0.705$ cm^{-1}) but it comes from the 1159_2 ones ($I_{incoh} = 0.735$ cm^{-1}). Some similarities can be noticed between the porosity obtained from the Mercury Inclusion Porosimetry (MIP) showed in figure 6.13 and the Q_p values obtained from SANS. It is important to underline that MIP technique probes pores from some nm to tens of μm and it is limited to the open pores only while SANS probes pore's dimension from some Å up to averagely 600 nm. From the MIP results it is possible to notice that the porosity is quite different for the two historical groups but not as evident as in the case of the $Q_{p,norm}$. The average value for the porosity of the two historical groups are (12±3)% and (23±2)% respectively for the German and the Mediterranean ones. The 5157 Mediterranean samples exhibit the highest value of porosity (34%) even through MIP analysis.

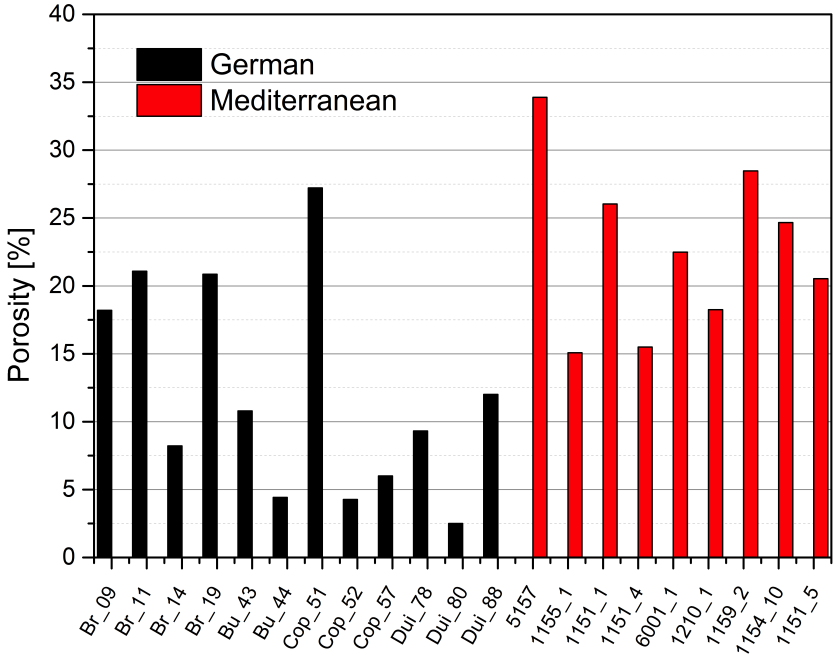

Figure 6.13: Histogram of open porosity (given as the % ratio between the open pore volume and the equivalent sample volume) as obtained by using Washburn's equation [27].

6.4 Closed porosity with the Contrast Method

To introduce the contrast method employed to study the closed porosity, it is important to introduce before the concept of "contrast" in neutron techniques. Representing schematically the coherent scattering intensity $I(Q)$ for a colloidal solution as example, it's possible to notice that it depends mainly from: the volume fraction of dispersed particles ϕ, the volume V, the structure factor $S(Q)$, the total form factor $P(Q)$ and the total scattering length density of sample's atoms $\Delta\rho$ [28]

$$I(Q) = \phi V(\Delta\rho)^2 P(Q) S(Q) \tag{6.15}$$

If these particles are dispersed in a mixture of H_2O/D_2O the total scattering length density will be obtained as

$$(\Delta\rho)^2 = (\rho_{particles} - \rho_{mixture})^2 \tag{6.16}$$

The SLD is a property of the interaction between neutrons and the nuclei which allows the neutrons to be highly sensitive on atomic composition of the sample. One of the common techniques which is based on this highly sensitivity of neutrons to the atoms and isotopes is the contrast technique based on the measurement of samples soaked in

different medium (which are usually a mixture of H_2O/D_2O). Changing the composition of this mixture, different value of its SLD will be obtained. If an ideal two-phases sample (A/B) are immersed in a mixture of H_2O/D_2O which has the same scattering length density of the phase "A", this one become "invisible" to neutrons. i.e. it is now contrasted and neutrons see it as if it is part of the solvent. For example, observing the figure 6.14, if a dispersion of silica particles (orange sphere) and PEG (polyelty-lene glycole which are represented by the dark blue objects) in water, it is possible to contrast the PEG polymers through a mixture of H_2O/D_2O, obtaining the “pure” scattering of silica particles.

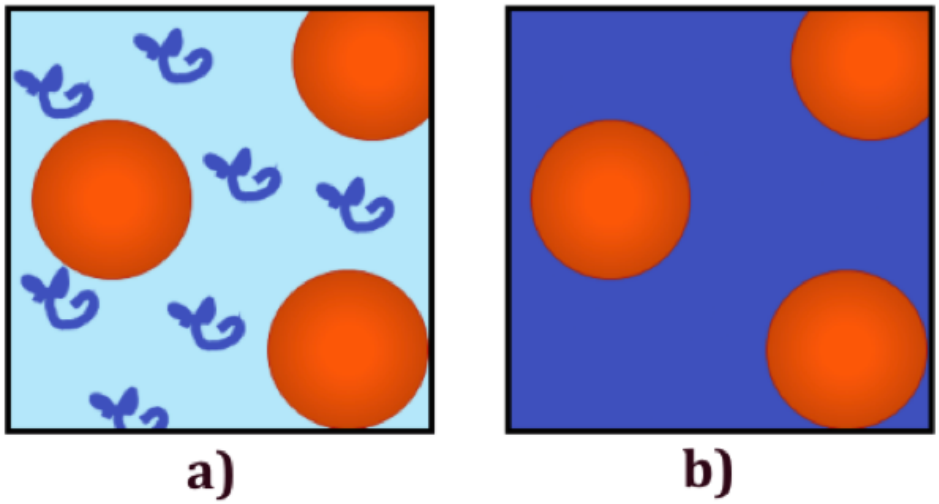

Figure 6.14: Illustration of the neutron contrast for silica particle (orange spheres) and PEG polymers (blue coils) dispersed in: a) pure heavy water D_2O, b) mixture of 15% D_2O and 85% H_2O.

6.4.1 The Contrast Method

The contrast method in SANS technique is used to highlight a part of the system in analysis and separate the contribution to the scattering from different phases. As reported above, usually the contrast of solvent is adjusted to match a specific component of the sample performing a series of measurements using different mixtures of deuterated-hydrogenated solvent (often heavy water and light water) as described in the references [29, 30]. Considering that SANS beam-time can only be obtained through a highly competitive proposal system, and is therefore very limited, we could not follow this procedure and determine and adjust the H_2O/D_2O match point for the large number of samples measured in this study. Therefore to perform the analysis of the closed pores, the water mixture employed in the contrast method has been

prepared on the basis of the bulk density and the composition (obtained from both SEM-EDX and XPS analysis) of the samples previously determined in the Ricci's thesis [18].
The scattering length density (SLD) values of the solid, i.e. of the ceramics matrix of samples were obtained through the SLD calculator function implemented in the SasView software [31] taking into account the bulk densities and the compositions of some samples listed in table 6.3 and 6.4. For the German samples the mean value of SLD is (2.1±0.1)x10^{-6} Å^{-2} and for Mediterranean ones it is (2.0±0.2)x10^{-6} Å^{-2}. These two values are close to each other as it is expected, because the composition of the different samples changes only for minority components as the clays contain to a vast majority silicates. That implies the lack of determination for the matching point for each sample does not influence the values obtained for Q_p in the analysed region.

Table 6.3: SLD values calculated for the German samples.

Sample	SLD [10^{-6}Å^{-2}]
Br_19	2.04
Br_14	2.43
Br_09	1.63
Bu_43	1.89
Bu_44	2.59
Cop_57	2.30
Cop_51	2.66
Dui_80	1.38
Dui_88	2.25

Table 6.4: SLD values calculated for the Mediterranean samples.

Sample	SLD [10^{-6}Å^{-2}]
5157	2.31
1159_2	1.59
1210_1	1.68
1151_5	2.27
1151_1	2.33

6.4.2 Data Analysis

The data treatment of the SANS curves of the samples in "Wet" conditions was performed in the same way as it has been done for the total porosity analysis in the case samples measured in "Dry" conditions (see the data treatment of the "Total porosity with the Porod's Invariant"). The composition of the H_2O/D_2O mixture was prepared on the basis of the average SLD values between the two historical groups which is 2.0x10^{-6} Å^{-2}. This SLD values for the mixture has been obtained with a water solution of 63/37 % vol of H_2O/D_2O.

Results

The contrast method has allowed to investigate the closed porosity shedding light on the complexity of porosity in ceramics. This analysis, together with the others involved in this study has helped to solve the puzzle of closed and open porosity. For

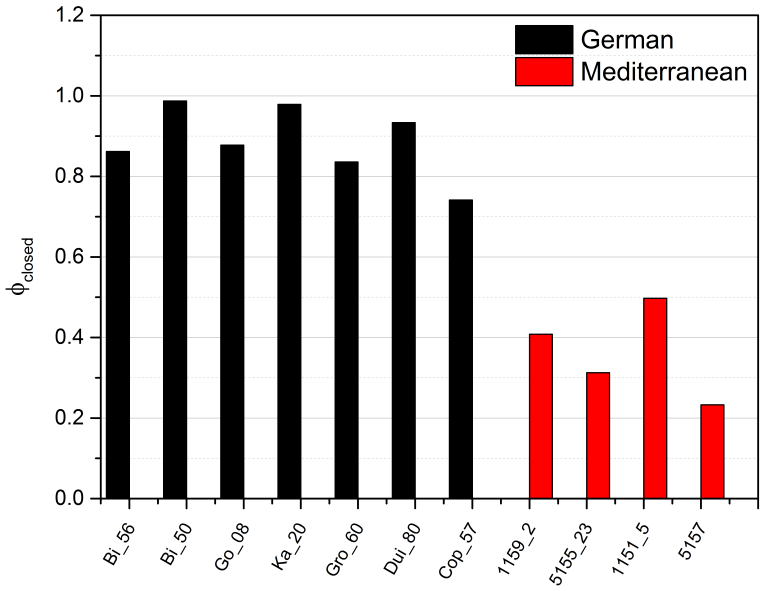

Figure 6.15: Diagram reporting the ratio between the closed pore volume and the total pore volume, ϕ_{closed}, for samples from the German group (black) and from the Mediterranean group (red).

each sample the Q_p values obtained for the measurement in the "Wet" condition has been normalised for the Porod's Invariant calculated in the "Dry" condition. This ratio express the volume fraction of the closed pores. Due to the fact that the SLD values of the historical ceramic shreds are averagely the same and then the open pores have been masked with the H_2O/D_2O mixture, the ratio between $Q_{p,Wet}/Q_{p_Dry}$ gives the volume fraction of the closed pores on the total ones, ϕ_{closed}, as reported in figure 6.15. Once again a marked difference between the two groups is observed. In the German samples, around 90% of the total pore volume is due to closed pores, while for Mediterranean samples the ratio is around 40%. In figure 6.16 are reported the SANS curves for two ceramic samples measured in "Wet" and "Dry" condition, representative of the two historical groups. For a better comparison between the curves, the incoherent scattering value of the "Wet" sample has been re-scaled on the "Dry" ones.

Through these results, ceramic pores are not only described by a volume or a volume fraction, but they start to take a form. In fact to mask the open pores, the contrasting mixture has to penetrate inside the matrix moving along the open pores. The

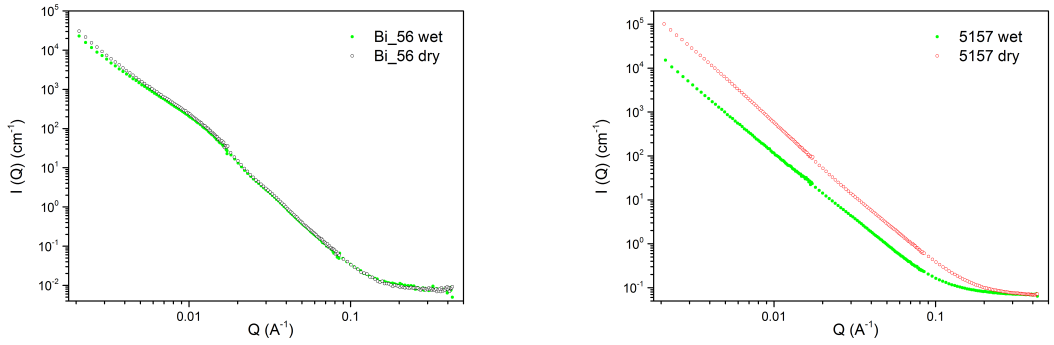

(a) (b)

Figure 6.16: Comparison of the scattering intensity $I(Q)$ vs Q for samples measured in air labelled as "Dry" and in the mixture of H_2O/D_2O labelled as "Wet", which are:(a) the German sample Bi_56 and (b) the Mediterranean sample 5157.

low value of the closed pores with respect to the total ones for the Mediterranean samples make it possible to predict an imagine of the pores in which they are extended deeper inside the ceramic matrix, interconnecting with each other. On the other hand the open pores in German samples seem to be not extended toward the core of the ceramic matrix as the Mediterranean ones and even less interconnected.

6.5 Form Factor Investigation

The SANS technique can be used to obtain structural information of the sample. If the studied system is composed of a collection of certain type of objects, though the mathematical models for the description of the scattering intensity $I(Q)$ it is possible to obtain information about the geometry and the interaction between the objects composing the system. The procedure of mathematical description of the scattering curve is called "modelization of the scattering intensity".
This analysis is based on the description of the $I(Q)$ by means two quantities which are function of the scattering vector Q that are the particle form factor $P(Q)$ and the structure factor $S(Q)$,

$$I(Q) = \phi V_p (\Delta\rho)^2 = K_c P(Q) S(Q) \tag{6.17}$$

where K_c is the contrast factor [25]. The form factor is a function that describes the geometry of the scattering object, while the structure factor describes the correlation between the particle mass centres.

In this work of thesis the porosity of the ceramic samples has been studied by the obtainment of the form factor of the pores.
The modelization analysis has been performed in this work of thesis through the fit of the $I(Q)$ curves of samples, by means of the SasView Software Package [31], that provides a large library of models for both form factors and shape independent models.

6.5.1 The Form Factor

The factor of the "intra-particulates structure" even called form factor $P(Q)$ is a function which describes how the scattering intensity is modulated by the resulting interference from the neutrons scattered by the atoms of the studied object. Considering a simple case of polymer particles in solution, the $P(Q)$ depends on the disposition of the atoms whit respect to the centre of mass of the macro molecule, i.e. from its form. In other words the $P(Q)$ is the analytical expression of the atomic arrangement in the reciprocal space.

Regarding the form factor, two possible approach may be applied to perform its determination.

1. The **direct method** consist in calculating analytical expression which are compared to the experimental data by varying parameters (like particle radius, length, polydispersity, etc) in order to minimize the χ^2:

$$\chi^2 = \sum_{N-x} [(I_{model}(Q) - I_{exp}(Q))/E(Q)]^2/(N-x) \tag{6.18}$$

   where $E(Q)$ is the error on the experimental intensity, x is the number of variables of the analytical expression and $N - x$ is the number of degrees of freedom [32].

2. The **indirect methods** use the inverse Furier transform of the experimental data which provides the pair distance distribution function $p(r)$ or the correlation function $\gamma(r)$ [24]. These methods were not employed in this work of thesis.

6.5.2 Data Analysis

The ceramic samples analysed in this thesis are a complex system due to the facts that they are historical object which are constituted by a vastness of different oxides and compounds. For these reasons the form factor analysis was not easy and has required a lot of time and efforts to find the correct analytical expression to describe the form

factor. Based on the SANS results reported in the chapters above and the previous characterisation performed by Dr. Giulia Ricci, which are reported in chapter 4, a lot of different models were explored to achieve the correct geometrical description of the pores. Some examples of shape dependent models from the SasView library, which were tested are: Sphere [24], triaxial ellipsoid [33], cylinders [32] and lamellar fissure [34]. Moreover different types of independent models were tested, for example: the Guinier-Porod model[35], the correlation length model [36] and the teixeira model for fractal objects [10]. None of these models have allowed to obtain a good value of the χ^2 and a satisfying description of the pores's form factor.
The best fit to describe the scattering coming from the nanopores resulted to be the Flexible Cylinder Elliptical (FCE) model [37, 38]. For a complete description of the $I(Q)$ curves, a power law (PL) has been added, which has been used to take into account the tails of the scattering from larger pores occurring at the lower Q region outside of the probed Q range [39]. The $I(Q)$ analytical expression is then described as follows

$$I(Q) = scale_a[scale_b P(Q)_{FCE} + PL(Q)] + bg \tag{6.19}$$

where the $scale_a$ and $scale_b$ are the scaling factor of the form factor.
The detailed analytical expression of the FCE form factor $P_{FCE}(Q)$ is reported in the reference [37], in which some correction to the Pedersen and Schurtenberger [38] form factor expression has been done. Briefly the $P_{FCE}(Q)$ can be divided in two parts

$$P(Q)_{FCE} = S(Q, L, b)_{WC} * P(Q, R_{CS}, x)_{CS} \tag{6.20}$$

where the $S(Q)_{WC}$ is the scattering function of single semi-flexible chain which is function of the scattering vector Q, the contour length of the semi-flexible chain L and the Kunh length b that are the rigid rods that forms the chain. The $P(Q, R_{CS}, x)_{CS}$ is the scattering function from the cross section of a rigid rod with an elliptical cross section, which is function of the Q, the major radius $R_{CS} \equiv R_{Major}$ and the ratio between the two radii $x \equiv R_{Major}/R_{Minor}$ of the elliptical cross section.
The FCE model considers a flexible cylinder with a uniform scattering length density and elliptical cross section, characterised by a minor radius R_{Minor} and a major radius R_{Major}. The form factor is normalised by the particle volume, by averaging over all possible orientations of flexible cylinders. Referring to the Figure 6.17 in which is depicted a schematic picture of the FCE model, the flexible cylinder formed by a chain of total length L (contour length), composed by a number of stiff segments of length l_p. The Kuhn length is defined as $b = 2l_p$, with l_P being the persistence length: it is a measure of the stiffness of the chain and can be related to its tortuosity which is defined as

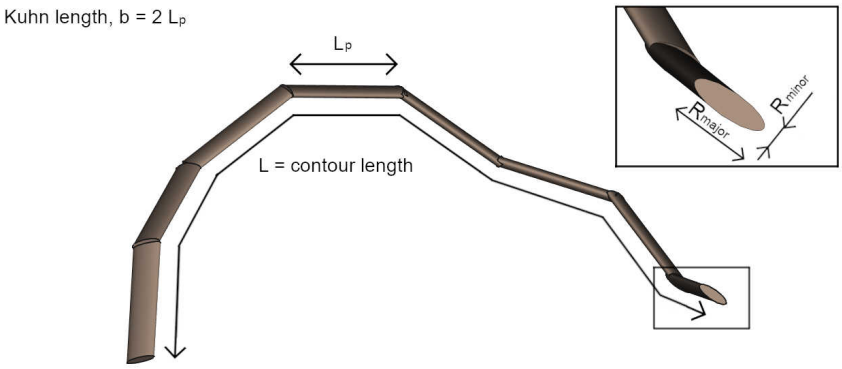

Figure 6.17: 3D depiction of the FCE model

the ratio between the contour length and the rigid rod,

$$tortuosity = \frac{L}{l_p} = \frac{2L}{b} \tag{6.21}$$

For the FCE model it's possible to calculate the average distribution of the major radius which is indicated as PD_{Rmajor}. The meaning of polydispersity parameter PD has not to be confused with a molecular weight distributions in polymer science. The distribution function used to describe the PD_{Rmajor} is a Gaussian distribution function and the polydispersity is defined as follows:

$$PD_{Rmajor} = \frac{\sigma}{\bar{x}} \tag{6.22}$$

where σ is the standard deviation and $\bar{x}$ is the mean value of the distribution.

Results

The results obtained with the FCE+PL model are reported in table 6.5 and 6.6, respectively for the German and Mediterranean samples analysed.
In table 6.7 are reported the average values for the main shape parameters of the best fit obtained for both the two historical groups. The polydispersity has been evaluated for the major radius R_{major} and the average values obtained are 0.34 ± 0.02 and 0.41 ± 0.07 respectively for the German and Mediterranean samples modelized. The errors related to the *tortuosity* values have been obtained by the propagation of uncertainty of L and b. The results show that the pores in the Mediterranean samples are longer than in the German samples. Their shape is more squeezed (they have more or

Table 6.5: Values obtained for the main shape parameters from the fit of the German samples.

Sample	Contour length L [nm]	Kunh length b [nm]	Major radius R_{major} [nm]	Axis ratio	Tortuosity, $2L/b$
Dui_80	101±6	83±1	13±1	4.0±0.3	2.4±0.1
Cop_57	500±40	152±4	25±2	3.5±0.5	6.6±0.6
Bu_49	460±20	120±2	8.6±0.3	1.9±0.1	7.7±0.4
Bu_44	280±10	125±4	16±1	7.6±0.2	4.5±0.2
Br_14	270±20	170±5	15±1	8±1	3.2±0.3
Bi_50	170±10	93±1	18±2	5.8±0.4	3.7±0.2
Bau_91	530±30	129±3	15±1	6.0±0.6	8.2±0.5
Bau_89	96±5	29±1	15±1	4.2±0.3	6.6±0.4

Table 6.6: Values obtained for the main shape parameters from the fit of the Mediterranean samples.

Sample	Contour length L [nm]	Kunh length b [nm]	Major radius R_{major} [nm]	Axis ratio	Tortuosity, $2L/b$
5155_23	540±30	50±3	6±1	6±1	22±2
5157	790±60	20±1	15±1	5.2±0.5	79±7
1224_2	800±50	20±2	10±1	10±1	80±9
1159_2	800±60	25±1	14±2	7.2±0.8	64±5
1151_5	850±70	50±2	10±1	10±1	34±3

less the same major radius but a very different axis ratio): this is consistent with previous results regarding the anisotropy of the Mediterranean samples. Furthermore the contour length L of the Mediterranean samples is averagely longer than the German ones, confirming the results obtained with the contrast method (see section 6.4), which has evidenced the fact that Mediterranean ceramic shreds have elongated pores which are interconnected with each others.

Table 6.7: Average values for the main shape parameters obtained by worm like flexible cylinders model for the nanopores.

Samples	Average L [nm]	Average b [nm]	Average R_{major} [nm]	Average Axis ratio	Average tortuosity
Mediterranean	750±50	30±10	11±2	8±1	60±20
German	300±60	110±20	16±2	5±1	5±1

Another results emerging from this analysis is the ratio between the contour length L and the unit segment L_p as an indication of pore tortuosity. The Mediterranean samples are significantly more tortuous than German ones.
In Figure 6.18 it is reported as example the $I(Q)$ data with the best fit for the two

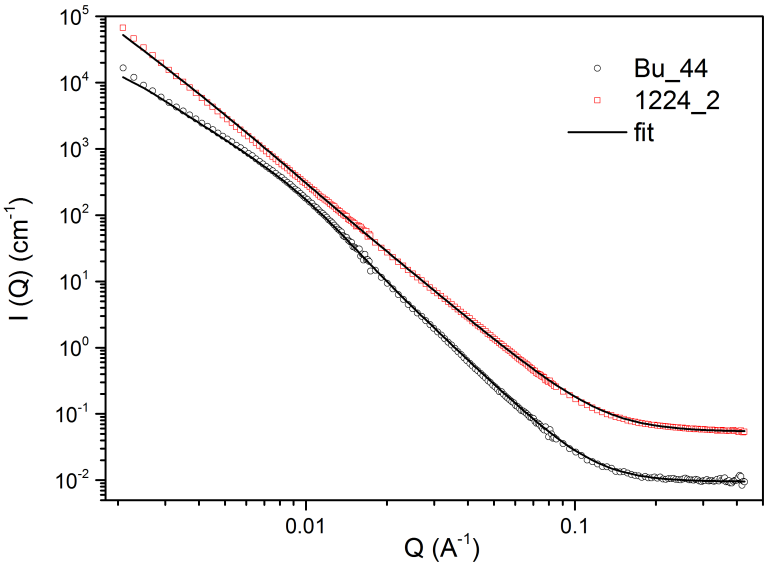

Figure 6.18: Scattering intensity $I(Q)$ vs Q for both historical samples, together with the best curve fit obtained by using the model described in the text. Black dots are related to the Bu_44 German sample, red square for the 1224_2 Mediterranean sample, solid black line is for the fit curves.

samples Bu_44 and 1224_2 , belonging to the two historical groups (the parameters of the fit are reported in table 6.5 and 6.6).

Bibliography

[1] E. Gandon, R. Casanova, P. Sainton, T. Coyle, V. Roux, B. Bril, R. J. Bootsma, *Journal of Archaeological Science* **2011**, *38*, 1080–1089.

[2] N. di Caprio, *La ceramica in archeologia, 2: antiche tecniche di lavorazione e moderni metodi di indagine*, L'Erma di Bretschneider, **2007**.

[3] M. Courty, V. Roux, *Journal of Archaeological Science* **1995**, *22*, 17–50.

[4] R. Raut Dessai, J. Desa, D. Sen, S. Mazumder, *Journal of Alloys and Compounds* **2015**, *628*, 97–101.

[5] M. Winterer, *Nanocrystalline Ceramics: Synthesis and Structure*, Springer Berlin Heidelberg, **2013**.

[6] B. B. Mandelbrot, *The fractal geometry of nature /Revised and enlarged edition/*, **1983**.

[7] H. D. Bale, P. W. Schmidt, *Physical Review Letters* **1984**, *53*, 596–599.

[8] P. W. Schmidt, *Journal of Applied Crystallography* **1991**, *24*, 414–435.

[9] A. Bunde, S. Havlin in *Encyclopedia of Complexity and Systems Science*, (Ed.: R. A. Meyers), Springer New York, New York, NY, **2009**, pp. 3700–3720.

[10] J. Teixeira, *Journal of Applied Crystallography* **1988**, *21*, 781–785.

[11] R. Roe, *Methods of X-ray and Neutron Scattering in Polymer Science*, Oxford University Press, **2000**.

[12] A. J. Chorin, *Journal of Computational Physics* **1982**, *46*, 390–396.

[13] K. Foroutan-pour, P. Dutilleul, D. Smith, *Applied Mathematics and Computation* **1999**, *105*, 195–210.

[14] D. W. Schaefer, A. J. Hurd, *Aerosol Science and Technology* **1990**, *12*, 876–890.

[15] D. P. Serrano, R. van Grieken, *Journal of Materials Chemistry* **2001**, *11*, 2391–2407.

[16] D. F. R. Mildner, P. L. Hall, *Journal of Physics D: Applied Physics* **1986**, *19*, 1535–1545.

[17] C. Mondelli, S. Zorzi, G. Ricci, V. Galvan, E. Balliana, R. Schweins, E. Cattaruzza, *ChemPhysChem* **2020**, *21*, 966–970.

[18] Giulia Ricci, PhD thesis, Ca'Foscari Venezia, **2016**, 203 pp.

[19] C. B. Carter, M. G. Norton, *Ceramic Materials*, Springer New York, New York, NY, **2013**.

[20] M. S. Ali, M. A. A. Hanim, S. M. Tahir, C. N. A. Jaafar, N. Mazlan, K. Amin Matori, *Advances in Materials Science and Engineering* **2017**, *2017*, 1–10.

[21] P. Tenorio Cavalcante, M. Dondi, G. Ercolani, G. Guarini, C. Melandri, M. Raimondo, E. Rocha e Almendra, *Ceramics International* **2004**, *30*, 953–963.

[22] M. Raimondo, M. Dondi, D. Gardini, G. Guarini, F. Mazzanti, *Construction and Building Materials* **2009**, *23*, 2623–2630.

[23] G. Porod, *Kolloid-Zeitschrift* **1951**, *124*, 83–114.

[24] O. Glatter, O. Kratky, *Small angle x-ray scattering*. _eprint: https://onlinelibrary.wiley.com/doi/ London: Academic Press, **1982**, 296 pp.

[25] I. Grillo in *Soft Matter Characterization*, (Eds.: R. Borsali, R. Pecora), Springer Netherlands, Dordrecht, **2008**, pp. 723–782.

[26] C. M. Stevenson, M. Gurnick, *Journal of Archaeological Science* **2016**, *69*, 54–63.

[27] E. W. Washburn, *Phys. Rev.* **1921**, *17*, Publisher: American Physical Society, 273–283.

[28] S. Kumar, D. Ray, V. K. Aswal, J. Kohlbrecher, *Physical Review E* **2014**, *90*, 042316.

[29] H. B. Stuhrmann, A. Miller, *Journal of Applied Crystallography* **1978**, *11*, 325–345.

[30] J. Calo, P. Hall, M. Antxustegi, *Colloids and Surfaces A: Physicochemical and Engineering Aspects* **2001**, *187-188*, 219–232.

[31] SasView, SasView, Library Catalog: www.sasview.org, `https://sasview.github.io/`.

[32] J. S. Pedersen, *Adv. Colloid Interface Sci.* **1997**, 40.

[33] L. A. Feigin, D. I. Svergun, G. W. Taylor in *Structure Analysis by Small-Angle X-Ray and Neutron Scattering*, (Eds.: L. A. Feigin, D. I. Svergun, G. W. Taylor), Springer US, Boston, MA, **1987**, pp. 25–55.

[34] J. Berghausen, J. Zipfel, P. Lindner, W. Richtering, *The Journal of Physical Chemistry B* **2001**, *105*, 11081–11088.

[35] B. Hammouda, *Journal of Applied Crystallography* **2010**, *43*, 716–719.

[36] B. Hammouda, D. L. Ho, S. Kline, *Macromolecules* **2004**, *37*, 6932–6937.

[37] W.-R. Chen, P. D. Butler, L. J. Magid, *Langmuir* **2006**, *22*, 6539–6548.

[38] J. S. Pedersen, P. Schurtenberger, *Macromolecules* **1996**, *29*, 7602–7612.

[39] A. Riabtseva, L. I. Kaberov, L. Noirez, V. Ryukhtin, C. Nardin, B. Verbraeken, R. Hoogenboom, P. Stepanek, S. K. Filippov, *European Polymer Journal* **2018**, *99*, 518–527.

Chapter 7

Conclusions

The experimental evidence obtained by SANS allowed to propose a convincing picture of the porosity of the different sample groups by consistently arranging all the pieces of the mosaic of information obtained.
1) The German samples are more isotropic than the Mediterranean ones and the anisotropy is mainly due to porosity in the size range of hundreds of nm or more.
2) The volume of total porosity of the Mediterranean samples is more than three times larger than that of the German samples.
3) The ratio between open and closed pore volume is approximately 1 for the Mediterranean and 1/10 for the German samples.
4) The best model for the form factor of the pores relating to their shape corresponds to flexible cylinders with elliptical cross section, indicating a worm-like morphology. The pores in the Mediterranean samples are more interconnected, more extensive, and they have an articulated and complex shape. In general, they are characterised by a large morphological disorder, in terms of existing mutual interconnections and the irregularity of their shape.
In addition, the Mediterranean samples have, in all the size ranges, a more marked porosity than the German ones. This difference is particularly evident for open pores and more relevant in small pores range (whereas in the German samples closed pores dominate). Considering that the small closed pores are probably quite spherical in shape, this justifies the greater isotropy shown by the German samples. It is reasonable to consider that the differences demonstrated by SANS are closely related to the granularity of the raw materials used in different historical periods, to the geographical areas they are from and to the final use of the ceramic artefacts. On the other hand, it is well known that the main parameters determining the final porosity are firing temperature, raw material composition and other manufacturing technologies, such as the clay refining. The firing temperatures of all the samples investigated were

around 900°C and the starting clay materials were kaolin-rich clay (German samples) and Ca-rich clay (Mediterranean samples). Moreover, among the German samples two different origins can be distinguished, namely Central (Thuringia) and Eastern (Saxony) Germany, due to the specificity that the clay used in Central Germany was finer and thinner than that used in Eastern Germany. In order to identify which parameter plays the main role in the determination of porosity and to mimic historical samples, raw materials corresponding to Mediterranean Ca-rich paste and German kaolin-rich pastes from both the Thuringia and Saxony regions were procured. These raw materials were chosen for their similarity with historical samples in terms of mineralogical composition and granularity. From these pastes, lab ceramics have been made and were performed on them similar SANS analyses as on the historical samples. Preliminary results showed that even for samples belongings to the same compositional group, nanoporosity is more marked in those obtained from the finest raw materials. The complete study of lab ceramic samples in terms of the impact of different synthesis parameters on nanoporosity will be soon the subject of an additional paper. In summary, with this very detailed study of nanoporosity in ancient ceramic samples, it was possible to relate the nanoporosity, the open/closed pores ratio, the tortuosity and the form factor of pores to the manufacturing technologies and quality of the starting raw materials. This particular approach, specifically focused on nanoporosity, can open up new prospects for investigations in a plethora of innovative materials, bearing in mind that nanoporosity may be an important parameter for improving the engineering of the desired functional properties of advanced modern ceramics.

Acknowledgements

I will fill in these following lines with thoughts of gratitude addressed to all the special persons which have contribute to the successful outcome of this work. It is true that I am not a good writer and usually the blank space necessary to profoundly express all the words of gratitude is not enough. For this reason I'm going to write through the words of the music, using songs that are for me masterpieces.
Firstly I would like to express my sincere gratitude to my two tutors which are Prof. Elti Cattaruzza (Ca'Foscari University of Venice) and Dr. Claudia Mondelli (CNR-IOM-OGG and long term visitor at ILL). They have been, and still are, reference points, not only in the academic field but also in the everyday life. To Elti, who had trust in me and who provided me the opportunity to attend this wonderful experience in the field of neutron science, I extend my sincere thanks. For his support and encouragement during all my studies, for all the teachings and the interesting discussion and advice, I dedicate him the song "Mellow Dream" by Ryo Fukuy. Special thanks to Claudia, who welcomed me with open hands during the stage and the experiments at ILL. For her support, for all the precious conversations we have had and for all the "Nespresso" coffees she has offered to me during these two years, I dedicate to her the song "Samba de Bençao" by Vinicius de Moraes.
My sincere thanks also to Dr. Ralf Schweins, responsible of the D11 instrument at the ILL, for his patience, his time, his availability and his training about the neutron scattering. To him, I dedicate the song "Soul Sacrifice" by Santana.
I thank Dr. Miguel Angel Gonzales from the ILL Research Centre, for his kindness, willingness and his technical advice on the use of the SasView program; for his enormous patience I dedicate him the song "Nuntereggae Più" by Rino Gaetano.
I would like to thank Prof. Elisabetta Zendri (Ca'Foscari University of Venice) for our helpful discussions.
I would also like to thank Dr. Stefan Krabath, from the Landesamt für Archäologie Sachsen (Archaeological Heritage Office in Saxony), and Dr. Diego Calaon, from the Department of Humanities of Ca' Foscari University of Venice, for kindly giving me their time and for all the German and Mediterranean ceramic samples provided.

Many thanks also to Dr. Alessio De Francesco and Dr. Ferdinando Formisan (long-term visitors at the ILL and members of the Società Italiana Spettroscopia Neutronica, SISN) for all the lectures and the teachings they have given me during the SISN schools I have attended and for the good time we have spent together. To them I dedicate the song "Bebop" by Dizzy Gillespie.
I also would like to thank the friends I have met during the years of the University, for the special time I have spent with them, inside and outside the University Campus. In particular, I would like to mention Carlo for his advices and crazy-good ideas, and even Davide and Vittoria for all the time they have cheer up my soul and my mind. To them, I dedicate the song "Buena" by Morphine. A huge thanks is for all my close friends of the "Casteo City" with whom I'm still spending my time. With these beautiful and nice people I have travelled to different places, sharing with them a lot of adventures, concerts, feelings, beers and bottles of wine. I love them a lot, and I would like to dedicate the song "With a Little Help From My Friends" by Joe Cocker.
A special thank to Camilla, for all the time we have spent together in these years, the difficulties, the fights and then the laugh, the love and the precious experiences shared. I wish her the best as she deserve. To her I dedicate the song "Shape of My Heart" by Sting.
Last but obviously not least, my family. I would like to thank all of them, brothers and sister and especially my parents for their support, love and the free spirit they have taught me. To my mother I dedicate the song "Viva la Mamma" by Edoardo Bennato, for all the comprehension and the security that a mother can give. To my father I dedicate the song "Hasta Siempre" by Buena Vista Social Club, for all the time we have animatedly discussed on different subjects trying to coming up with reason. Even if we will not find the truth, I'm listening to you "siempre".